Thesis for obtaining
a title of Doctor of Chemical Engineering of Federal University of Rio Grande do Sul
a title of Doctor of Université de Lille

Specialty:
Organic, Mineral and Industrial Chemistry
Molecules and Condensed Matter

SYNTHESIS AND CATALYTIC PERFORMANCE OF METAL-ZEOLITE COMPOSITE CATALYSTS

by
Camila Gomes Flores

Thesis Supervisors:
Prof. Dr. Nilson Romeu Marcilio (UFRGS, Porto Alegre, Brazil)
Dr Andrei Khodakov, CNRS Research Director (UCCS, Université de Lille, France)

The PhD thesis defense took place on April 29th, 2019 in UFRGS, Porto Alegre, Brazil

PANEL OF EXPERT EXAMINERS:
Reviewer Dr Benoît Louis, DR CNRS, Université de Strasbourg (France)
Reviewer Professor Juliana da Silveira Espindola, Federal University of Rio Grande (Brazil)
Dr Cuong Pham-Huu, DR CNRS, Université de Strasbourg (France)
Professor Márcio Schwaab, Federal University of Rio Grande do Sul (Brazil)
Professor Nilson R. Marcilio, Federal University of Rio Grande do Sul (Brazil)
Dr Andrei Khodakov, DR CNRS, Université de Lille (France)

CONTENTS

TABLE LIST iv

FIGURE LIST v

ABSTRACT viii

RESUMO x

RESUMÉ xii

Chapter 1: Introduction 14

1.1 Challenges in the design of bifunctional catalysts and goals of the thesis 15

Chapter 2: Literature Review 18

2.1 Zeolites: structure, porosity, acidity and catalysis 18

2.2 Reactions occurring on metal-zeolite catalysts 29

2.2.1 Model reactions on acid sites 29

2.2.2 Model reactions on metal sites 32

2.2.3 Fischer-Tropsch Synthesis 33

2.2.4 Catalysts 39

References 40

Chapter 3: Influence of impregnation and ion exchange sequence on metal localization, acidity and catalytic performance of cobalt zeolite catalysts in Fischer-Tropsch synthesis 52

3.1 Introduction 52

3.2 Experimental Section 55

3.3 Results and Discussion 57

3.4 Conclusion 70

References 71

Supporting Information 74

Chapter 4: Direct production of iso-paraffins from syngas over hierarchical cobalt-ZSM-5 nanocomposites synthetized using carbon nanotubes as sacrificial templates 76

4.1 Introduction 76

4.2 Experimental Section 79

4.3 Results and Discussion 84

4.4 Conclusion 97

References 99

Supporting Information 102

Chapter 5: Multifaceted Role of Metal Carbon Nanotube Templates in the Synthesis of Hierarchical Zeolite Composite Catalysts 107

5.1 Introduction 108

5.2 Experimental 111

5.3 Results and Discussion 115

5.3 Conclusion 133

References 135

Chapter 6: General Conclusion and Perspectives 140

6.1 General Conclusion 140

6.2 Perspectives 142

TABLE LIST

Chapter 2

Table 2-1 Model reactions on zeolite acid sites. 13

Chapter 3

Table 3-1 Catalyst Characterization. 60

Table 3-2 Catalytic performance in FT at iso-coversion.* 67

Chapter 4

Table 4-1 Catalyst textural characterization. 85

Table 4-2 Catalyst acidity and cobalt reducibility. 90

Table 4-3 Activity and selectivity of the catalysts for the Fischer-Tropsch synthesis reaction (P=2 MPa, GHSV=20-70 L/h g_{Co}, T=250 °C, H_2/CO=2). 92

Chapter 5

Table 5-1. Catalyst characterization data……..108

Table 5-2. Activity and selectivity of the catalysts for the Fischer-Tropsch synthesis reaction (P=2 MPa, GHSV=20-70 L/hgCo, T=250 °C, H_2/CO=2)……..120

Table 5-3 Hydrogenation reaction (H_2=20 mL/min, Liquid flow=0.8 mL/h T=250 °C, P=20 bar)…… ..121

Table 5-4 Acylation reaction (2 g of anisol, 0.3 g hexanoic acid, 20 mg of the catalyst, T=180 °C; reaction time 2 h)…….122

FIGURE LIST

Chapter 2

Figure 2-1 Zeolite structure adaptaded from [20]..... 19

Figure 2-2 Polymorph of BEA zeolite [24]. 21

Figure 2-3 Formation of layers of tetrahedrons of ZSM-5 zeolite [27]..... 21

Figure 2-4 Schematic diffusion of reagents and products through the pores ZSM-5 zeolite (adapted from [29]). 22

Figure 2-5 Approaches for creating a hierarchical zeolite [44]. 24

Figure 2-6 Formation of Brönsted acid sites in zeolites (adapted from [51])..... 26

Figure 2-7 Formation of Lewis acid sites in zeolites (adapted from [51]). 26

Figure 2-8 Friedel-Craft alkylation reaction [83]. 31

Figure 2-9 General acylation reaction adapted from [85]..... 31

Figure 2-10 Ethylene hydrogenation reaction [96]..... 32

Figure 2-11 Toluene hydrogenation and products cracking [98]. 33

Figure 2-12 Conversion of non-petroleum sources to syngas for producing chemicals and liquids fuel (adapted from [104]). 34

Figure 2-13 FTS mechanism [106]. 35

Figure 2-14 Hydrocarbons selectivity as α function [108]..... 36

Figure 2-15 Carbene mechanism [113]. 38

Figure 2-16 Schematic representation of carbonyl insertion [113]. 38

Chapter 3

Figure 3-1 Co 2p XPS spectra of the calcined cobalt BEA zeolite catalysts. 62

Figure 3-2 TPR catalyst reduction profiles. 63

Figure 3-3 Localization of cobalt species in the CoH/HBEA (a) and CoH/NaBEA zeolite (b). 65

Figure 3-4 Wax products (C_{9+}) distribution. 68

Figure 3-5 ASF distribution plot for the wax products obtained from the FT synthesis reaction. 68

Chapter 4

Figure 4-1 XRD patterns of cobalt ZSM-5 nanocomposites. 85

Figure 4-2 TEM images of $Co_{(10-20)}$/ZSM-5 (A), $CoCNT_{(10-20)}$/ZSM-5(B), $CoCNT_{(10-20)}$/ZSM-5 high magnification(C) and $CoCNT_{(20-40)}$/ZSM-5 high magnification. 87

Figure 4-3 Synthesis of ZSM-5 zeolite using Co/CNT as sacrificial templates. Resulting zeolites replicate carbon nanotube morphology. 88

Figure 4-4 Results of STEM-HAADF electron tomography analysis of $CoCNT_{(20-40)}$ZSM-5 catalyst (3D volume and typical slices showing clearly the presence of cobalt nanoparticles inside the zeolite structure). 89

Figure 4-5 Temperature programmed reduction (TPR) profiles of the catalysts. 89

Figure 4-6 Molar distribution of liquid products by carbon number. $Isomer_{Total}$ represents the total amount of isomerized products in the gas fraction. α represents the chain growth coefficient for the ASF distribution. 94

Chapter 5

Figure 5-1 Low temperature nitrogen adsorption-desorption isotherms on the HZSM-5 zeolite synthetized with and without addition of CNT (a) cobalt (b), nickel (c) and magnesium (d) ZSM-5 catalysts. 116

Figure 5-2 XRD patterns of the metal ZSM-5 catalysts. 120

Figure 5-3 TEM images of $CoCNT_{(10-20)}$/ZSM-5 high magnification(A), $CoCNT_{(20-40)}$/ZSM-5 high magnification (B), $MgCNT_{(10-20)}$/ZSM-5 (C) and $NiCNT_{(20-40)}$/ZSM-5 (D). 121

Figure 5-4 TEM image and SAED patterns of NiCNT(20-40)/ZSM-5 zeolite. 122

Figure 5-5 STEM-HAADF electron tomography analysis of $CoCNT_{(20-40)}$/ZSM-5 catalyst clearly showing the presence of cobalt nanoparticles inside the zeolite structure. 123

Figure 5-6 Synthesis of hierarchical zeolites using metal oxide supported on CNT as secondary hard templates..... 124

Figure 5-7 Temperature programmed reduction (TPR) profiles of the Co (a) and Ni (b) catalysts. 125

Figure 5-8 FTIR spectra observed after adsorption of Py on cobalt (a), nickel (b) and magnesium (c) zeolite catalysts..... 128

Figure 5-9 Acylation of anisole with hexanoic acid results in ortho-methoxy-hexyl-phenone..... 131

Figure 5-10 Hexanoic acid conversion in anisole acylation over the metal zeolite catalysts prepared by impregnation and using Me/CNT as secondary hard templates. 133

ABSTRACT

Zeolites are microporous crystalline solids with a regular pore system, which have found numerous applications in industrial processes such as oil refining, organic synthesis, adsorption and separation. Very small pore size of zeolites (~1 nm) imposes diffusional limitations for many catalytic reactions. The catalytic performance of metal zeolite bifunctional catalysts can be improved by creating hierarchical zeolites and by controlling localization of metal species within the zeolite crystals. Impregnation is an efficient method for the preparation of bi-functional cobalt-zeolite catalysts for the direct production of liquid fuels from syngas. In the catalysts prepared via impregnation, cobalt occupies the cation exchange positions in the zeolite micropores decreasing the number of acid sites available for hydrocarbon isomerization and cracking. Isolation of cobalt ions in cationic positions reduces catalyst reducibility, makes it difficult to achieve metallic state and decreases the amount available metal active sites for Fischer Tropsch synthesis. We found that the presence of Na^+ instead of H^+ ions in the exchange positions of the large pore Beta zeolite favored deposition of cobalt on the external surface of the zeolite, while the acid sites in the zeolite micropores were not much affected. The large pore cobalt Beta zeolite catalyst with cobalt species localized on the external surface and high concentration of acid sites in the zeolite crystals has showed enhanced catalytic performance in Fischer-Tropsch synthesis combined with hydrocarbon isomerization

Another approach of this thesis has addressed creating hierarchical zeolites with several levels of meso- and microporosity using sacrificial templates. Hierarchical zeolites synthesized using cobalt containing carbon nanotubes, as sacrificial hard templates exhibited higher catalytic activity, lower methane selectivity and higher selectivity to isomerized hydrocarbons in Fischer-Tropsch synthesis. The synthesis strategy based on metal carbon nanotubes as sacrificial templates has been extended to other metals such as

nickel and magnesium. This new approach to the synthesis of metal-zeolite composite increases the mesoporosity and improves the catalytic performance in hydrogenation of aromatics and anisole acylation.

Keywords: hierarchical zeolite, hard template, cobalt, catalysis, catalytic reactions

RESUMO

As zeólitas são sólidos cristalinos microporosos com um sistema de poros regular que têm encontrado inúmeras aplicações em processos industriais, como refino de petróleo, síntese orgânica, adsorção e separação. O tamanho muito pequeno dos poros das zeólitas (~1 nm) impõe limitações difusionais para muitas reações catalíticas. O desempenho catalítico de catalisadores bifuncionais de zeólitas-metal pode ser melhorado através da criação de zeólitas hierárquicas e do controle da localização de espécies metálicas dentro dos cristais da zeólita. A impregnação é um método eficiente para a preparação de catalisadores bifuncionais (cobalto-zeólita) para a produção direta de combustíveis líquidos a partir do gás de síntese. Nos catalisadores preparados via impregnação, o cobalto ocupa as posições de troca catiônica nos microporos das zeólitas, diminuindo o número de sítios ácidos disponíveis para a isomerização e fracionamento de hidrocarbonetos. O isolamento de íons cobalto em posições catiônicas reduz a redutibilidade do catalisador, dificultando a obtenção do estado metálico e diminuindo a quantidade de sítios metálicos ativos disponíveis para a síntese de Fischer Tropsch. A presença de íons Na^+ em vez de H^+ nas posições de troca da zeólita Beta, que apresenta poros grandes, favorece a deposição de cobalto na superfície externa dessa zeólita, não afetando os sítios ácidos nos microporos. O catalisador a base de cobalto suportado em zeólita hierárquica que apresenta espécies de cobalto localizados na superfície externa e possui alta concentração de sítios ácidos nos cristais de zeólita mostrou o melhor desempenho catalítico na síntese de Fischer-Tropsch combinada com a isomerização de hidrocarbonetos.

Essa tese também abordou a criação de zeólitas hierárquicas com vários níveis de meso- e microporosidade usando agentes estruturais. Foram sintetizadas zeólitas hierárquicas utilizando nanotubos de carbono contendo cobalto, uma vez que o uso de *templates*

rígidos resultou em maior atividade catalítica, menor seletividade a metano e maior seletividade a hidrocarbonetos isomerizados na síntese de Fischer-Tropsch. A síntese baseada em nanotubos de carbono impregnando metais como *template* de sacrifício na síntese zeolítica foi estendida a outros metais, como níquel e magnésio. Esta nova abordagem para a síntese do compósito metal-zeólita aumenta a mesoporosidade e melhora o desempenho catalítico na hidrogenação de aromáticos e acilação de anisol.

Palavras-chave: zeólita hierárquica, agente estruturante, cobalto, catálise, reações catalíticas

RESUMÉ

Les zéolithes sont des solides cristallins microporeux avec un système de pores réguliers, qui ont trouvé de nombreuses applications dans les procédés industriels tels que le raffinage du pétrole, la synthèse organique, l'adsorption et la séparation. Une très petite taille des pores des zéolithes (~1 nm) impose des limitations diffusionelles pour des nombreuses réactions catalytiques. La performance catalytique des catalyseurs bifonctionnels à base de zéolites peut être améliorée en créant des zéolithes hiérarchisées et en contrôlant la localisation des espèces métalliques. L'imprégnation est une méthode efficace pour la préparation de catalyseurs bifonctionnels à base de cobalt-zéolite pour la production directe de carburants liquides à partir de gaz de synthèse. Dans les catalyseurs préparés par imprégnation, le cobalt occupe les sites cationiques dans les micropores de zéolite, ce qui diminue le nombre de sites acides disponibles pour l'isomérisation et le craquage des hydrocarbures. L'isolement des ions cobalt en sites cationiques réduit la réductibilité du catalyseur, rend difficile d'obtenir l'état métallique et diminue la quantité de sites actifs métalliques disponibles pour la synthèse Fischer Tropsch. Nous avons démontré que la présence des ions Na^+ au lieu des ions H^+ dans les sites cationiques de zéolite favorise le dépôt de cobalt à la surface externe, alors que les sites acides dans les micropores de la zéolite sont peu affectés.

Une autre approche de cette thèse porte sur la synthèse de zéolithes hiérarchisées à plusieurs niveaux de méso- et microporosité en utilisant des agents structurants sacrificiels. Les zéolithes hiérarchisées synthétisées à l'aide de nanotubes de carbone contenant du cobalt présentaient une activité catalytique plus élevée, une sélectivité en méthane plus faible et une sélectivité plus importante en hydrocarbures isomérisés dans la synthèse Fischer-Tropsch. La stratégie de synthèse fondée sur les nanotubes de carbone comme agents structurants a été étendue à d'autres métaux comme le nickel et le

magnésium. Cette nouvelle approche à la synthèse de composites métal-zéolite en utilisant des nanotubes de métal-carbone comme agents structurants sacrificiels augmente la mésoporosité et améliore la performance pour l'hydrogénation d'aromatiques et l'acylation d'anisole.

Mots-Clés: zéolite hiérarchisée, agent structurant, cobalt, catalyse, réactions catalytiques

Chapter 1: Introduction

Heterogeneous catalysis plays an important role in the chemical industry. The major challenge in the heterogeneous catalysis is catalyst design with good activity, high selectivity and satisfactory stability. For this reason many researchers are looking for new approaches to the catalyst design [1]. Use of bifunctional catalysts can advantageous for multistage catalytic reactions, because these materials contain both metallic sites over metal nanoparticles and acid sites from support (e.g. metals combine with zeolite) [2]. Design of efficient bifunctional catalysts remains however, a major challenge.

Zeolites are crystalline aluminosilicates with uniform micropores with pores size smaller than 2 nm. These minerals have been widely used for adsorption, membrane separation and in the field of catalysis. The zeolite main properties are ordered microporosity and presence of Brönsted and Lewis acid sites. The crystalline framework gives zeolites mechanical and high thermal stability, high specific surface area and high ion-exchange capacity [3–6].

The zeolite properties, mainly their strong acid sites and their thermal stability, make them promising materials for catalysis [7]. Zeolite can be used as acid or as bifunctional catalysts when a metal has been added to the structure [8]. Conventional ways to introduce metals into the zeolites are through impregnation or ion exchange. However, this can lead to the neutralization of some acid sites in the zeolites [9]. The metal ions introduced by impregnation or ion exchange will probably occupy a cation exchange position, decreasing the number of acid sites available in the zeolite [10]. The number of acid sites is extremely important for many catalytic reactions occurring on zeolites. For example, the transformation of syngas into branched hydrocarbons is easier when more acid sites are available in the bifunctional catalysts. The presence of acid sites favors hydrocarbon cracking and isomerization. Another issue concerning the location of the

metal in the support is the difficult reduction of the metal for metallic state, which leads to a lower amount of metal active phase. The metal distribution on the outer surface and in the micropores of the zeolite is an important parameter, which could affect the catalytic performance of metal zeolite composite catalysts

In addition, conventional zeolites exhibit diffusion limitations in particular, for bulky molecules as a result of their small micropores. One of solutions to reduce diffusion limitations over zeolite catalysts is synthesis of mesoporous or hierarchical zeolites. There are two major ways to create mesoporosity in zeolites, known as top-down and bottom-up methodologies. The classical top-down methods consist of physical and chemical treatments, such as desilication and dealumination [11,12]. This approach may cause a broad distribution of mesopores and an instability in the zeolite structure because a part of the zeolite will be destructed by removing silicon or aluminum. In the bottom-up strategies soft and/or hard templates are used. This procedure is performed by introducing a solid material, normally a rigid structure, into the zeolite gel. Therefore, the zeolite crystallization occurs around the template during the hydrothermal treatment and, when the template is removed by combustion or dissolution, the mesopores are created [4].

1.1 Challenges in the design of bifunctional catalysts and goals of the thesis

In this literature review, two major challenges have been identified in the design metal-zeolite bifunctional catalysts. The first challenge is relevant to the small pore sizes of the zeolites, which results in major diffusional limitations. One of the possible solutions could be design of hierarchical zeolites with enhanced mesoporosity. The second challenge in bifunctional catalysts is relevant to the localization of the metal and acid sites with the zeolites. It is often considered that the proximity between metallic and acid sites is particularly important to obtain enhanced catalytic performance in the catalytic

reactions requiring bifunctional catalysts. At the same time, localization of metal species in the zeolite micropores can be harmful for catalytic performance. It can lead to decrease in the zeolite acidity due to the neutralization of acid sites by metal cations. Small metal oxide particle size can also result in poor metal reducibility.

The present PhD thesis focuses on the design of new synthesis strategies for the preparation of hierarchical nanocomposites of metal and zeolite and their application in catalysis. We suppose that the control of localization of metal nanoparticles within the zeolite micro and mesopores can influence on the selectivity of catalytic reactions and in particular Fischer-Tropsch synthesis.

The first goal of this thesis is to optimize the impregnation sequence while introducing cobalt ions on the metal localization in zeolite and catalytic performance in FT synthesis. Cobalt is introduced by impregnation either to the sodium or proton forms of large pore BEA zeolite. Higher reaction rates are observed over the catalysts, which did not contain cobalt ions in the cation sites of the zeolite. Lower methane selectivity and higher selectivity to isomerized hydrocarbons are observed when cobalt species are located on the zeolite outer surface and acid sites inside the zeolite micropores. The BEA zeolite has relatively large pores. The situation could be different for ZSM-5 with narrow zeolite pores (d= 5.5 Å) and the diffusion limitation in ZSM-5 zeolites can become much more severe. The preferential localization of cobalt species on the outer surface of ZSM-5 might not be therefore optimal for the enhanced catalytic performance.

The second goal of the thesis is to create hierarchical ZSM-5 zeolite using carbon nanotubes (CNT) with different diameters as sacrificial template. Our target is to obtain in a one-pot synthesis composite hierarchical zeolites with cobalt metal particles uniformly distributed in the zeolite mesoporous structure. The cobalt zeolite catalysts

prepared using cobalt carbo nanotubes as secondary templates showed enhanced selectivity to iso-paraffins.

Finally, the third goal of the thesis is to extend the methodology, which involves using cobalt CNT as secondary templates to other metals such as nickel (Ni) and magnesium (Mg) introduced into the ZSM-5 zeolites. We uncovered three roles of Me-CNT in the zeolite synthesis. First, they strongly affect the shape of the synthesized zeolites, which seem to be replicas of CNT and show distinct fibrous morphology. Second, the Me-CNT act as mesoporogen and strongly enhance the zeolite mesoporous volume. Finally, zeolite synthesis in the presence of Me-CNT offers the opportunity to simultaneously introduce new catalytic functions leading to bifunctional metal-zeolite catalysts. The catalysts designed using this methodology were evaluated on model reactions such as aromatics hydrogenation by Ni catalyst and anisole acylation for all catalysts (Ni, Co and Mg).

The main results of this thesis are published and submitted in the papers below:

2018 - **Influence of Impregnation and Ion Exchange Sequence on Metal Localization, Acidity and Catalytic Performance of Cobalt BEA Zeolite Catalysts in Fischer-Tropsch Synthesis** Camila Flores, Nuno Batalha, Nilson R. Marcilio, Vitaly V. Ordomsky, and Andrei Y. Khodakov – **ChemCatChem.**

2018 -**Direct Production of Iso-Paraffins from Syngas over Hierarchical Cobalt-ZSM-5 Nanocomposites Synthetized by using Carbon Nanotubes as Sacrificial Templates** - Camila Flores, Nuno Batalha, Vitaly V. Ordomsky, Vladimir L. Zholobenko, Walid Baaziz, Nilson R. Marcilio, and Andrei Y. Khodakov – **ChemCatChem.**

2019 - Versatile Roles of Metal Species in Carbon Nanotube Templates in the Synthesis of Metal-Zeolite Nanocomposite Catalysts - Camila Flores, Vladimir L. Zholobenko, Bang Gu, Nuno Batalha, Valentin Valtchev, Walid Baaziz, Ovidiu Ersen, Nilson R. Marcilio, Vitaly V. Ordomsky and Andrei Y. Khodakov **– submitted**.

Chapter 2: Literature Review

This chapter presents a literature review of the main topics discussed throughout that thesis such as zeolites, hierarchical zeolites, Lewis and Brönsted acidity, bifunctional catalysts, model reactions on acid and metallic sites, Fischer Tropsch synthesis. After analysis of the literature, Chapter 2 summarizes challenges for the design of new zeolite based catalysts. The goals of this thesis are also defined in this chapter.

2.1 Zeolites: structure, porosity, acidity and catalysis

Zeolites are microporous aluminosilicates with crystalline structure formed by AlO_4 and SiO_4 tetrahedra linked via their edges. The zeolites are important as industrial catalysts in petroleum refining (e.g. catalytic cracking, hydrocracking, isomerization, alkylation, fuels etc.) and chemical processes such as oxidation of olefins, fragrance synthesis [13]. The main synthetic zeolites used in these processes are Mordenite Framework Inverted (MFI), Faujasite (FAU) and Beta (BEA). They have been commercialized as catalysts [14].

Zeolite materials present specific features such as large surface area, high thermal stability, high ion-exchange capacity, presence of strong acid sites and shape-selectivity [5]. However, the structural micropores of zeolite become their disadvantage for the mass transfer of bulky molecules causing diffusion limitations for reagents, intermediates and products [15]. In the last years, numerous works have been performed in order to create zeolites with mesopores and to minimize the diffusional limitations [16].

2.1.1 Structure

The zeolites are structured in a crystalline form composed of tetrahedron of TO_4 (T is Si or Al in a natural zeolite and can be others elements such as Ga, Ge, Fe, B, P, Ti in a synthetic material) connected through oxygen atoms (Figure 2-1) [17]. Zeolite structure contains channels and cavities, with the sizes of around 1 nm, which are accessible for many molecules [18]. The combination of silicon and oxygen in tetrahedra leads to formation of an uncharged solid (SiO_2). When the aluminum is incorporated in the silica structure, the structure is charged negatively. This fact occurs through the $Al^{3+} \leftrightarrow Si^{4+}$ substitution and requires the compensating cations to keep the overall framework neutral [19].

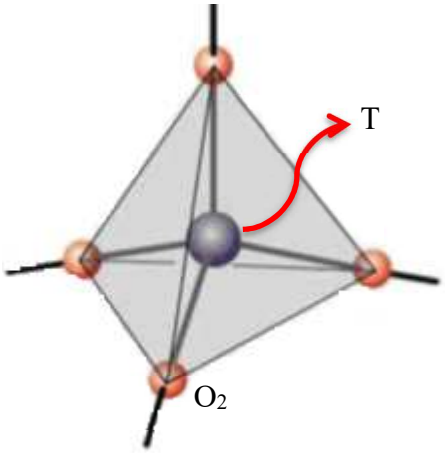

Figure 2-1 Zeolite structure adaptaded from [20].

The compensating cations (normally Na^+ or others alkaline or alkaline earth ions) are transmutable ions, attributing this material an ion-exchange capacity, where the metal ion could be changed by other cation (e.g. metal, ammonium and quaternary ammonium). The zeolite composition can be described by the following empirical formula:

$$M_{x/m}^{m+} \cdot [AlO_2]_x \cdot [SiO_2]_y \cdot nH_2O$$

where M is a compensating cation with the charge m, x and y are the number of Al and Si atoms in the unit cell and n is the number of water molecules. The silicon/aluminum

(or simply Si/Al) ratio in the framework represents an important characteristics, since it determines the acidity and ion-exchange capacity.

The structure of zeolites involves blocks of 3, 4, 5 and 6 membered rings (MR), each MR is linked with nT and O atoms, thus all oxygen atoms are connected with 2 T atoms. Thus, a 6 MR contains 12 atoms which can be T atoms or oxygen atoms. Zeolites can be classified into three categories according to their porosity:

- Small pore (8 Membered ring): the pores are constituted of 8 atoms (T or O) and the diameter size is between 0.3 to 0.45 nm (e.g. LTA).

- Medium pore (10 Membered ring): the pores are composed of 10 atoms (T or O) and the diameter size is between 0.45 to 0.60 nm (e.g. MFI).

- Large pore (12 Membered ring): presents 12 atoms (T or O) and the pore diameter is between 0.60 to 0.80 nm (e.g. BEA).

Depending on the pore class (small, medium or large), the zeolite can be used for adsorption and in many catalytic reactions. There are several types of zeolites that have a wide application on catalytic processes like faujasite (Y), beta (BEA) and MFI (ZSM-5), the use in these processes is linked with their properties such as high surface area, acidity and thermal stability [21,22].

BEA has ring channels with twelve tetrahedra that intersect on three-dimensions and different opening size, the first with 5.5 Å x 5.5 Å and two others of 7.6 Å x 6.4 Å (Figure 2-2). The range of Si/Al ratio is 10-100, it can reach 150. The greater is the Si/Al ratio of zeolite, higher is the thermal stability. The Beta zeolite has relatively large micropores, high surface area (600 m²/g), shape selectivity, ion exchange capacity. The large micropores of BEA zeolite allow selective absorption of bulky molecules, such as aromatic hydrocarbons [23].

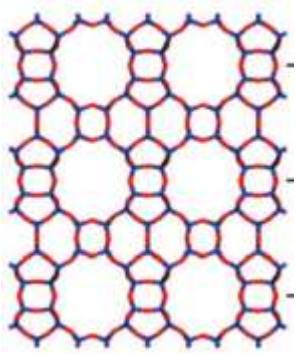

Figure 2-2 Polymorph of BEA zeolite [24].

ZSM-5 (MFI zeolite) has a structure formed by unit cells with ten rings of five T atoms, which are united by oxygen atoms to a similar chain, thus forming channels (Figure 2-3). These channels form a three-dimensional structure of ZSM-5 zeolite. ZSM-5 presents also a high ratio of silicon to aluminum (Si/Al>11) [25]. This ratio has strong influence on the capacity ion-exchange, that the greater is quantity of aluminum in the framework, the greater will be the amount of charge-compensating cation [26].

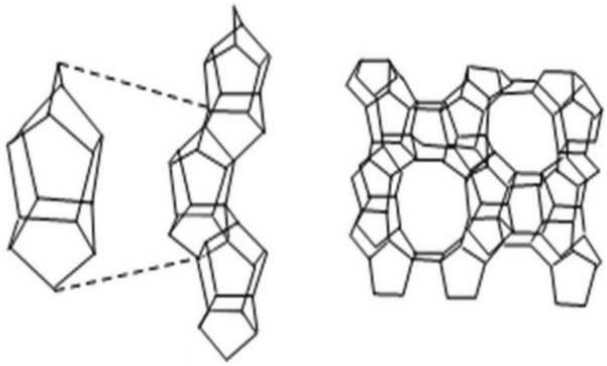

Figure 2-3 Formation of layers of tetrahedrons of ZSM-5 zeolite [27].

2.1.2 Porosity and hierarchical zeolites

Despite many interesting properties, zeolites display difficulties for mass transport of chemical compounds, which have the size of the molecules similar or larger than the zeolite micropores. The small pores reduce the transport of reagents towards the active sites, consequently forming the undesired by-products and coke deposits. This may also

results in blocking the zeolite micropores and a fast catalyst deactivation and their short life-time [5,28]. It is necessary therefore to improve transport properties of the zeolite by creating mesopores (according to IUPAC the mesopore sizes vary from 2 to 50 nm) (Figure 2-4).

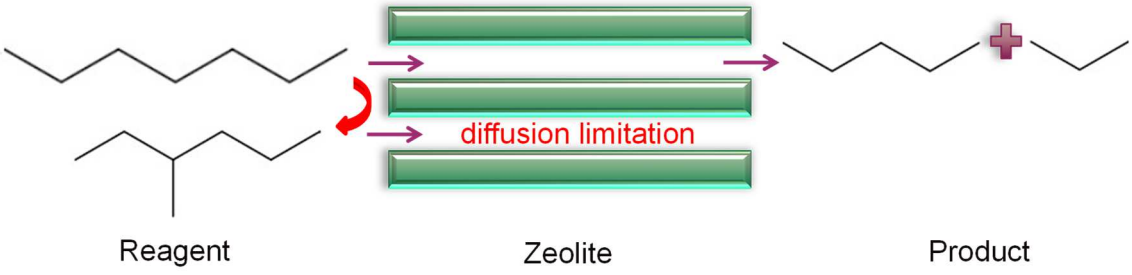

Figure 2-4 Schematic diffusion of reagents and products through the pores ZSM-5 zeolite (adapted from [29]).

In order to overcome these, numerous efforts have made to synthesize nano-sized zeolite crystals, extra-large pore zeolites or mesoporous zeolites, the latter are often referred to as hierarchical zeolites [30]. The hierarchical zeolites contain, in addition to the well-defined micropore system, mesopores with the diameters in the range of 2-50 nm. Different to zeolite micropores, the size, shape and orientation of these mesopores are not directly related to the zeolite crystalline structure. Hierarchical porous zeolite materials begin to gain space in the research due to their reduced diffusion limitation on the reactions and improved accessibility of active sites. The zeolite mesopores can also delay catalyst deactivation [31]. Several synthesis strategies have been proposed to obtain hierarchical zeolites, which are divided into “top-down” and “bottom-up” (Figure 2-5). The first approach consists in creating a hierarchical zeolite starting from already synthetized zeolite. The main techniques used are dealumination using acid and desilication using alkaline solutions [17].

Dealumination is based on removing Al atoms in the zeolite post-synthesis treatment. This method can be realized in two ways. The first way involves chemical

agents like H_4DTA, ammonium fluorosilicate ($(NH_4)_2SiF_6$) in the liquid-phase and silicon tetrachloride ($SiCl_4$) in the gas-phase reactions, the dealumination occurs by Al leaching. Another way of zeolite dealumination is carried out at high temperature (873-1073 K) via steaming process. This treatment leads to the hydrolysis of -Si-O-Al- bonds. The Al atoms are then detached from original zeolite structure. Beyond, these both methods can be used together [32].

Desilication is a method well known for creating the secondary porosity in zeolites. It involves silicon extraction from zeolite framework using alkaline solutions (e.g. NaOH), basically preserving aluminum and acidic properties [5,33–35].

However, by using the "top-down" methodology it is difficult to control the creation of uniform mesopores. It might lead to the partial destruction of zeolite structure [36]. The "bottom-up" approach is considered more challenging for the researchers because it depends on templates and conditions of zeolite synthesis, such as hard and soft templating [37]. Both hard and soft templates have been utilized to synthetize hierarchical zeolites using the "bottom up" approach. The hard templates usually include carbon nanoparticles, nanotubes and polymer beads, while various cationic surfactants, organosilane, cationic polymer, and ionic liquids are considered as soft secondary templates. Both hard and soft templates could be removed by calcination. There are numerous reports in the literature that address using templates for obtaining mesopores in zeolites. Zhang et al. [38] used bifunctional (TPABr-grafted MWCNT) template to synthesize hierarchical ZSM-5 zeolite, Wang et al. [26] used organo-functionalized mesoporous silica (MS) as silica source to create the spherical self-assemblies of ZSM-5 nanocrystals. Huang et al. [39] synthesized a hierarchical Beta zeolite using a layered silicate precursor (H-kanemite) as silica source. Several methodologies, which involve soft and rigid/hard templating for creating hierarchical zeolites are described below.

Double templating is carried out with different types of surfactants (e.g. CTMA, CTAB). Those molecules tend to create micelles in aqueous solutions. The surfactant is removed by calcination or washing, thereby, forming mesostructure in the solids [40, 41].

Rigid or hard templating consists of using hollow or porous solids, which incorporate zeolites during their synthesis and create mesopores on their removal. The methodology may be described by the following general three steps: (a) a solution containing the reagents and zeolite precursors is added into the pores/cavities of the template, (b) zeolite crystals are growing within the hard template, (c) the template is removed by calcination (organic templates) or dissolution processes (inorganic templates). The most usable hard templates are carbonaceous (e.g. carbon nanotubes (CNT), carbon fibers) and polymer microspheres (e.g polystyrene) [17, 42-43].

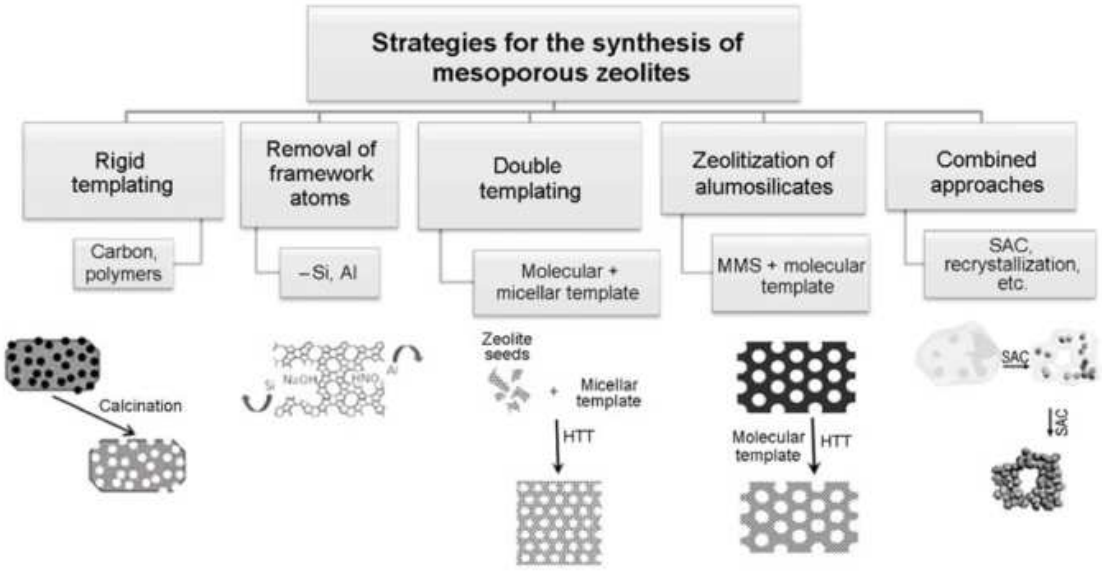

Figure 2-5 Approaches for creating a hierarchical zeolite [44].

Because of the presence of mesoporosity, the molecular diffusion is substantially improved over hierarchical zeolites. The mesoporosity is able to reduce the molecule residence time inside the pores avoiding secondary reactions, increasing lifetime and minimizing the catalyst deactivation. Zeolite with large pores can be applied in different reactions such as cracking, alkylation, isomerization, oxidation, condensation among

others [45,46]. Furthermore, another challenge beyond creating mesopores is design of bifunctional catalysts by encapsulation of metal nanoparticles in zeolite micro- and mesopores. It is believed that the metal confined in the crystals of zeolite can improve catalytic performance, activity and stability in Fischer Tropsch synthesis (FTS) and other reactions [47].

2.1.3 Brönsted and Lewis acidities

Acidity of the zeolites is related to their structure and chemical composition. The zeolite acid sites are mostly localized inside their pores. Therefore, zeolite can be used in a safer way than sulphuric acid for example, which is a highly corrosive liquid [48,49]. Catalytic activity of zeolite is often correlated with the number and types of Brönsted and Lewis acid sites present in this solid structure [32].

The amount and strength of acid sites are affected by Al concentration and distribution in the zeolite framework. The zeolite acidity occurs through substitution of Si^{4+} atoms with Al^{3+} atoms, which produces a negatively charged structure. This charge needs to be compensated, a proton is linked to neighbour oxygen between one Si and one Al, forming a hydroxyl group (Si-O(H)-Al), which is responsible for Brönsted acidity [50]. Aluminum concentration in the lattice is directly proportional to the concentration of acid sites in the zeolites [7]. The formation of Brönsted sites from the sodium form of zeolite is presented in Figure 2-6.

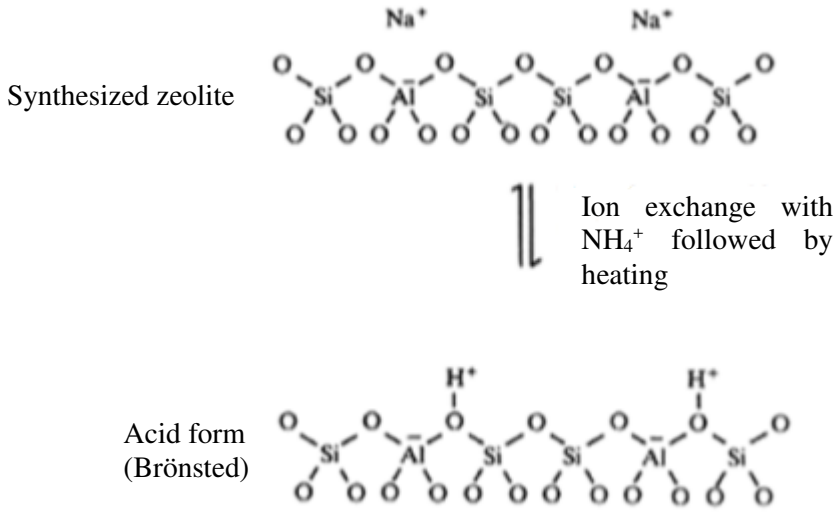

Figure 2-6 Formation of Brönsted acid sites in zeolites (adapted from [51]).

The Lewis acid sites in zeolites are formed during the calcination (>500 ºC) owing the dehydroxylation of Brönsted acid sites (Figure 2-7) [49].

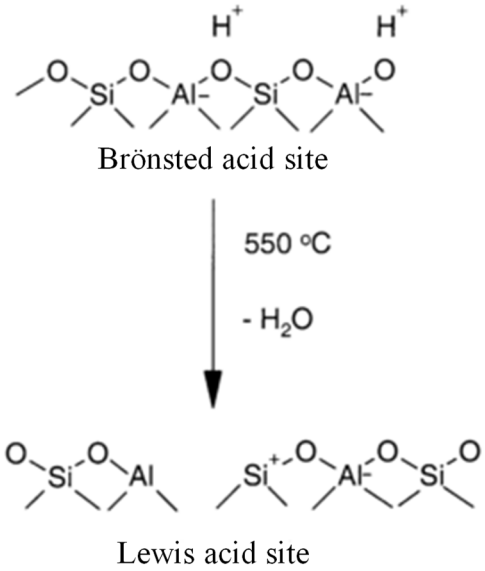

Figure 2-7 Formation of Lewis acid sites in zeolites (adapted from [51]).

Lewis acid sites are electron-receptors and are linked to aluminum atoms with octahedral coordination located extra framework of the zeolite. They can be also formed by low coordinated T atoms inside the zeolite framework. Aluminum extra framework

species may have different forms like Al^{3+}, $Al(OH)^{2+}$, AlO^{+} and exhibit a weak Brönsted acidity [52].

The nature of acid sites may be characterized by NH_3-stepwise temperature-programed desorption (NH_3-STPD), infrared spectrometry (IR) with molecular probes (NH_3, pyridine, acetonitrile etc), nuclear magnetic resonance (NMR) and microcalorimetry among others [53, 54]. Infra-red spectroscopy is a technique most commonly used for measuring the acidity in porous solids. Generally, pyridine is used as a probe molecule. The pyridine interaction with of Brönsted or Lewis acid sites forms adsorbed species with characteristic vibrational frequencies that correlate with the type and concentration of acid sites. The quantification of the species may be done by the IR peak area integration [55- 56].

2.1.4 Bifunctional catalysis and catalysts

The concept of multi-functional catalysis was developed in the 60s of last century by Weiss [57]. Bifunctional catalysts are those that present two types of active sites. These kinds of catalysts usually have metallic sites, whose function is dehydrogenation/hydrogenation and acid sites, whose main function is to conduct acid catalyzed reactions (e.g. cracking, isomerization and others) [58]. The components responsible for hydro-dehydrogenation may be of several types: (a) transition or noble metals with good dispersion such as platinum (Pt), palladium (Pd) and other, (b) metal sulphides and (c) metal oxide such as cobalt (Co), nickel (Ni), iron (Fe), copper (Cu) supported on zeolite. Bifunctional catalysts employed in industrial processes often contain Pt, which plays a role in hydrogenation-dehydrogenation. The presence of metallic sites in these catalysts is of fundamental importance. They can catalyze reactions

such as hydrogenation-dehydrogenation, hydrogenolysis, aromatization and hydrocarbon cyclization [59-60].

Metallic sites usually catalyze hydrogenation-dehydrogenation reactions, while acid sites catalyze the carbocation rearrangements. There is an association between the acid and metallic sites in bifunctional catalysts, which increases catalytic activity and product yield. Therefore, a balance and a synergy of the acid and metallic sites in bifunctional catalysts is extremely important. It often determines activity, stability and product selectivity [54, 61]. The activity and selectivity of catalysts depend on the acid support. Generally the reaction rate of isomerization of n-paraffins is limited both by catalytic activity of acid support and activity of metal function [62,63, 64].

Strength of acid sites and distribution of metal and acid sites are important parameters of bifunctional catalysts. In bifunctional catalysis, the kinetic steps of the consequent reactions are coupled to each other through the processes of diffusion of these intermediates from one type of sites to another. The two types of active sites in bifunctional catalysts should be as closer as possible for attaining higher catalytic activity and selectivity [65]. The metals can be introduced into zeolite by different methodologies, the most used is incipient wetness impregnation (IW or IWI), also called capillary impregnation or dry impregnation [66].

Wet impregnation consists in adding to the catalytic support a solution containing metal precursor that filling the zeolite pores followed by drying, calcination/reduction steps. This technique is called “incipient wetness impregnation”, when the volume of solution is equal or smaller than the total pore volume of the support [10].

2.2 Reactions occurring on metal-zeolite catalysts

2.2.1 Model reactions on acid sites

The model reactions are used as tools for characterizing the active basic, acid or acid-basic solid supports. Those reactions are summarized in Table 2.1 with some examples of zeolite catalysts.

Table 2-1 Model reactions on zeolite acid sites.

Type of Reaction	Typical applications and catalysts
Isomerization	Bifunctional Pt/Fe-ZSM-5 catalyst for xylene isomerization [67].
Cracking	SO_4^{2-}/TiO_2 promotion on HZSM-5 for catalytic cracking of paraffin [68].
Oligomerization	Butene oligomerization reaction over the hemicellulose modified HZSM-5 [69].
Friedel-Crafts	Benzene alkylation with methanol over ZSM-5 zeolite [70]. Friedel-Crafts acylation reactions over hierarchical MCM-22 zeolites [71]. Acylation of ansiole with long-chain carboxylic acids over wide pore zeolites [72]. Effects of acid-modified HBEA zeolites on thiophene acylation and the origin of deactivation of zeolites [73].

Isomerization is a reaction leading to the production of isomers (same molecular size, type and atoms number but with different molecular arrangement) [74]. The hydrocarbon isomerization is conducted for obtaining branched isomers, because they are chemical compounds with a high commercial value. The octane number of the branched hydrocarbons is higher than that for linear compounds.

Olefin isomerization is a fast reaction, while isomerization of paraffins is slower and requires very high temperatures. The paraffin isomerization reaction occurs on bifunctional catalyst with acid sites for isomerization by carbenium ions produced from

olefins and metallic sites for dehydrogenation/hydrogenation from paraffins to olefins and vice versa. Assuming the classical mechanism, the paraffins dehydrogenate first on the metal sites and the protonated olefins are produced over the Brönsted acid sites. Carbenium ions rearrangement and β-scission follows by hydrogenation and deprotonation on metal sites towards the paraffins [62,75]. This mechanism can be descripting by following steps occurred over bifunctional catalysts [8]:

(a) Hydrogenation/dehydrogenation over metal sites;

(b) Protonation/deprotonation on acid sites;

(c) Proton addition to form alkyl-carbenium ion on acid sites;

(d) Competitive absorption/desorption of carbenium ion and alkene over acid sites;

(e) Rearrangement of alkyl-carbenium ion;

(f) Cracking of alkyl-carbenium ion.

Acid supports of bifunctional catalysts can be amorphous oxides, mixtures of oxides (e.g Al_2O_3, Si_2O-Al_2O_3), zeolite (Y, BEA, ZSM-5), silicoaluminophosphate (SAPO-11, SAPO-231), mesoporous materials (MCM-41, AIMCM-41) [38,76,77].

Cracking is a reaction, which involves a rupture of the C-C bonds of hydrocarbons. It occurs upon acid active sites of solid surfaces after formation of carbocations [78].

The catalytic cracking of paraffins, like heptane, generally starts with their protonation by proton H^+ of the catalyst, after the formation of a five-ordered carbocation, followed protolytic cracking, thereby, forming the first carbenium ions and paraffins. The carbenium ions are normally transformed into alkenes, regenerating again the acid centers in which they were absorbed. The reaction proceeds through isomerization of carbocations. Many different species will suffer β-scission, producing an olefin and a new carbocation [79].

Oligomerization is a reaction that forms C-C bonds, yielding hydrocarbons which have a higher molecular weight. This reaction is favored at low temperature and high pressure. Oligomerization is an exothermic reaction; it causes a reduction in the number of molecules. This reaction is promoted by acid catalysts. The formed oligomers are cracked mainly at higher reaction temperatures, modifying the cracking products distribution [80,81].

Friedel-Crafts alkylation and acylation are among the most important reactions occurring over zeolites. They synthesize mainly alkyl and ketone aromatics for fine chemistry, pharmaceutical, cosmetics, agrochemical industries [82].

Alkylation of aromatics involves hydrogen substitution of an aromatic ring with alkyl group through interaction of an alkylating agent with the catalyst. The alkyl group is simultaneously added to the aromatic ring forming a complex σ as an intermediate (Figure 2-8) [83].

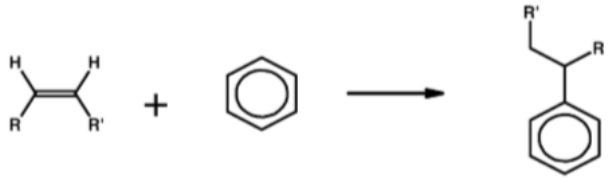

Figure 2-8 Friedel-Craft alkylation reaction [83].

Acylation reaction implies in the electrophilic substitution of an aromatic substrate with acyl, generally an acyl is halide, to form aromatic ketones (Figure 2-9) [84].

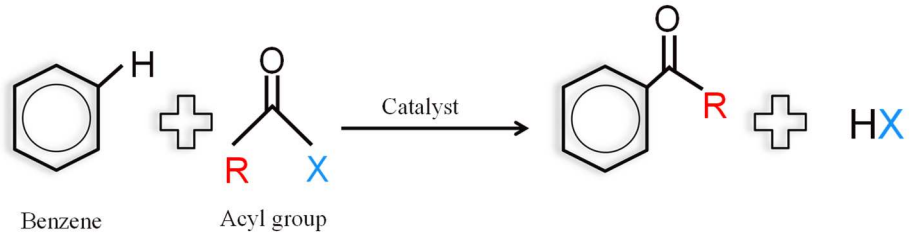

Figure 2-9 General acylation reaction adapted from [85].

The catalysts used in both reactions are Lewis acid or Brönsted acid such as Al_2O_4, $FeCl_3$, $TiCl_4$, HCl, HF. However, these catalysts present some disadvantages on the environmental disposal like toxicity and corrosion. In view of this, the development the new solid heterogeneous acid catalysts is highly demanding[71, 73, 86, 87].

Broad ranges of acidity, Si/Al ratios and crystalline structure are advantages of zeolites over other kinds of superacids materials [88]. Spagnol and co-workers were the first to propose application of the BEA zeolite for the acylation of anisole with acetic anhydride [89]. Zeolites such as BEA, ZSM-5 and Y [85,90–92] have been also used for the acylation and alkylation reactions [93].

2.2.2 Model reactions on metal sites

Hydrogenation/dehydrogenation reactions occur on the catalysts that have metallic functions (e.g. Pt, Pd, Rh). Metal sites can dehydrogenate saturated reactant molecules to alkenes and hydrogenate olefin intermediates desorbed from acid sites [78].

Thermodynamically, hydrogenation is likely to occur at low temperatures and high pressures, it is highly exothermic and causes a reduction in the number of molecules. The hydrogen activation is conducted by metal catalyst and causes a rupture of the H-H bond. An example can be seen for hydrogenation reaction of the ethylene molecule (Figure 2-10) and toluene (Figure 2-11) [94,95] .

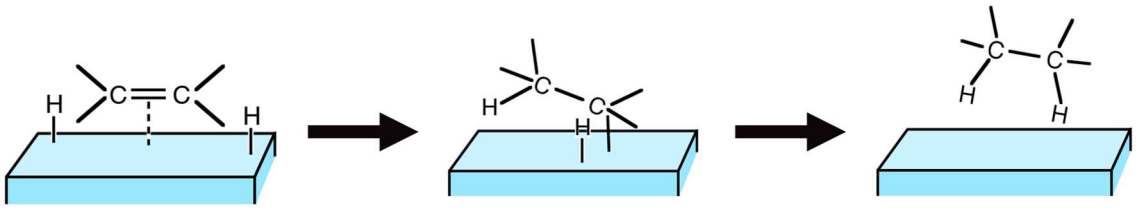

Figure 2-10 Ethylene hydrogenation reaction [96].

The interest to toluene hydrogenation has been increasing because of more strict requirements to the quality of diesel fuels as cetane number and the environmental legislative rules. Toluene has similar properties but lower toxicity than benzene, for these reasons it has been used in many applications replacing benzene. The Figure 2-11 shows toluene hydrogenation forming methyl-cyclohexane product and the catalytic cracking forming cyclohexane and methane as by-products [97–100].

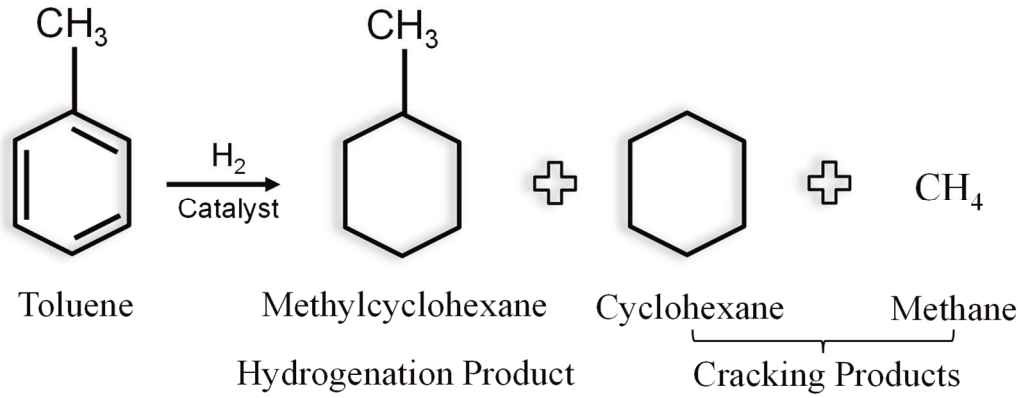

Figure 2-11 Toluene hydrogenation and product cracking [98].

2.2.3 Fischer-Tropsch Synthesis

Fischer Tropsch Synthesis (FTS) is a reaction that produces hydrocarbons from syngas (CO and H_2). The syngas is obtained from coal, natural gas, and biomass and is aimed for producing chemicals and fuels (Figure 2-12). FTS produces cleaner fuels and allows non-use or minimization of the use of petroleum resources [101–103]. The interest to FTS strongly depends on the crude oil prices, which vary cyclically over last decades. These days they are approaching 53 $ per barrel according to EIA, 2019.

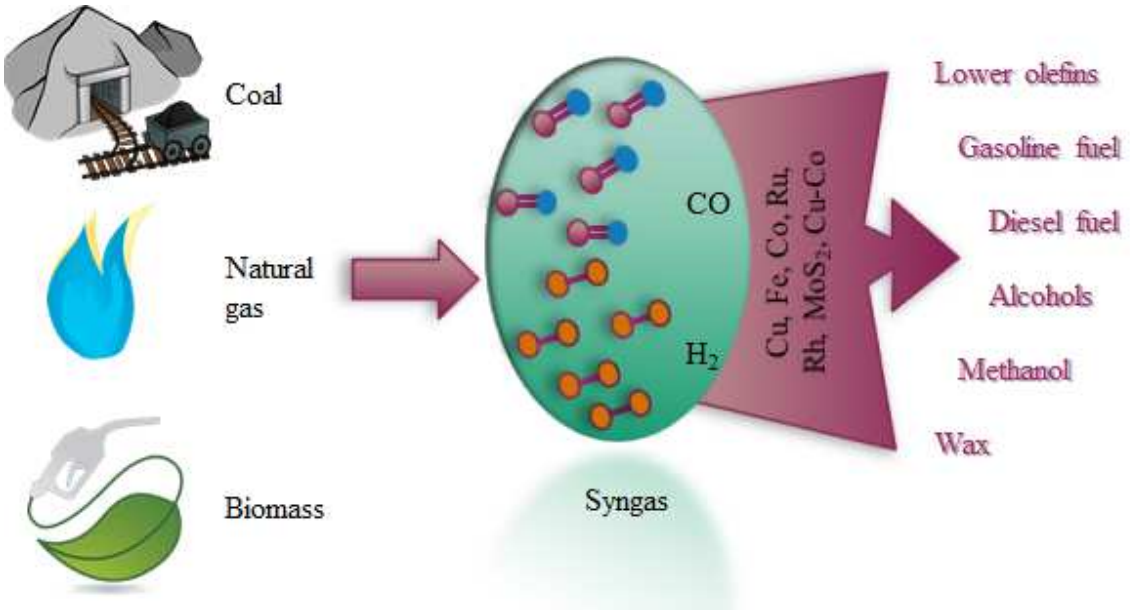

Figure 2-12 Conversion of non-petroleum sources to syngas for producing chemicals and liquids fuel (adapted from [104]).

Fischer Tropsch synthesis includes parallel and consecutive reactions, determined according to the operational conditions. Amongst them, the main are:

Paraffin synthesis: $(2n+1)\cdot H_2 + nCO \rightarrow C_nH_{2n+2} + nH_2O$

Olefin synthesis: $2n\cdot H_2 + nCO \rightarrow C_nH_{2n} + nH_2O$

Alcohol synthesis: $2n\cdot H_2 + nCO \rightarrow C_nH_{2n+1}OH + (n-1)\cdot H_2O$

Water Gas Shift (WGS): $CO + H_2O \rightarrow H_2 + CO_2$

Boudouard reaction (coke): $2CO \rightarrow C + CO_2$

Oxidation of metal: $xM + H_2O \rightarrow H_2 + MO_x$

In these reactions, n is the carbon number in hydrocarbons and alcohols. Several parameters can affect the performance of Fischer Tropsch synthesis, such as temperatures, composition of the gas (H_2/CO ratio) and type of catalysts.

There are two types of FT processes: High Temperature Fischer-Tropsch (HTFT) and Low Temperature Fischer-Tropsch (LTFT). The first process (HTFT) operates at high temperatures at the range from 320 to 350 ºC and uses iron as catalyst. It generates

olefins, oxygenates and paraffins of gasoline range. In the LTFT process, the reactions are carried out at lower temperatures (220 to 250 ºC) using iron or cobalt catalysts. The process produces mainly long-chain linear paraffins. Indeed, the LTFT synthesis will produce preferably middle distillates, which are used for formulation of diesel fuels [61].

The FT reaction mechanism consists of surface polymerization that yields a product distribution with different molecular weights, known as Anderson-Schulz-Flory (ASF) distribution [105]. The mechanism involves the following steps shown (Figure 2-13):

(1) Reagent adsorption;

(2) Chain initiation;

(3) Chain growth;

(4) Chain termination;

(5) Products desorption;

(6) Readsorption and secondary reactions.

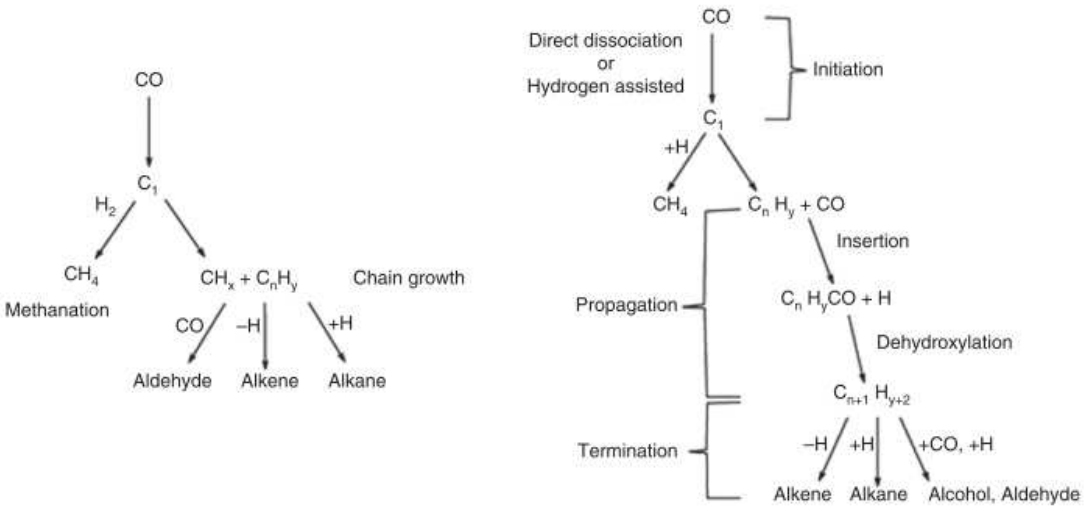

Figure 2-13 FTS mechanism [106].

The distribution of hydrocarbon products is described by the ASF distribution via Equation 1.

$$\alpha = \frac{r_p}{(r_p + r_t)} \quad (1)$$

where r_p is the initiation chain, r_t is the termination chain and α is the chain-growth probability. The chain growth towards olefins and paraffins is usually between 0.77 and 0.93 [107]. The termination probability will be (1-α). The relation between growth chain and molar fraction of a hydrocarbon is defined the Equation 2.

$$W_n = n(1-\alpha)^2\,\alpha^{n-1} \quad (2)$$

where W_n is a molar fraction of product with a carbon number n. The chain length distribution can be predicted by the Schulz-Flory law (Figure 2-14) [108].

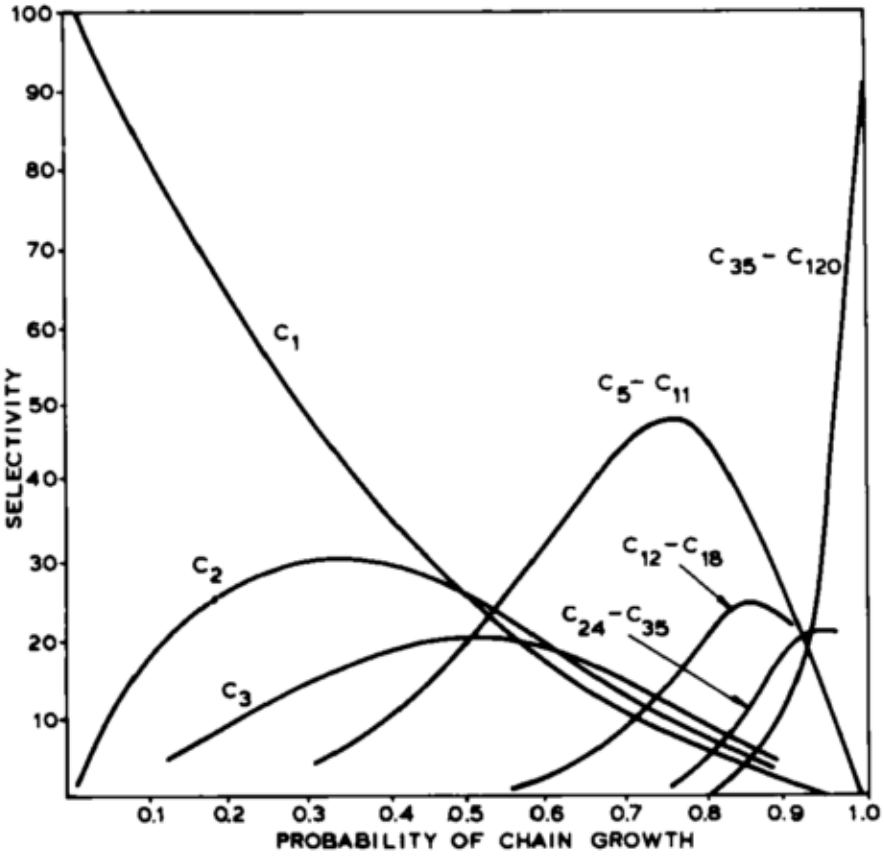

Figure 2-14 Hydrocarbon selectivity as α function [108].

Several methods have been proposed for selectivity control in FT synthesis. First, catalytic cracking/isomerization of FT hydrocarbons can upgrade the reaction products to a specific fuel. Combination of FT synthesis process with hydrocracking and

isomerization of long chain hydrocarbons restricts the hydrocarbon distribution to a more convenient range [109]. The isomerization and cracking of FT hydrocarbons would lead to iso-paraffins or diesel fuels constituted by the C_{10}-C_{20} hydrocarbons. This multistage process, however, significantly reduces the efficiency of synthetic fuel production.

An alternative to that multi-stage process would be utilization of bifunctional catalysts containing an active FT component, e.g. cobalt (Co) or ruthenium (Ru), and an acid catalyst active for cracking and isomerization. The proximity between metal and acid sites is an important parameter of the bifunctional catalysts often governing reaction rate and selectivities. Recently two additional methods for hydrocarbon selectivity control were proposed, which involve making use of nanoreactors [110] and microemulsions [111]. In these methods, the carbon chain length is limited by steric and diffusion limitations [112].

Fischer Tropsch mechanism is still under debates. Some mechanisms were proposed to literature which involve carbide, hydroxylcarbene and carbonyl insertion.

1) Surface carbide is formed firstly by CO and H_2 dissociation on metal particles supported, forming C_1 intermediates (without oxygen atoms). After that, the carbide reacts with adsorbed hydrogen, generating intermediates such as CH, CH_2 and/or CH_3, due to hydrogenation of carbon atoms. The chain growth is promoted by the insertion of CH_x species to C_xH_y, it is adsorbed into the metal particle. The chain termination is followed by: (i) dehydrogenation to olefins, (ii) hydrogenation of C_xH_y intermediates to paraffins or (iii) disproportional growth of C_xH_y intermediates to paraffins or olefins. Methylene (CH_2 adsorbed) is often considered the key intermediate specie (Figure 2-15).

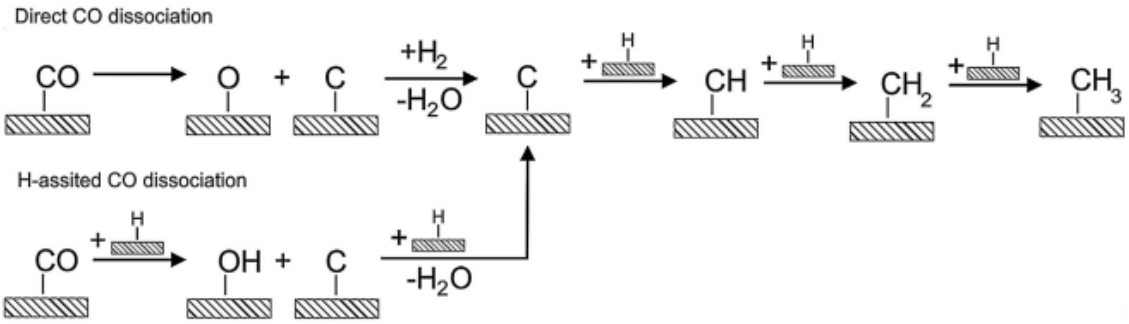

Figure 2-15 Carbene mechanism [113].

2) Hydroxycarbene mechanism entailing partial hydrogenation of adsorbed CO to adsorbed hydroxycarbene (CHOH) species. Thereafter, it involves a condensation reaction of two –CHOH species, with the elimination of water at the same time, forming – RCHOH intermediates (Figure 2-15).

This mechanism explains the formation of paraffinic and olefinic hydrocarbons by OH bond elimination.

3) Carbonyl insertion mechanism is essentially different of two mechanisms previously mentioned, because the CO molecule keeps unaltered. The growth of hydrocarbon chain occurs through CO insertion into the metal-alkyl bonds (Figure 2-16).

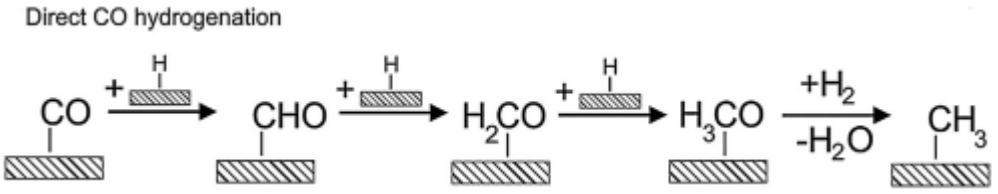

Figure 2-16 Schematic representation of carbonyl insertion [113].

Carbonyl insertion mechanism is based on the results obtained with organometallic complexes and was proposed for the first time by Pichler and Schulz (1970). When catalysts on the basis of ruthenium or iron are used, this mechanism is often supposed to occur [114].

2.2.4 Catalysts

The right choice of catalysts for the Fischer Tropsch synthesis is one the most important factors in order to obtain high reaction yield. The catalysts must be active, selective and stable. If it is possible, they can be regenerated. Several metals can be used as catalysts in this reaction, the main are: cobalt (Co), iron (Fe), ruthenium (Ru) and nickel (Ni) [115].

The iron catalysts normally are used because of their low cost. Besides that, these catalysts present a good performance using syngas rich in CO or CO_2, because of their high activity in the water gas shift reaction. The main disadvantages of iron catalysts is lower activity and rapid deactivation by oxidation or sintering [116].

Ruthenium is the most active catalyst for Fischer Tropsch synthesis, but its high cost and limited reserves make it impossible industrial application. [117,118].

Cobalt-based catalysts present high activity, stability, C_5^+ hydrocarbons selectivity and low activity in the WGS reaction. Cobalt catalysts are used in the low temperature process (LTFT- Low Temperature Fischer Tropsch synthesis) for synthesis of diesel fuels, whereas at high temperatures they produce a lot of methane (CH_4). Besides that, these catalysts have high activity in hydrogenation and tend to form preferably linear alkanes, undesirable in the gasoline production, one of the main products of HTFT process [119, 120]. In the state of the art catalysts, cobalt nanoparticles are dispersed on porous supports like Al_2O_3, TiO_2, SiO_2, zeolites and others [9,121,122]. Higher activity, higher conversion per single pass, higher resistance to deactivation by water, lower activity in WGS and lower amount of oxygenate products are main advantages that cobalt presents in front of iron-based catalysts.

References

1. Shlögl, R. Combinatorial Chemistry in Heterogeneous Vatalysis: A New Scientific Approch or ¨the King's New Clothes"? *Angewandte Chemie International Edition* (1998).

2. Plana-pallejà, J., Abelló, S., Berrueco, C. & Montané, D. Applied Catalysis A : General Effect of zeolite acidity and mesoporosity on the activity of Fischer – Tropsch Fe / ZSM-5 bifunctional catalysts. **515,** 126–135 (2016).

3. Lee, W. *et al.* Effects of hierarchical zeolites on aromatization of acetylene. *Catal. Today* **303,** 177–184 (2018).

4. Jia, X., Khan, W., Wu, Z., Choi, J. & Yip, A. C. K. Modern synthesis strategies for hierarchical zeolites: Bottom-up versus top-down strategies. *Adv. Powder Technol.* (2018). doi:10.1016/j.apt.2018.12.014

5. Feliczak-Guzik, A. Hierarchical zeolites: Synthesis and catalytic properties. *Microporous Mesoporous Mater.* **259,** 33–45 (2018).

6. Emdadi, L. *et al.* Synthesis of hierarchical lamellar MFI zeolites with sequential intergrowth influenced by synthetic gel composition. *Microporous Mesoporous Mater.* **275,** 31–41 (2019).

7. Weitkamp, J. Zeolites and Catalysis. *Solide State Ionics* **131,** 175–188 (2000).

8. Deldari, H. Suitable catalysts for hydroisomerization of long-chain normal paraffins. *Appl. Catal. A Gen.* **293,** 1–10 (2005).

9. Steen, E. Van *et al.* TPR Study on the Preparation of Impregnated Co / SiO 2 Catalysts. **229,** 220–229 (1996).

10. Schwarz, J. A., Contescu, C. & Contescu, A. Methods for Preparation of Catalytic Materials. *Chem. Rev.* **95,** 477–510 (1995).

11. Almas, Q., Sievers, C. & Jones, C. W. Role of themesopore generation method in structure, activity and stability of MFI catalysts in glycerol acetylation. *Appl. Catal. A Gen.* **571,** 107–117 (2019).

12. Huang, Z. *et al.* Promoting effects of desilication and dealumination on the catalytic performance of Al-rich HMOR for catalysing naphthalene tert-butylation with tertiary butanol. *Appl. Catal. A Gen.* **572,** 80–89 (2019).

13. Moliner, M. Direct Synthesis of Functional Zeolitic Materials. *ISRN Mater. Sci.* **2012,** 1–24 (2012).

14. Koohsaryan, E. & Anbia, M. Nanosized and hierarchical zeolites : A short review. **37,** 447–467 (2016).

15. Fang, Y., Hu, H. & Chen, G. Zeolite with tunable intracrystal mesoporosity synthesized with carbon aerogel as a secondary template. **113,** 481–489 (2008).

16. Kustova, M., Egeblad, K., Christensen, C. H., Kustov, A. L. & Christensen, C. H. in *Studies in Surface Science and Catalysis* **170,** 267–275 (2007).

17. Zhang, K. & Ostraat, M. L. Innovations in hierarchical zeolite synthesis. *Catal. Today* **264,** 3–15 (2016).

18. Serrano, D. P., Escola, J. M. & Pizarro, P. Synthesis strategies in the search for hierarchical zeolites. *Chem. Soc. Rev.* **42,** 4004–4035 (2013).

19. Kharchenko, A. Properties of copper species stabilized in zeolite nanocrystals. (Normandie Université, 2017).

20. Silva Filho, S. H. da *et al.* Synthesis of Zeolite A employing Amazon kaolin waste. *Cerâmica* **61,** 409–413 (2015).

21. Sklenak, S. *et al.* N2O decomposition over Fe-zeolites: Structure of the active sites and the origin of the distinct reactivity of Fe-ferrierite, Fe-ZSM-5, and Fe-beta. A combined periodic DFT and multispectral study. *J. Catal.* **272,** 262–274 (2010).

22. Odedairo, T., Balasamy, R. J. & Al-Khattaf, S. Influence of mesoporous materials containing ZSM-5 on alkylation and cracking reactions. *J. Mol. Catal. A Chem.* **345,** 21–36 (2011).

23. Mihailova, B. *et al.* Interlayer stacking disorder in zeolite beta family: A Raman spectroscopic study. *Phys. Chem. Chem. Phys.* **7,** 2756–2763 (2005).

24. Díaz-Cabañas, M. J. *et al.* Synthesis and structure of polymorph B of Beta zeolite. *Stud. Surf. Sci. Catal.* **174,** 233–236 (2008).

25. Na, R. *et al.* Comptes Rendus Chimie Transformation of South African coal fl y ash into ZSM-5 zeolite and its application as an MTO catalyst. *Comptes rendus - Chim.* **20,** 78–86 (2017).

26. Wang, Y., Ma, J., Ren, F., Du, J. & Li, R. Hierarchical architectures of ZSM-5 nanocrystalline aggregates with particular catalysis for lager molecule reaction. *Microporous Mesoporous Mater.* **240,** 22–30 (2017).

27. Lounis, Z. & Belarbi, H. The Nanostructure Zeolites MFI-Type ZSM5. *Nanocrystals and Nanostructures* 43–62 (2018). doi:10.5772/intechopen.77020

28. Pérez-Ramírez, J., Christensen, C. H., Egeblad, K., Christensen, C. H. & Groen, J. C. Hierarchical zeolites: enhanced utilisation of microporous crystals in catalysis by advances in materials design. *Chem. Soc. Rev.* **37,** 2530 (2008).

29. Bassan, Í. A. L. Catalisadores bifuncionais à base de silicoaluminofosfato e fosfatos de nióbio para emprego em reações de hidroisomerização e hidrocraqueamento do n-hexadecano. (2015).

30. Schwieger, W. *et al.* Hierarchy concepts: Classification and preparation strategies for zeolite containing materials with hierarchical porosity. *Chem. Soc. Rev.* **45,** 3353–3376 (2016).

31. Deng, Z., Zhang, Y., Zhu, K., Qian, G. & Zhou, X. Carbon nanotubes as transient inhibitors in steam-assisted crystal- lization of hierarchical ZSM-5 zeolites. **159,** 466–469 (2015).

32. Groen, J. C., Moulijn, J. A. & Pérez-Ramírez, J. Decoupling mesoporosity formation and acidity modification in ZSM-5 zeolites by sequential desilication-dealumination. *Microporous Mesoporous Mater.* **87,** 153–161 (2005).

33. Groen, J. C., Jansen, J. C., Moulijn, J. A. & Pérez-Ramírez, J. Optimal aluminum-assisted mesoporosity development in MFI zeolites by desilication. *J. Phys. Chem. B* **108,** 13062–13065 (2004).

34. Milina, M., Mitchell, S., Crivelli, P., Cooke, D. & Pérez-Ramírez, J. Mesopore quality

determines the lifetime of hierarchically structured zeolite catalysts. *Nat. Commun.* **5,** 1–10 (2014).

35. Groen, J. C. *et al.* Creation of hollow zeolite architectures by controlled desilication of A1-zoned ZSM-5 crystals. *J. Am. Chem. Soc.* **127,** 10792–10793 (2005).

36. Dai, G., Hao, W., Xiao, H., Ma, J. & Li, R. Hierarchical mordenite zeolite nano-rods bundles favourable to bulky molecules. *Chem. Phys. Lett.* **686,** 111–115 (2017).

37. M. Opanasenko. Zeolite constructor kit: Design for catalytic applications. *Catal. Today* **304,** 2–11 (2018).

38. Chunfei Zhang, Hao Chen, Xiangwen Zhang, Q. W. TPABr-grafted MWCNT as bifunctional template to synthesize hieraschical ZSM-5 zeolite. *Mater. Lett.* **197,** 111–114 (2017).

39. Huang, G. *et al.* Fast synthesis of hierarchical Beta zeolites with uniform nanocrystals from layered silicate precursor. *Microporous Mesoporous Mater.* **248,** 30–39 (2017).

40. Saito, A. & Foley, H. C. Micelle-templated silicates as a test bed for methods of mesopore size evaluation. *Microporous Mater.* **3,** 531–542 (1995).

41. Karlsson, A., Stöcker, M. & Schmidt, R. Composites of micro- and mesoporous materials: simultaneous syntheses of MFI/MCM-41 like phases by a mixed template approach. *Microporous Mesoporous Mater.* **27,** 181–192 (1999).

42. Zhu, K., Sun, J., Zhang, H., Liu, J. & Wang, Y. Carbon as a hard template for nano material catalysts. *J. Nat. Gas Chem.* **21,** 215–232 (2012).

43. Liu, J. *et al.* Hierarchical Macro-meso-microporous ZSM-5 Zeolite Hollow Fibers With Highly Efficient Catalytic Cracking Capability. *Sci. Rep.* **4,** 1–6 (2014).

44. Shcherban, N. D., Ilyin, V. G. & Nauky, P. Preparation , physicochemical properties and functional characteristics of micromesoporous zeolite materials. *Theor. Exp. Chem.* **51,** 331–349 (2016).

45. Verboekend, D., Chabaneix, A. M., Thomas, K., Gilson, J.-P. & Pérez-Ramírez, J. Mesoporous ZSM-22 zeolite obtained by desilication: peculiarities associated with

crystal morphology and aluminium distribution. *CrystEngComm* **13,** 3408 (2011).

46. Chen, L.-H. *et al.* Hierarchically structured zeolites: synthesis, mass transport properties and applications. *J. Mater. Chem.* **22,** 17381 (2012).

47. Chuang XIng, Guohui Yang, Peng Lu; Wenzhong Shen, Xikun Gai, Li Tan, Jianwei, Tiejun Wang, Ruiqin Yang, N. T. A hierarchically spherical Co-based zeolite catalyst with aggregated nanorods structure for improved FischereTropsch synthesis reaction activity and isoparaffin selectivity. *Microporous Mesoporous Mater.* **233,** 62–69 (2016).

48. Luna, F. J. & Schuchardt, U. Modificação de zeólitas para uso em catálise. *Quim. Nova* **24,** 885–892 (2001).

49. Stöcker, M. Gas phase catalysis by zeolites. *Microporous Mesoporous Mater.* **82,** 257–292 (2005).

50. Corma, A. Inorganic Solid Acids and Their Use in Acid-Catalyzed Hydrocarbon Reactions. *Chem. Rev.* **95,** 559–614 (1995).

51. Juzsakova, T. *et al.* Study on the Alkylaton Mechanism of Isobutane With 1-Butene Using Environmental Friendly Catalysts. *Environ. Eng. Manag. J.* **13,** 2343–2347 (2014).

52. Li, S. *et al.* Extra-framework aluminium species in hydrated faujasite zeolite as investigated by two-dimensional solid-state NMR spectroscopy and theoretical calculations. *Phys. Chem. Chem. Phys.* **12,** 3895 (2010).

53. Gackowski, M., Kuterasiński, Ł., Podobiński, J., Sulikowski, B. & Datka, J. IR and NMR studies of hierarchical material obtained by the treatment of zeolite Y by ammonia solution. *Spectrochim. Acta - Part A Mol. Biomol. Spectrosc.* **193,** 440–446 (2018).

54. Zhang, W. & Smirniotis, P. G. Effect of zeolite structure and acidity on the product selectivity and reaction mechanism for n-octane hydroisomerization and hydrocracking. *J. Catal.* **182,** 400–416 (1999).

55. Farneth, W. E. & Gorte, R. J. Methods for Characterizing Zeolite Acidity. *Chem. Rev.* **95,** 615–635 (1995).

56. Dias, S. C. L. & Dias, J. A. Effects of the dealumination methodology on the FER

zeolite acidity: A study with fractional factorial design. *Mol. Catal.* **458,** 139–144 (2018).

57. Weisz, P. B. Polyfunctional Heterogeneous Catalysis. *Adv. Catal.* **13,** 137–190 (1962).

58. Song, Y. Q. *et al.* Effect of variations in pore structure and acidity of alkali treated ZSM-5 on the isomerization performance. *J. Mol. Catal. A Chem.* **310,** 130–137 (2009).

59. Z.B. Wang, A. Kamo, T. Yoneda, T. Komatsu, T. Y. Isomerization of n-heptane over Pt-loaded zeolite/3 catalysts. *Appl. Catal. A Gen.* **159,** 119–132 (1997).

60. Bao, J., Yang, G., Okada, C., Yoneyama, Y. & Tsubaki, N. H-type zeolite coated iron-based multiple-functional catalyst for direct synthesis of middle isoparaffins from syngas. *Appl. Catal. A Gen.* **394,** 195–200 (2011).

61. Sartipi, S. Bifunctional catalysts for the direct production of liquid fuels from syngas. (Delft University of Technology The, 2014).

62. Miyaji, A. *et al.* Selectivity and mechanism for skeletal isomerization of alkanes over typical solid acids and their Pt-promoted catalysts. *Catal. Today* **74,** 291–297 (2002).

63. Chica, A., Corma, A. & Miguel, P. J. Isomerization of C 5 – C 7 n -alkanes on unidirectional large pore zeolites : activity , selectivity and adsorption features. **65,** 101–110 (2001).

64. Kinger, G., Majda, D. & Vinek, H. N-heptane hydroisomerization over Pt-containing mixtures of zeolites with inert materials. *Appl. Catal. A Gen.* **225,** 301–312 (2002).

65. Cejka, J., Bekkum, H. van, Avelino, C. & Ferdi, S. *Introduction to Zeolite Science and Practice*. (Elsevier Science, 2007).

66. Deraz, N. M. The comparative jurisprudence of catalysts preparation methods: I. Deposition-precipitation and adsorption methods. *J. Ind. Environ. Chem.* **2,** 1–3 (2018).

67. Rasouli, M., Atashi, H., Mohebbi-kalhori, D. & Yaghobi, N. Bifunctional Pt/Fe-ZSM-5 catalyst for xylene isomerization. *J. Taiwan Inst. Chem. Eng.* **78,** 438–446 (2017).

68. Hou, X., Qiu, Y., Yuan, E., Zhang, X. & Liu, G. SO4 2−/TiO2 promotion on HZSM-

5 for catalytic cracking of paraffin. *"Applied Catal. A, Gen.* **537,** 12–23 (2017).

69. Chao, L. I., Hui, W., Shan-shan, Z. H. U., Guang-bo, L. I. U. & Jin-hu, W. U. Research on butene oligomerization reaction over the hemicellulose modified HZSM-5. *J. Fuel Chem. Technol.* **45,** 1088–1094 (2017).

70. Rui, J. *et al.* Synthesized high-silica hierarchical porous ZSM-5 and optimization of its reaction conditions in benzene alkylation with methanol. *Chinese Chem. Lett.* **30,** 757–761 (2019).

71. Aleixo, R. *et al.* Kinetic study of Friedel-Crafts acylation reactions over hierarchical MCM-22 zeolites. *Mol. Catal.* **434,** 175–183 (2017).

72. S.G. Wagholikar, P.S. Niphadkar, S. Mayadevi, S. S. Acylation of ansiole with long-chain carboxylic acids over wide pore zeolites. *Appl. Catal. A Gen.* **317,** 250–257 (2007).

73. Chen, Z., Feng, Y., Tong, T. & Zeng, A. Effects of acid-modified HBEA zeolites on thiophene acylation and the origin of deactivation of zeolites. *Appl. Catal. A Gen.* **482,** 92–98 (2014).

74. Olah, G. A.; Prakash, G. K. S.; Molnar, Á.; Sommar, J. *Superacid Chemistry*. *John Wiley & Sons, Inc.* (2009). doi:10.1002/9780470421604

75. Steijns, M. & Froment, G. F. Hydroisomerization and Hydrocracking. 3. Kinetic Analysis of Rate Data for n-Decane and n-Dodecane. *Ind. Eng. Chem. Prod. Res. Dev.* **20,** 660–668 (1981).

76. Sartipi, S., Van Dijk, J. E., Gascon, J. & Kapteijn, F. Toward bifunctional catalysts for the direct conversion of syngas to gasoline range hydrocarbons: H-ZSM-5 coated Co versus H-ZSM-5 supported Co. *Appl. Catal. A Gen.* **456,** 11–22 (2013).

77. Bessell, S. Investigation of bifunctional zeolite supported cobalt Fischer-Tropsch catalysts. *Appl. Catal. A, Gen.* **126,** 235–244 (1995).

78. Weitkamp, J. Catalytic Hydrocracking-Mechanisms and Versatility of the Process. *ChemCatChem* **4,** 292–306 (2012).

79. Corma, A., Planelles, J. & Tomás, F. The influence of branching isomerization on the

product distribution obtained during cracking of n-heptane on acidic zeolites. *J. Catal.* **94,** 445–454 (1985).

80. Jentoft, F. C. & Gates, B. C. Solid-acid-catalyzed alkane cracking mechanisms: Evidence from reactions of small probe molecules. *Top. Catal.* **4,** 1–13 (1997).

81. Kotrel, S., Knözinger, H. & Gates, B. C. The Haag-Dessau mechanism of protolytic cracking of alkanes. *Microporous Mesoporous Mater.* **35–36,** 11–20 (2000).

82. Narayanan, S. & Deshpande, K. *Aniline alkylation over solid acid catalysts*. *Applied Catalysis A: General* **199,** (2000).

83. Kocal, J. A., Vora, B. V. & Imai, T. Production of linear alkylbenzenes. *Appl. Catal. A Gen.* **221,** 295–301 (2001).

84. Gore, P. H. The Friedel-Crafts Acylation Reaction and its Application to Polycyclic Aromatic Hydrocarbons. *Chem. Rev.* **55,** 229–281 (1955).

85. Kim, J. C., Cho, K., Lee, S. & Ryoo, R. Mesopore wall-catalyzed Friedel-Crafts acylation of bulky aromatic compounds in MFI zeolite nanosponge. *Catal. Today* **243,** 103–108 (2015).

86. Bernardon, C., Ben Osman, M., Laugel, G., Louis, B. & Pale, P. Acidity versus metal-induced Lewis acidity in zeolites for Friedel–Crafts acylation. *Comptes Rendus Chim.* **20,** 20–29 (2017).

87. Kubů, M. *et al.* Three-dimensional 10-ring zeolites: The activities in toluene alkylation and disproportionation. *Catal. Today* **259,** 97–106 (2016).

88. Corma, A., José Climent, M., García, H. & Primo, J. Design of synthetic zeolites as catalysts in organic reactions. *Appl. Catal.* **49,** 109–123 (1989).

89. Bonati, M. L. M., Joyner, R. W. & Stockenhuber, M. On the mechanism of aromatic acylation over zeolites. *Microporous Mesoporous Mater.* **104,** 217–224 (2007).

90. Srivastava, R. Synthesis and applications of ordered and disordered mesoporous zeolites: Present and future prospective. *Catal. Today* **309,** 172–188 (2018).

91. Procházková, D., Kurfiřtová, L. & Pavlatová, J. Acylation of p-xylene over zeolites. *Catal. Today* **179,** 78–84 (2012).

92. Kantam, M. L., Ranganath, K. V. S., Sateesh, M., Kumar, K. B. S. & Choudary, B. M. Friedel-Crafts acylation of aromatics and heteroaromatics by beta zeolite. *J. Mol. Catal. A Chem.* **225,** 15–20 (2005).

93. Bernardon, C. Catalyseurs « Verts » Pour La Synthese Organique : (Université de Strasbourg, 2016).

94. Yadav, R. & Sakthivel, A. Silicoaluminophosphate molecular sieves as potential catalysts for hydroisomerization of alkanes and alkenes. *Appl. Catal. A Gen.* **481,** 143–160 (2014).

95. Arribas, M. A., Concepción, P. & Martínez, A. The role of metal sites during the coupled hydrogenation and ring opening of tetralin on bifunctional Pt(Ir)/USY catalysts. *Appl. Catal. A Gen.* **267,** 111–119 (2004).

96. Batalha, N. M. R. Optimization of the balance between activity and selectivity on a hydroisomerization catalyst. (Université de Poitiers, 2012).

97. Szegedi, Á., Popova, M., Mavrodinova, V. & Minchev, C. Cobalt-containing mesoporous silicas-Preparation, characterization and catalytic activity in toluene hydrogenation. *Appl. Catal. A Gen.* **338,** 44–51 (2008).

98. Loiha, S. *et al.* Catalytic enhancement of platinum supported on zeolite beta for toluene hydrogenation by addition of palladium. *J. Ind. Eng. Chem.* **15,** 819–823 (2009).

99. Hashemi, M., Teymouri, M., Rashidi, A. & Khodaei, M. M. Mesoporous catalyst of Co/MWCNTs as an effective catalyst in toluene hydrogenation and data analysis using response surface methodology (RSM). *Mater. Lett.* **126,** 253–258 (2014).

100 .Suppino, R. S., Landers, R. & Cobo, A. J. G. Influence of noble metals (Pd, Pt) on the performance of Ru/Al2O3based catalysts for toluene hydrogenation in liquid phase. *Appl. Catal. A Gen.* **525,** 41–49 (2016).

101. Xiong, H., Motchelaho, M. A. M., Moyo, M., Jewell, L. L. & Coville, N. J. Correlating the preparation and performance of cobalt catalysts supported on carbon nanotubes and carbon spheres in the Fischer – Tropsch synthesis. *J. Catal.* **278,** 26–40

(2011).

102. Wen, X. *et al.* Performance of hierarchical ZSM-5 supported cobalt catalyst in the Fischer-Tropsch synthesis. *J. Fuel Chem. Technol.* **45,** 950–955 (2017).

103. Yuelun Wang, Yuan Jiang, Juan Huang, Jing Liang, Hui Wang, Zhuo Li, Jinhu Wu, Min Li, Yunpeng Zhao, J. N. Effect of hierarchical crystal structures on the properties of cobalt catalysts for Fischer–Tropsch synthesis. *Fuel* **174,** 17–24 (2016).

104. Carvalho, A. A. B. Investigation of intrinsic activity of cobalt and iron based Fischer-Tropsch catalysts using transient kinetic methods. (Université de Lille, 2017).

105. van Wechem, V. M. H. & Senden, M. M. G. Conversion of natural gas to transportation fuels via the shell middle distillate synthesis process(smds). *Stud. Surf. Sci. Catal.* **81,** 43–71 (1994).

106. Gholami, Z., Asmawati Mohd ZabiDi, N., Gholami, F., Ayodele, O. B. & Vakili, M. The influence of catalyst factors for sustainable production of hydrocarbons via Fischer-Tropsch synthesis. *Rev. Chem. Eng.* **33,** 337–358 (2017).

107. Khodakov, A. Y., Chu, W. & Fongarland, P. Advances in the development of novel cobalt Fischer-Tropsch catalysts for synthesis of long-chain hydrocarbons and clean fuels. *Chem. Rev.* **107,** 1692–1744 (2007).

108. King, F., Shutt, E. & Thornson, A. I. Ruthenium Catalyst Systems for the Production of Hydrocarbons from Coal recent studies on the fischer-tropsch reaction Process Developments. 146–154 (1985).

109. Bouchy, C., Hastoy, G., Guillon, E. & Martens, J. A. Fischer-Tropsch waxes upgrading via hydrocracking and selective hydroisomerization. *Oil Gas Sci. Technol.* **64,** 91–112 (2009).

110. Subramanian, V., Cheng, K., Lancelot, C. & Heyte, S. Nanoreactors: An E ffi cient Tool To Control the Chain-Length Distribution in Fischer − Tropsch Synthesis †. (2016). doi:10.1021/acscatal.5b01596

111. Ordomsky, V. V., Khodakov, A. Y., Legras, B. & Lancelot, C. Fischer–Tropsch synthesis on a ruthenium catalyst in two-phase systems: an excellent opportunity for the control of reaction rate and selectivity. *Catal. Sci. Technol.* **4,** 2896–2899 (2014).

112. Li, Z., Wu, L., Han, D. & Wu, J. Characterizations and product distribution of Co-based Fischer-Tropsch catalysts: A comparison of the incorporation manner. *Fuel* **220,** 257–263 (2018).

113. Todic, B., Ma, W., Jacobs, G., Davis, B. H. & Bukur, D. B. CO-insertion mechanism based kinetic model of the Fischer – Tropsch synthesis reaction over Re-promoted Co catalyst. *Catal. Today* **228,** 32–39 (2014).

114. Yang, J. *et al.* Reaction mechanism of CO activation and methane formation on Co Fischer-Tropsch catalyst: A combined DFT, transient, and steady-state kinetic modeling. *J. Catal.* **308,** 37–49 (2013).

115. Bessell, S. Support effects in cobalt-based fischer-tropsch catalysis. *Appl. Catal. A, Gen.* **96,** 253–268 (1993).

116. Plana-pallejà, J., Abelló, S., Berrueco, C. & Montané, D. Effect of zeolite acidity and mesoporosity on the activity of Fischer – Tropsch Fe/ZSM-5 bifunctional catalysts. *Appl. Catal. A Gen.* **515,** 126–135 (2016).

117. Phaahlamohlaka, T. N., Kumi, D. O., Dlamini, M. W., Jewell, L. L. & Coville, N. J. Ruthenium nanoparticles encapsulated inside porous hollow carbon spheres: A novel catalyst for Fischer–Tropsch synthesis. *Catal. Today* **275,** 76–83 (2016).

118. Kang, J. *et al.* Mesoporous zeolite-supported ruthenium nanoparticles as highly selective fischer-tropsch catalysts for the production of C5-C11 isoparaffins. *Angew. Chemie - Int. Ed.* **50,** 5200–5203 (2011).

119. Yang, J., Ma, W., Chen, D., Holmen, A. & Davis, B. H. Fischer-Tropsch synthesis: A review of the effect of CO conversion on methane selectivity. *Appl. Catal. A Gen.* **470,** 250–260 (2014).

120. Zhang, Y., Xiong, H., Liew, K. & Li, J. Effect of magnesia on alumina-supported cobalt Fischer-Tropsch synthesis catalysts. *J. Mol. Catal. A Chem.* **237,** 172–181 (2005).

121. Martínez, A., López, C., Márquez, F. & Díaz, I. Fischer-Tropsch synthesis of hydrocarbons over mesoporous Co/SBA-15 catalysts: The influence of metal loading, cobalt precursor, and promoters. *J. Catal.* **220,** 486–499 (2003).

122. Liu, Y., Dintzer, T., Ersen, O. & Pham-Huu, C. Carbon nanotubes decorated ??-

Al_2O_3 containing cobalt nanoparticles for Fischer-Tropsch reaction. *J. Energy Chem.* **22,** 279–289 (2013).

Chapter 3: Influence of impregnation and ion exchange sequence on metal localization, acidity and catalytic performance of cobalt zeolite catalysts in Fischer-Tropsch synthesis

Paper published in ChemCatChem, October 2018, IF 4.67, Qualis A1.

Abstract: Cobalt distribution between the external surface and micropores and acidity of the large pore BEA zeolite were controlled by choosing the sequence of impregnation and ion exchange procedures. Higher concentration of ion exchangeable cobalt was observed in the catalyst prepared by ion-exchange of the zeolite proton form. The presence of Na^+ instead of H^+ ions in the exchange positions of zeolite favored deposition of cobalt on the external surface. The acid sites in the zeolite micropores can be then restored by subsequent ion exchange of sodium with ammonium nitrate and calcination. The catalytic performance of the cobalt zeolite catalysts prepared using different impregnation and ion exchange procedures was tested in the Fischer-Tropsch synthesis. Higher reaction rates were observed over the catalysts, which did not contain cobalt ions in the cation sites of the zeolite. Lower methane selectivity, higher selectivity to long chain hydrocarbons and high fraction of isomerized products are observed when cobalt species are located on the zeolite outer surface and acid sites inside the BEA zeolite micropores.

3.1 Introduction

The depletion of fossil resources and increasing environmental concerns have led to the development of new catalytic processes from alternative and renewable feedstocks. Natural gas and biomass can be transformed into syngas ($CO+H_2$) by steam reforming, partial oxidation or gasification. The syngas can be then converted into ultra-clean fuels

over cobalt-based catalysts via Fischer-Tropsch (FT) synthesis [1-3] FT synthesis is a "nontrivial surface polymerization reaction" [4], with the reaction selectivity typically described by very broad Anderson-Schulz-Flory distribution [1, 5]. Consequently, the major challenge of FT reaction is adjustment of the reaction selectivity in order to produce specific hydrocarbon fractions.

Several methods were proposed for selectivity control in FT synthesis. Some of them involve control of hydrocarbon selectivity by steric limitation and diffusion in nanoreactors and microemlusions [6-8]. The combination of FT synthesis with hydrocracking and isomerization of long-carbon chain hydrocarbons restricts the hydrocarbon distribution to a more convenient narrow range [9, 10]. Isomerization and cracking of FT hydrocarbons would lead to iso-paraffins or diesel fuels mostly constituted by the C_{10}-C_{20} hydrocarbons. This reaction can be performed over hybrid or composite catalysts containing an active FT component, e.g. Co or Ru, and an acid catalyst active in cracking and isomerization.

Because of their high acidity and stability, zeolites have been often proposed as most promising catalysts for hydrocarbon cracking and isomerization under FT synthesis conditions [3, 11]. Impregnation is an effective method for the preparation of bi-functional cobalt-zeolite catalysts for the direct production of fuels from syngas [12-18]. Note however, that introduction of cobalt ions to the zeolite may result however, in the neutralization of the zeolite acid sites. This represents a major drawback of this method. Cobalt ions, introduced during impregnation, can occupy cation exchange positions in the zeolite micropores decreasing the number of acid sites available for hydrocarbon isomerization and cracking. In addition, the isolated Co ions in the cationic positions can be very difficult to reduce to metallic state, thus decreasing the amount of available metal active phase for FT synthesis. Finally, it is known that the diffusion in zeolites is strongly

affected by the presence of exchange cations inside the micropores [19-21]. The metal particles in the narrow zeolite micropores are more susceptible to suffer from diffusion limitations due to the small pores of the zeolite in the presence of larger compensation cations. The diffusion limitations in the zeolite micropores in particular for carbon monoxide would lead to higher methane selectivity [22]. In addition, use of larger compensation cations during impregnation can restrain diffusion of Co ions inside the zeolite pores during the ion exchange and thus affect cobalt distribution between the zeolite external surface and micropores of the zeolite. The diffusion of reagents, intermediates and reaction products is usually much faster in the H-from of the zeolites and more particularly in the BEA zeolite, which has larger pore diameters compared to mordenite and most commonly used ZSM-5 zeolite. It can be also expected that HBEA zeolite which has weaker Brönsted acidity [13] than H-ZSM-5 might reduce overcracking and exhibit higher selectivity to isomerized hydrocarbons.

This chapter focuses on the effect of the impregnation sequence while introducing cobalt ions on the metal localization in zeolite and catalytic performance in FT synthesis. Cobalt was introduced by impregnation either to the sodium or proton forms of BEA zeolite. The as-prepared cobalt zeolite catalysts were calcined after the impregnation and then submitted to NH_4^+ ion exchange. The Brönsted acidity was restored in the zeolite by decomposition of NH_4^+ ions at higher temperature. All samples, before and after regeneration of the acid sites, were characterized by a wide range of methods and tested in FT synthesis.

3.2 Experimental Section

Catalyst synthesis

A commercial NH_4BEA zeolite (Zeolyst, CP-814E, Si/Al=12.5) was used for preparation of all catalysts. The H^+ form of the BEA zeolite (HBEA) was obtained via calcination of the parent NH_4BEA sample at 450 °C for 4 h. The Na^+ form (NaBEA) was prepared by two successive ion exchanges of HBEA with a 2 M NaCl (Janssen Chimica, P.A) solution at 80 °C for 1 h (50 mL·gsample^{-1}), followed by calcination at 450 °C for 4 h. Cobalt and platinum were introduced to the HBEA and NaBEA zeolites through incipient wetness impregnation by using $Co(NO_3)_2$ (2.39 mol L^{-1} solution) (Sigma-Aldrich, 98%) and $Pt(NH_3)_4(NO_3)_2$ (Sigma-Aldrich) as precursors. The amounts of precursors were calculated to obtain 20 wt.% of cobalt and 0.1 wt.% platinum in the final samples. After the impregnation, the samples were calcined at 450 °C for 4 h. The impregnated HBEA and NaBEA are denoted as Co/HBEA and Co/NaBEA, respectively.

The calcined Co/HBEA and Co/NaBEA catalysts were submitted to two successive ion exchanges with 2 M NH_4NO_3 (Sigma-Aldrich, 98%) solution at 80 °C for 1 h (50 mL•gsample^{-1}), followed by calcination at 450 °C for 4 h. The final samples after the ion exchange with NH_4^+ and calcination are denoted as CoH/HBEA and CoH/NaBEA.

Catalyst characterization

The calcined samples were characterized by X-ray diffraction (XRD) by using a D8 Advance diffractometer equipped with an energy dispersive type detector and a monochromatic CuKα radiation source. The XRD patterns were measured using a step of 0.02° with an acquisition time of 0.5 s. The average size of cobalt oxide (Co_3O_4) nanoparticles was determined by the Scherrer equation.

The samples chemical composition was determined by ICP-OES analysis. The zeolite samples for the analysis were dissolved a mixture of aqua regia and hydrofluoric acid. Quantitative elemental analyses were performed by inductively coupled plasma-optic emission spectroscopy 720-ES ICP-OES (Agilent) with axially viewing and simultaneous CCD detection. The quantitative determination of metal content in the catalysts was made based on the analysis of certificated standard solution. The ICP ExpertTM software (version 2.0.4) provides the weight percentage of components.

The textural properties of the samples were determined by N_2 physisorption using a Micromeritics ASAP 2000 apparatus. Prior to the analysis, the samples were degassed under vacuum (10 µmHg) at 350 °C for 4 h. The total pore volume (TPV) was calculated from the amount of vapor adsorbed at a relative pressure P/P0 = 0.97. The catalyst microporous volume (Vmicro) were calculated using the deBoer t-plot method. The samples mesoporous volume was calculated as the difference between the total pore volume and microporous volume.

The XPS spectra were taken using a Kratos Axis spectrometer, equipped with an aluminum monochromater for a 1486.6 eV source working at 120 W. All spectra were recorded under a vacuum of 10-8 Torr and recalibrated afterwards with the binding energy of the Al 2p at 74.6 eV.

The catalyst Brönsted and Lewis acidities were measured using Infrared spectroscopy after pyridine adsorption on a Nicolet 8700 apparatus. The samples were pretreated under vacuum (10-3 torr) at 450 °C for 2 h. After the pre-treatment, pyridine (1.2 mbar) was adsorbed on the sample at room temperature. The samples were then heated under vacuum (10-3 torr) at 150 °C and a spectrum was taken at room temperature. The intensity of the Py-L and Py-H+ peaks at ~ 1455 and 1545 cm^{-1} was measured as a function of temperature, and the resulting plots used to compare the zeolite acidity.

Fischer-Tropsch synthesis

The catalytic performance of the samples was tested in FT synthesis. The experiments were performed in a fixed-bed reactor. Prior to testing, the samples were reduced in-situ in pure H_2 gas flow at 400 °C for 4 h with a temperature ramping rate of 3 °C/min. After the reactor was cooled down to room temperature, the flow was switched to syngas (H_2/CO = 2) and the pressure was adjusted to 20 bar. Nitrogen (5% of the CO flow) was used as internal standard. The flow was adjusted to obtain GHSV of 66 L/gCo.h^{-1}). After achieving the desired pressure, the temperature was progressively increased to the reaction temperature, i.e. 250 °C, at the ramping rate of 3 °C/min. The gaseous reaction products, i.e. up to C_5, were analyzed online using gas chromatography. The liquid products were condensed under pressure and analyzed off-line using a Shimatzu 2010-Plus-AF gas chromatograph.

3.3 Results and Discussion

Catalyst characterization

The catalyst characterization data are shown in Table 3-1. The H-form of BEA zeolite impregnated with cobalt (Co/HBEA) contains 13.7 wt.% of cobalt and only trace amounts of sodium. The amount of cobalt added by impregnation to the sodium form of the zeolite was almost the same (14.3 wt.%). Note that the Co/NaBEA samples contained in addition to cobalt about 1 wt.% of sodium. Subsequent ion exchange of the Co/HBEA and Co/NaBEA samples with ammonia nitrate results in decrease in cobalt content in the catalysts. The decrease in cobalt content after the ion exchange with NH_4NO_3 is more significant in the Co/HBEA catalyst. This suggests that Co/HBEA contains a higher fraction of cobalt ion in the zeolite cation positions. Only very slight decrease in cobalt content was observed in Co/NaBEA. Most of cobalt seems to be present in this catalyst

as cobalt oxide clusters rather than isolated cobalt ions in the cation sites. The ion exchange with ammonia nitrate leads to a major decrease in the concentration of sodium in the Co/NaBEA zeolite.

The Co_3O_4 oxide phase was identified in the catalysts using IR, Raman spectroscopies and XRD. The IR spectra of the cobalt zeolite catalysts are shown in Figure S1 (SI, Supporting Information). They exhibit the peaks at 670 and 555-600 cm^{-1}, which were assigned to the ν (Co–O) vibration modes in Co_3O_4 [23]. Note that these bands overlap with the bands at 622, 525 and 468 cm^{-1} related respectively to coupled Al-O and Si-O out-of-plane vibrations, Al-O-Si and Si-O-Si bending vibrations in zeolite [24, 25]. The broad bands at 1350-1000 cm^{-1} are due to asymmetric Si–O(Si,Al) and Al–OH bending vibrations. Figure S2, SI shows the Raman spectra of the catalysts. They are also indicative of the presence of the Co_3O_4 phases. The intense band at 667 cm^{-1} is attributed to the cobalt octahedral sites (CoO_6) [23, 26, 27]. The medium intensity bands at 465 and 505 cm^{-1} correspond to the E_g and $F_{2g}^{(2)}$ sites, respectively, while the weak band located at 606 cm^{-1} has the $F_{2g}^{(1)}$ symmetry.

The cobalt oxide crystallite sizes in the calcined samples were estimated from broadening of the Co_3O_4 characteristic XRD peak at 36.8° (2θ, Figure S3, SI). All the samples showed similar cobalt oxide crystallite size, i.e. between 23-26 nm, once gain indicating that the secondary ion exchanges performed with CoH/HBEA and CoH/NaBEA had no effect on the size of larger cobalt oxide particles which are most probably localized on the external surface of zeolite. Note that XRD might not be sensitive to the presence of much smaller cobalt oxide nanoparticles in the zeolite micropores (<1 nm). Indeed, sub-nanometric clusters of cobalt oxides located inside the micropores of BEA zeolites prepared by impregnation were detected by STEM analysis in our recent publication [22].

The porous volume and surface areas of zeolites significantly decreased after the impregnation with cobalt compared to the parent samples. The reduction of the mesoporous and microporous volume observed after cobalt impregnation indicates that cobalt oxide nanoparticles are localized in both types of the pores. The microporous volume decreases by 12% and 18%, respectively, on Co/HBEA and Co/NaBEA. This phenomenon can be explained by the presence of Co_3O_4 inside the zeolite crystallites [28]. Higher loss of microporous volume observed on Co/NaBEA can be directly linked to the presence of Na^+ localized in the zeolite micropores. Slower diffusion of cobalt ions in the micropores of Na/BEA results in preferential localization of cobalt ions in the entrances of the zeolite pores. This could lead to easier blocking of the pores of NaBEA zeolite with cobalt species.

Table 3-1 Catalyst Characterization.

	N_2 Adsorption			Acidity		ICP-OES		XPS (atom ratio)		Co particle size (nm)
	S_{BET}[b] ($m^2.g^{-1}$)	V_{meso}[b] ($cm^3.g^{-1}$)	V_{micro}[b] ($cm^3.g^{-1}$)	Brönsted[a] ($\mu mol.g^{-1}$)	Lewis[a] ($\mu mol.g^{-1}$)	Co (wt.%)	Na (wt.%)	Co/Si	Si/Al	
$HBEA_{Parent}$	704	0.54	0.188	115	52	-	-	-	-	-
Co/HBEA	590	0.43	0.166	88	84	13.21	0.08	0.048	9.76	23
CoH/HBEA	570	0.37	0.168	116	137	8.89	0.08	0.036	10.37	25
Co/NaBEA	530	0.37	0.154	20	160	14.26	0.95	0.030	13.13	26
CoH/NaBEA	563	0.35	0.179	96	145	12.79	0.20	0.029	13.70	25

[a] obtained by IR spectroscopy with pyridine adsorption at 150°C
[b] values normalized per gram of zeolite

After regeneration of the catalyst acidity via ion exchange with NH_4^+ ions and calcination, CoH/NaBEA recovered most of the original microporosity, i.e. only 5% V_{micro} loss. Similarly, after NH_4^+ ion exchange, Co/HBEA recovered a much smaller portion of micropore volume. The recovery of the zeolite micropore volume after ion exchange with NH_4^+ is linked to the removal of Na^+ and Co^{2+} exchanged species from the zeolite framework. Consequently, more significant recovery of micropore volume was observed on CoH/NaBEA. This indicates a lower concentration of sub-nanometric cobalt oxide clusters inside of the zeolite micropores of NaBEA compared to the BEA zeolite H-form.

Introduction of cobalt ions to the zeolite also leads to the decrease in the mesoporous volume formed by intracrystalline spaces between zeolite crystals. Interestingly, different to microporous volume, the subsequent ion exchange does not result in the reversible recovery of this volume. This indicates that, for all samples, the decrease in mesoporous volume is principally due to the formation of cobalt oxide nanoparticles, which are non-soluble in aqueous solutions. These cobalt oxide nanoparticles, which form during catalyst calcination are located either in the mesopores or on the external surface of zeolite. This decreases interaction between the zeolite crystallites and thus mesoporous volume [15, 21, 22].

The Co 2p XPS spectra (Figure 3-1) show that Co_3O_4 is the dominant cobalt phase in oxidized catalysts. For CoH/HBEA and CoH/NaBEA, the shapes and binding energies of the Co2p line (

Figure **3-1**) at 780 eV and low-intense shake-up satellite structure with spin-orbital splitting of 15.2 eV were very similar to those of bulk Co_3O_4 [29]. Higher intensities of the satellite peaks, a shift of the XPS lines towards the higher energy region and an

increase in spin-orbital splitting observed for the XPS spectra of Co/HBEA and Co/NABEA indicate the presence of Co^{2+} ions [30, 31].

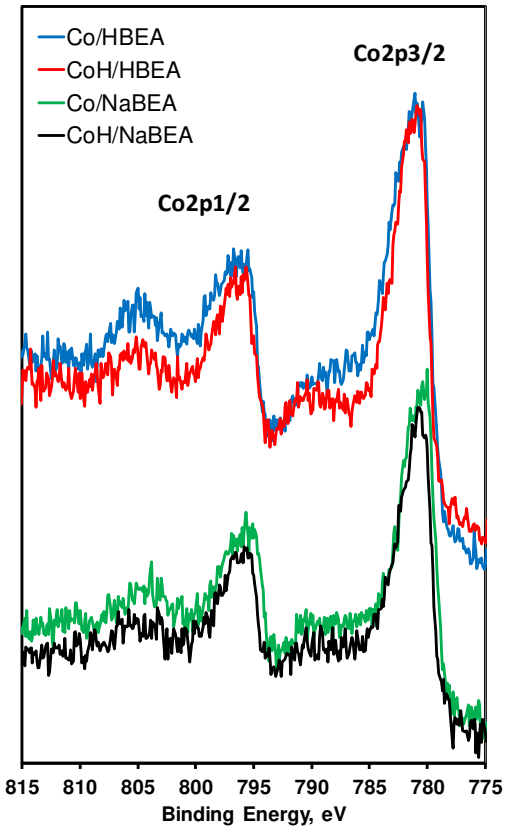

Figure 3-1 Co 2p XPS spectra of the calcined cobalt BEA zeolite catalysts.

Indeed, the Co/HBEA and Co/NaBEA samples prepared by impregnation of HBEA and NaBEA zeolite contain Co^{2+} ions in the zeolite cationic sites in addition to the Co_3O_4 crystallites. These cations are then removed by ion exchange with ammonium nitrate. The XPS Co/Si ratio (Table 3-1) almost does not change after the secondary ion exchange, while the cobalt content may decrease more significantly in particular for the Co/HBEA catalyst. This suggests that only a very small amount of cobalt is removed by ion exchange from the zeolite outer surface. Indeed, cobalt is present in the subsurface layers of the zeolite crystals mostly as Co_3O_4, which is refractory to the ion exchange.

The catalyst acidity was also impacted by the catalyst preparation method (Table 3-1). Due to the presence of cobalt oxide and cobalt ions in the exchange positions of the zeolite, the amount of Lewis acid sites was higher in the impregnated catalysts compared to the pristine zeolite [32]. The zeolite Brönsted acidity also depends on the presence of the compensation ions inside the zeolite micropores. As expected, in Co/NaBEA, the concentration of Brönsted acid sites was much lower than on other samples, due to the neutralization of the protonic sites by sodium. After NH_4^+ exchange and calcination, the concentration of Brönsted acid sites significantly increases due to the removal of cobalt ions from the cation exchange positions in Co/HBEA and to the removal of both cobalt and sodium ions from CoH/NaBEA. Still, the Brönsted acidity in CoH/NaBEA remains slightly lower than in CoH/HBEA. Note that the NH_4^+ ion exchange also results in the increase in the micropore volume because of the removal of bulky cations from the micropores (Table 3-1).

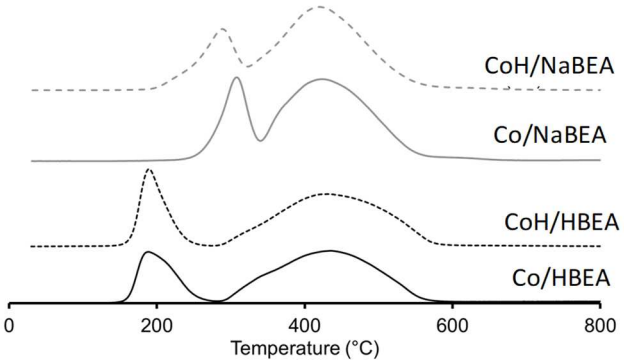

Figure 3-2 TPR catalyst reduction profiles.

The TPR profiles (Figure 3-2) clearly show that the reducibility of cobalt nanoparticles is strongly affected by the presence of sodium ions in the zeolites during impregnation. Typically, the reduction of cobalt oxide (Co_3O_4) to metallic cobalt under hydrogen atmosphere occurs in two consecutive steps: $Co_3O_4 \rightarrow CoO \rightarrow Co$ [33].

The two- step reduction is translated into two distinct peaks in the TPR profile. According to the stoichiometry, the area of the first peak should be 3 times smaller than that of the second. Figure 3-2 suggests that the reduction of Co_3O_4 to CoO is easier when the cobalt was impregnated over the proton form zeolite as the first reduction peak in Co/BEA and Co/HBEA is observed at 190 °C instead of 290-310 °C. This effect might be explained by hydrogen spillover in the presence of acid sites close to metal oxide. In comparison, when the cobalt impregnation is performed over the sodium form of BEA zeolite, the cobalt reduction only starts at 310 °C. The first reduction peak slightly shifts to 290 °C after the zeolite exchange to acid form which might be explained partial hydrogen transfer through zeolite acidity. Interestingly, this phenomenon is not observed for the second reduction peak (CoO to Co) with the hydrogen consumption peak appearing at the same temperature for all catalysts, i.e. around 420-430 °C. Previous reports [34, 35] suggest negative effect of alkali ions on cobalt reducibility. Note that no such effect was observed over Co/NaBEA zeolite (Figure 3-2) which is probably due to separate localization of cobalt and sodium species. Cobalt is preferentially localized on the zeolite outer surface, while sodium ions are located in the cation positions inside the zeolite crystallites.

Localization of cobalt species in CoH/HBEA and CoH/NaBEA zeolites after removal of cobalt ions form the zeolite cation sites is illustrated in Figure 3-3.To summarize, the CoH/HBEA and Co/HBEA catalysts prepared by impregnation contain cobalt as cobalt ions and cobalt oxide nanoparticles both in the pore and on the outer surface of the zeolite, while the Co/NaBEA and CoH/NaBEA mostly cobalt oxide particles located on the surface of the zeolite crystallites.

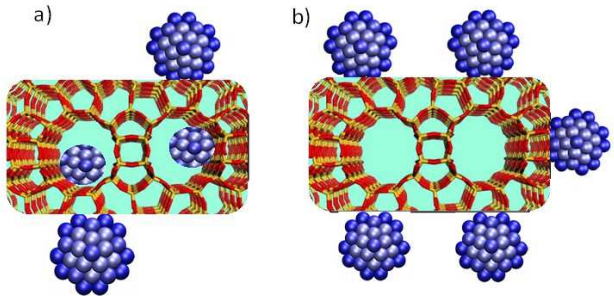

Figure 3-3 Localization of cobalt species in the CoH/HBEA (a) and CoH/NaBEA zeolite (b).

Catalytic performance in FT synthesis

All the catalysts showed significant reaction rate in FT synthesis. No changes in the catalyst activity were observed during 100 h of the reaction. Nonetheless, the catalyst activity and selectivity were significantly affected by the catalyst preparation method (Table 3-2).

After the NH_4^+ ion exchange and calcination, the activity of the CoH/HBEA catalysts increased by 132% compared to Co/HBEA and by 23% when comparing CoH/NaBEA to Co/NaBEA. Higher activity observed on the catalysts after ion exchange could be explained by the removal of cobalt and sodium ions from the zeolite micropores, higher concentration of zeolite Brönsted acid sites and easier diffusion of reaction intermediates to the acid sites inside the zeolite crystallites. The effect of NH_4^+ ion exchange and calcination on the catalytic performance is more pronounced for Co/HBEA where higher amounts of cobalt ions and cobalt active phase are located inside of the micropores. Ion exchange results in the removal of cobalt ions from the cation sites and reappearance of Brönsted acid sires. This result also indicates that the FT reaction rates are enhanced when cobalt nanoparticles and Brönsted acid sites are located in the proximity [13].

Once again, the catalytic data confirm distinct localization of cobalt and sodium species in Co/NaBEA samples. Alkali metal ions were reported [34, 35] to be poisons for conventional supported cobalt FT catalysts. Preferential localization of cobalt on the outer surface of NaBEA zeolite and sodium ions inside the zeolite pores leads to very weak interaction between cobalt and sodium in Co/NaBEA, very small cobalt poisoning and thus, a high catalytic activity of this sample. Similar phenomenon was observed early for Y-zeolites [36]. In the Y-zeolite, sodium had very small influence of the intrinsic activity of cobalt species because of sodium preferential localization in small cages on Y-zeolite, while cobalt was mainly present in the mesopores.

The product selectivities over different cobalt-zeolite catalysts are shown in Table 3-2 and Figure 3-4. Significant differences were observed as functions of catalyst preparation procedures. The selectivity towards methane was higher, when cobalt was impregnated on HBEA when compared to NaBEA, i.e. 22.2% compared to 17.5%. HBEA zeolite contained cobalt nanoclusters localized in the zeolite pores where their sizes are limited by the the pore diameters. Previously it was shown [37] that cobalt particle size smaller than 6 nm might lead to higher methane selectivity. In addition, localization of cobalt nanoparticles into the zeolite micropores in Co/HBEA introduces diffusion limitations for carbon monoxide, which results in higher H_2/CO ratio in the micropores and thus, leads to higher methane selectivity [38]. Higher methane selectivity was recently observed [22] over Co/zeolite catalysts containing cobalt nanoparticles only inside the zeolite crystals. The catalysts were prepared by selective extraction of cobalt from the zeolite outer surface using heteropolyacids. The Co/NaBEA contains mostly cobalt species on the zeolite external surface and was therefore less selective to methane.

After the NH_4^+ ion exchange, methane selectivity increases to 29% on Co/HBEA, whereas on CoH/NaBEA a slight decrease to 16.1% is observed. Similar trends were

observed for the C_2-C_4 hydrocarbon selectivity. Co/HBEA was less selective to the C_5^+ hydrocarbons followed by CoH/HBEA, Co/NaBEA and CoH/NaBEA, respectively with 48.7, 63.9, 66 and 71.9%. The C_2-C_4 olefins to paraffins ratio (Table 3-2) show slight differences between the samples [39, 40].

Table 3-2 Catalytic performance in FT at iso-coversion.*

	FT activity ($mol_{CO}.g_{Co}^{-1}.h$)	XCO_2 %	S_{CO2}	S_{CH4}	C_2-C_4		S_{C5+}	Isomer fraction in C_{9+} wax, %	Alpha
					S_{Total}	Olefin / Paraffin			
Co/HBEA	0.65	72	0.6	22.2	13.3	0.30	63.9	67	0.63
CoH/HBEA	1.51	74	1.6	29.0	20.7	0.22	48.7	63	0.48
Co/NaBEA	0.79	63	1.5	17.5	15.0	0.35	66.0	47	0.76
CoH/NaBEA	0.97	68	0.5	16.1	11.4	0.31	71.9	65	0.60

*Conversion is around 70% obtained though different GHSV (GHSV = 66 $Lg.Co^{-1}.h^{-1}$)

The wax composition for each catalyst is presented in Figure 3-5. The presence of n-paraffin and isomerized products was observed for all samples. No significant differences in the total isomer fraction among the catalysts were observed, with the exception of Co/NaBEA where a smaller amount of Brönsted acid sites (Table 3-1) led to lower selectivity to branched hydrocarbons. The catalyst preparation method also affects the hydrocarbon chain length in the wax products. On Co/NaBEA, hydrocarbons up to 25 carbons were observed, whereas for CoH/HBEA the carbon chain growth was limited to 20 carbons. The chain probability growth factor (α) determined by applying the ASF distribution model (Table 3-2, Figure 3-5) showed that the samples capacity to produce long carbon chain products decreases in the following order: Co/NaBEA>Co/HBEA>CoH/NaBEA>CoH/HBEA. The distribution of liquid products seems to be affected by both localization of metal phase and concentrations of Brönsted acid sites.

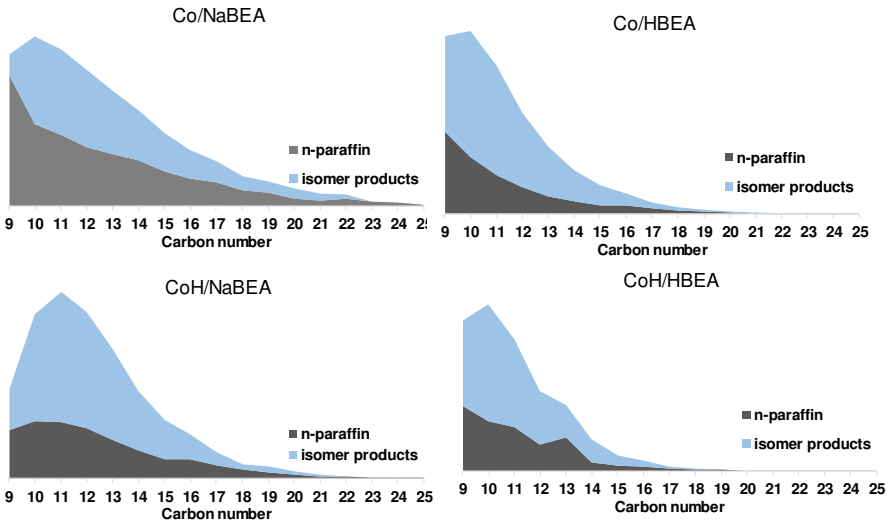

Figure 3-4 Wax products (C_{9+}) distribution.

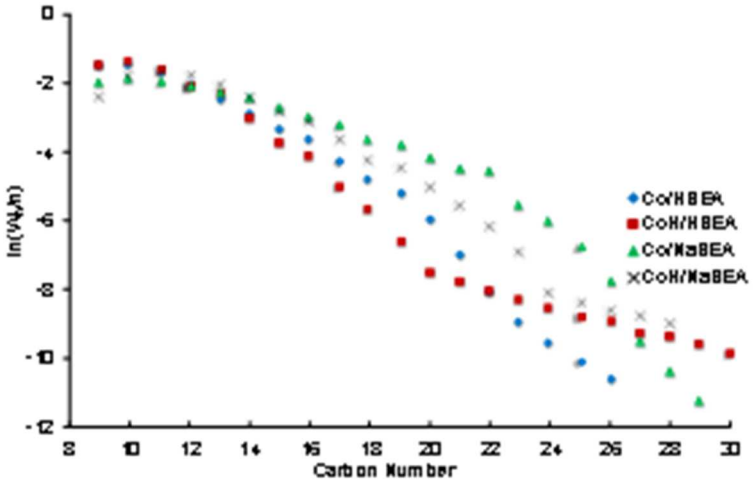

Figure 3-5 ASF distribution plot for the wax products obtained from the FT synthesis reaction.

Co/NaBEA has lower concentration of Brönsted acid sites, which are neutralized by Na^+, and the metal was mostly located on the external surface of the zeolite. Consequently, the hydrocarbons formed on the metal sites on the zeolite outer surface were less likely to undergo isomerization and cracking. Higher selectivity to long chain hydrocarbons was observed.

On CoH/NaBEA, the metal location is similar to Co/NaBEA. Most of cobalt is localized on the zeolite external surface. The zeolite Brönsted acidity was obtained after exchange of Na^+ with NH_4^+ ions and subsequent calcination. Consequently, the

CoH/NaBEA sample showed improved isomerization and cracking rates compared to Co/NaBEA. On Co/HBEA, the metal species are located both on the external surface of zeolite and inside the micropores. Some of Brönsted acid sites in Co/HBEA are neutralized by cobalt cations. The smaller size of the metal sub-nanometric cobalt clusters located in the confined space of the zeolite micropores and, the proximity to the acid sites contribute to shorter carbon chain length of the formed products [6, 37, 41, 42]. On the one hand, localization of cobalt metal particles inside the zeolite micropores could lead to the diffusion limitations in particular for carbon monoxide and would increase locally the H_2/CO ratio. Higher H_2/CO ratio would favor higher selectivity to methane and light hydrocarbons. On the other hand, the short diffusion pathway of the paraffins produced over cobalt clusters located inside the zeolite framework to the acid sites improves isomerization and cracking reactions and leads to the formation of smaller carbon chain products. It is important to mention that the higher methane selectivity observed on Co/HBEA and CoH/HBEA is directly linked to the FT synthesis, since methane formation through β-scission does not usually occur [43] and the protolytic cracking mechanism is unlikely to occur under the reaction conditions [44].

The preferential deposition of cobalt on the BEA zeolite external surface was proven to be an effective way to achieve simultaneously high FT reaction rate and lower methane selectivity. Removal of cobalt ions from the zeolite micropores by ion exchange results in the enhancement of the selectivity to the isomerized long chain hydrocarbons over Co/NaBEA zeolite. This catalyst has both high C_5^+ selectivity and higher fraction of isomerized hydrocarbons in the wax products. It is important to mention that Na^+ ions are not bulky enough to completely stop diffusion of Co^{2+} ions inside the micropores during impregnation. Consequently, the use of bulkier ions, e.g. K^+, or direct impregnation after zeolite synthesis before template removal, might be possible options to reduce the cobalt

ions diffusion inside the framework. The BEA zeolite has relatively large pores. The situation could be different for ZSM-5 with narrow zeolite pores (d= 5.5 Å) and in particular in the samples with larger zeolite crystallites. The diffusion limitation in ZSM-5 zeolites can become much more severe. The preferential localization of cobalt species on the outer surface of ZSM-5 might not be optimal for the enhanced catalytic performance.

3.4 Conclusion

The zeolite impregnation procedure and ion exchange sequence have a very strong impact on the structure and localization of cobalt species in BEA zeolite and catalytic performance in FT synthesis. Occupation of the zeolite cation exchange sites by sodium ions favored deposition of cobalt during impregnation with cobalt nitrate on the zeolite external surface. Cobalt deposition on the H-from of BEA zeolite via impregnation results in cobalt localization both on the zeolite outer surface and in the zeolite micropores.

Simultaneous deposition of cobalt on the BEA zeolite external surface and in the micropores leads to cracking and higher methane selectivities. The sample with the metal particles on the external surface and high concentration of Brönsted acid sites in the zeolite micropores, i.e. CoH/NaBEA exhibited lower methane, higher selectivity to long chain hydrocarbons and significant yield of isomerized hydrocarbons.

References

[1] A.Y. Khodakov, W. Chu, P. Fongarland, *Chem. Rev.* **2007**, 107, 1692–1744.

[2] B.H. Davis, M.L. Occelli, *Stud. Surf. Sci. Catal.* **2006**, 163, 1–420.

[3] Q. Zhang, K. Cheng, J. Kang, W. Deng, Y. Wang, *ChemSusChem* **2014**, 7, 1251–1264.

[4] H. Schulz, *Catal. Today* **2014**, 228, 113–122.

[5] G. Henrici-Olivé, S. Olivé, *Angew. Chemie Int. Ed* **1976**, 15, 136–141.

[6] V. Subramanian, K. Cheng, C. Lancelot, S. Heyte, S. Paul, S. Moldovan, O. Ersen, M. Marinova, V. V. Ordomsky, and A. Y. Khodakov, *ACS Catal.* **2016**, 6, 1785−1792.

[7] Y. Chen, N. Batalha, M. Marinova, M. Impéror-Clerc, C. Ma, O. Ersen, W. Baaziz, J.A.Stewart, D. Curulla-Ferré, A. Y.Khodakov, Vitaly V.Ordomsky, *J. Catal.* **2018**, 365, 429-439.

[8] V. V. Ordomsky, A. Y. Khodakov, B. Legras and C. Lancelot, *Catal. Sci. Technol.* **2014**, 4, 2896-2899.

[9] Bouchy, C., Hastoy, G., Guillon, E., Martens, J. A., *Oil Gas Sci. Technol. - Rev. IFP* **2009**, 64, 91–112.

[10] C. Flores, N. Batalha, V. V. Ordomsky, V. L. Zholobenko, W. Baaziz, N. R. Marcilio, A. Y. Khodakov, *ChemCatChem* **2018**, 10, 2291-2299.

[11] F. Pinto, R.N. André, C. Carolino, M. Miranda, *Fuel Process. Technol.* **2014**, 126, 19–29.

[12] S. Bessell, *Appl. Catal. A* **1995**, 126, 235–244.

[13] V. Subramanian, V.L. Zholobenko, K. Cheng, C. Lancelot, S. Heyte, J. Thuriot, S. Paul, V. V. Ordomsky, A.Y. Khodakov, *ChemCatChem* **2016**, 8, 380–389

[14] D.J. Koh, J.S. Chung, Y.G. Kim, *Ind. Eng. Chem. Res.* **1995**, 34, 1969–1975.

[15] K. Jothimurugesan, S.K. Gangwal, *Ind. Eng. Chem. Res.* **1998**, 37, 1181–1188.

[16] S. Bessell, *Appl. Catal. A.* **1993**, 96, 253–268.

[17] K. Cheng, L. Zhang, J. Kang, X. Peng, Q. Zhang, Y. Wang, *Chem. - A Eur. J.* **2015**, 21, 928–1937.

[18] S. Sartipi, M. Alberts, M.J. Meijerink, T.C. Keller, J. Pérez-Ramírez, J. Gascon, F. Kapteijn, *ChemSusChem* **2013**, 6, 1646–1650.

[19] H. Valdés, S. Alejandro, C.A. Zaror, *J. Hazard. Mater.* **2012**, 227–228, 34–40.

[20] V.R. Choudhary, D.B. Akolekar, *J. Mol. Catal.* **1991**, 66, 215–222.

[21] M.A. Keane, *Microporous Mater.* **1994**, 3, 93–108.

[22] A. Carvalho, M. Marinova, N. Batalha, N.R. Marcilio, A.Y. Khodakov, V. V. Ordomsky, *Catal. Sci. Technol.***2017**, 7, 5019-5027.

[23] J. Jiang, L. Li, *Materials Letters* **2007**, 61, 4894–4896.

[24] V.C. Farmer, The layer silicates. In: Farmer, V.C. (Ed.), The Infrared Spectra of Minerals. Mineralogical Society, London, 1974, pp. 331 – 363.

[25] J. Madejov, M. Janek , P. Komadel, H.-J. Herbert , H.C. Moog, *Applied Clay Science* **2002**, 20, 255 – 271.

[26] C.V. Ramana, M. Massot, C.M. Julien, *Surf. Interface Anal.* **2005**, 37, 412-416.

[27] Z.V. Marinkovic Stanojevic, N. Romcevic, B. Stojanovic, *J. Eur. Ceram. Soc.* **2007**, 27, 903-907.

[28] V. Subramanian, V.L. Zholobenko, K. Cheng, C. Lancelot, S. Heyte, J. Thuriot, S. Paul, V. V Ordomsky, A.Y. Khodakov, *ChemCatChem* **2016**, 8, 380–389.

[29] J.P. Bonnelle, J. Grimblot, A. D'huysser, A., *J. Electron Spectr.* **1975**, 7, 151-162

[30] D.G. Castner, P.R. Watson and I.Y. Chan, *J.Phys.Chem.* **1989**, 93, 3188-3194.

[31] S.W. Ho, M. Horialla, D.M. Hercules, *J.Phys.Chem.* **1990**, 94, 6396-6399.

[32] G.A.. Mekhemer, H.M.. Abd-Allah, S.A.. Mansour, *Colloids Surfaces A Physicochem. Eng. Asp.* **1999**, 160, 251–259.

[33] E. Van Steen, G.S. Sewell, R.A. Makhothe, C. Micklethwaite, H. Manstein, M. De Lange, C.T.O. Connor, *J. Catal.* **1996**, 162, 220–229.

[34] A. H. Lillebø,E.Patanou, J. Yang,E.A.Blekkan, A.Holmen, Catal. Today 2013, 215, 60–66

[35] Ø.Borg, N.Hammer, B.C.Enger, R. Myrstad, O. A. Lindvag,S.Eri, T. H.Skagseth, E. Rytter, *J. Catal.* **2011**, 279,163 –173.

[36] X. Peng, K. Cheng, J. Kang, B. Gu, X. Yu, Q. Zhang, Y. Wang, *Angew. Chem. – Int. Ed*. **2015**, 54, 4553-4556.

[37] G. L. Bezemer, J. H. Bitter†, H. P. C. E. Kuipers, H. Oosterbeek, J. E. Holewijn, X. Xu, F. Kapteijn, A. J. van Dillen, and K. P. de Jong, *J. Am. Chem. Soc.* **2016**, 128, 3956-3964.

[38] E. Iglesia, S.C. Reyes, R.J. Madon and S.L. Soled, *Adv. Catal.* **1993**, 39, 221-.

[39] E. Janiszewska, M. Kot, M. Zieliński, *Micro Mesopor Mater.* **2018**, 255, 94–102.

[40] J. Wang, Q. Li, J. Yao, *Appl. Catal. A.* **1999**, 184, 181–188.

[41] Ø. Borg, P.D.C. Dietzel, A.I. Spjelkavik, E.Z. Tveten, J.C. Walmsley, S. Diplas, S. Eri, A. Holmen, E. Rytter, *J. Catal*. **2008**, 259, 161–164.

[42] J.P. den Breejen, P.B. Radstake, G.L. Bezemer, J.H. Bitter, V. Frøseth, A. Holmen, K.P. de Jong, *J. Am. Chem. Soc*. **2009**, 131, 7197–7203.

[43] J. Weitkamp, S. Ernst, *Catal. Today* **1994**, 19, 107–149.

[44] A. Corma, P.J. Miguel, A. V Orchillés, *J. Catal.* **1997**, 172, 355-369.

Supporting Information

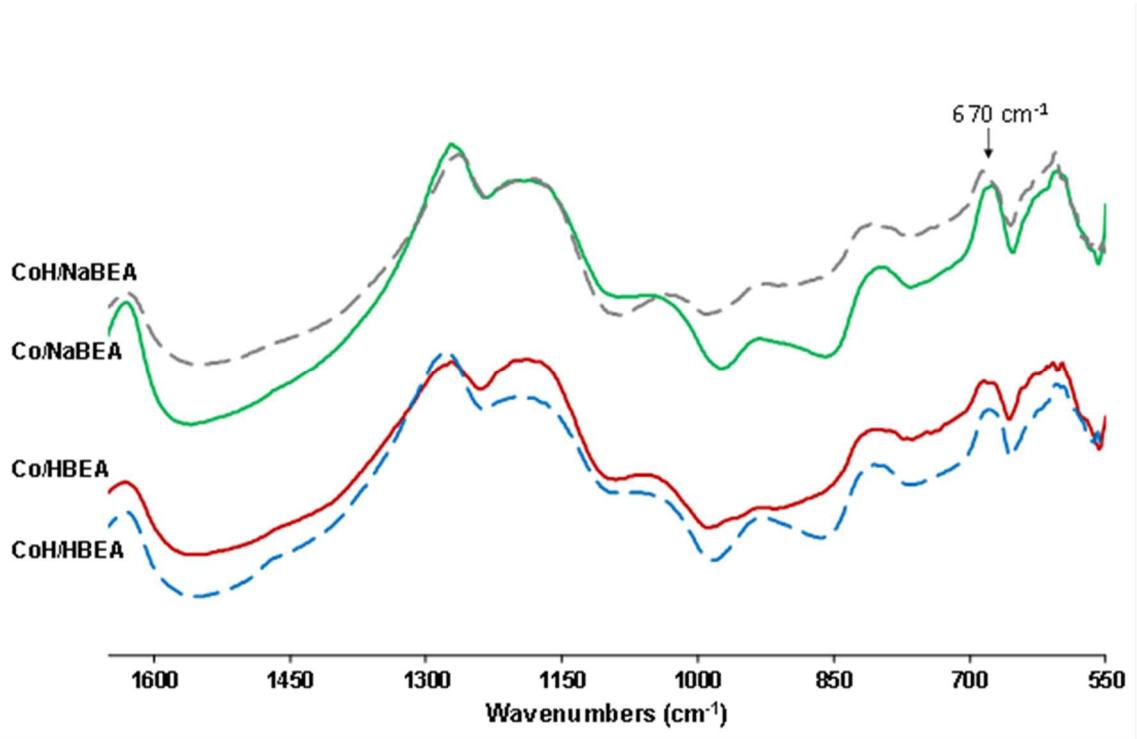

Figure S1. IR spectra of cobalt zeolite catalysts.

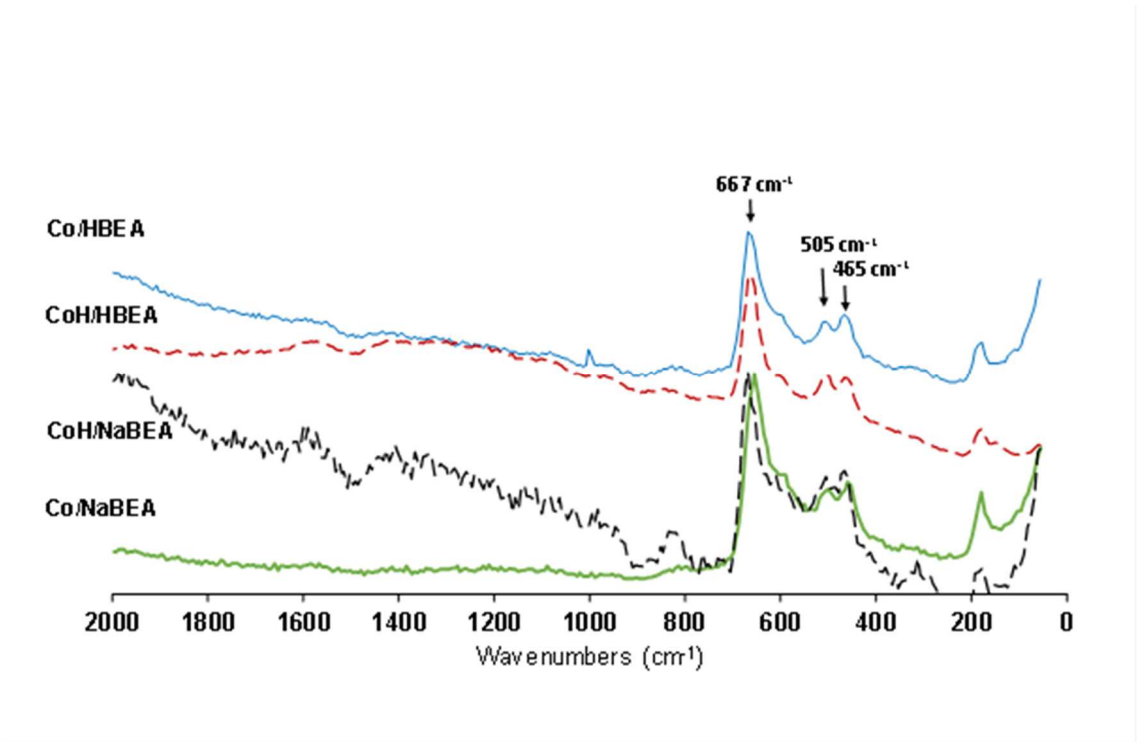

Figure S2. Raman spectra of cobalt zeolite catalysts.

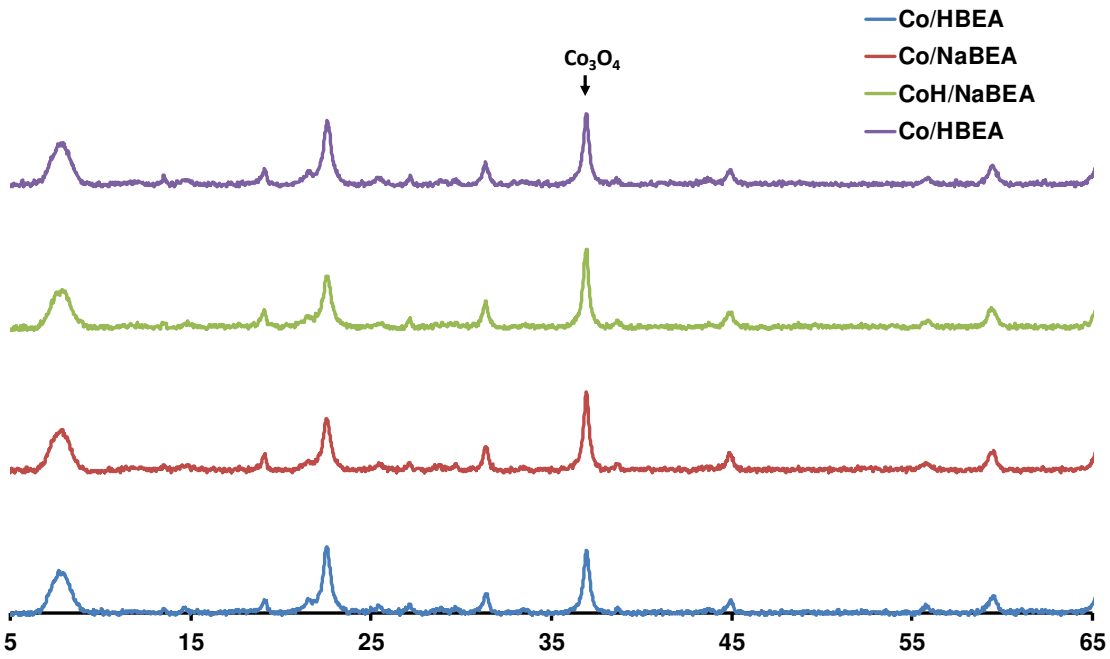

Figure S3. XRD patterns of cobalt zeolite catalysts.

Chapter 4: Direct production of iso-paraffins from syngas over hierarchical cobalt-ZSM-5 nanocomposites synthesized using carbon nanotubes as sacrificial templates

Paper published in ChemCatChem, February 2018, IF 4.67, Qualis A1

Abstract: This chapter focuses on the effect of synthesis conditions on the structure of cobalt-ZSM-5 zeolites, localization, dispersion and reducibility of cobalt species and their catalytic performance in Fischer-Tropsch synthesis. The zeolite catalysts were prepared using carbon nanotubes as sacrificial templates. Addition of pristine carbon nanotubes resulted only in a slight increase in the zeolite mesoporosity, while the presence of carbon nanotubes impregnated with cobalt drastically modified the zeolite morphology and texture. The zeolite mesoporous volume increased by 3-4 times. The catalysts prepared using cobalt impregnated carbon nanotubes as templates showed 5-10 times higher Fischer-Tropsch reaction rates normalized by reducible cobalt compared to the catalysts prepared by conventional impregnation. Higher selectivity to isomerized branched hydrocarbons on these zeolites was attributed to the enhanced diffusion favoring removal of isomerized products and avoiding their cracking.

4.1 Introduction

The depletion of fossil resources and increasing environmental concerns have led to the necessity for the development of new catalytic processes from alternative renewable resources. Natural gas and biomass can be transformed into syngas (H_2/CO) and subsequently by Fischer-Tropsch (FT) synthesis over cobalt-based catalysts into middle distillates and waxes [1-3]. FT synthesis is a "nontrivial surface polymerization reaction [4], with reaction selectivity typically described by the broad Anderson-Schulz-

Flory distribution (ASF) [1, 5]. Consequently, the major challenge of FT reaction is to tune the reaction selectivity to specific hydrocarbon fractions.

Several methods have been proposed for selectivity control in FT synthesis. First, catalytic cracking/isomerization of FT hydrocarbons can upgrade the reaction products to a specific fuel. Combination of FT synthesis with hydrocracking and isomerization of long chain hydrocarbons restricts the hydrocarbon distribution to a more convenient range [6]. The isomerization and cracking of FT hydrocarbons would lead to iso-paraffins or diesel fuels constituted by the C_{10}-C_{20} hydrocarbons. This multistage process, however, significantly reduces the efficiency of synthetic fuel production.

An alternative to that multi-stage process would be to utilize bifunctional catalysts containing an active FT component, e.g. Co or Ru, and an acid catalyst active for cracking and isomerization. The proximity between metal and acid sites is an important parameter of the bifunctional catalysts often governing reaction rate and selectivities. Recently two additional methods for hydrocarbon selectivity control were proposed, which involve making use of nanoreactors [7] and microemulsions [8]. In these methods the carbon chain length is limited by steric and diffusion limitations.

Zeolites have been often suggested as promising catalysts for hydrocarbon cracking and isomerization under the conditions similar to FT synthesis [3, 9]. An FT catalyst can be combined with a zeolite through several different methods: in a dual bed catalytic reactor with FT catalyst in the first layer followed by zeolite [10, 11]; in hybrid catalysts prepared by mixing of FT catalyst and zeolite [12-14]; in the catalysts prepared by zeolite impregnation with metal salts [13, 15-18]; and by composite zeolite/metal catalysts, for example, core-shell materials [19, 20].

A significant number of research publications have been dedicated to direct synthesis of gasoline and middle distillates over dual bed or hybrid catalysts obtained

through combination of supported Co catalysts and zeolites [10-16, 21-23]. Different types of zeolite frameworks such as ZSM-5, MCM-22, IM-5, ITQ-2, BEA, MOR, and FAU with and without addition of noble-metal promoters have been tested and combined with FT synthesis catalysts. Still, slow diffusion of long-chain paraffins through zeolite pores, in particular on medium-pore zeolites, leads to a preferential participation of the acid sites on the zeolite external surface and lower isomerization efficiency [22].

Impregnation is another method for the preparation of bi-functional Co-zeolite catalysts for direct production of fuels from syngas [13, 15-18, 24-26]. Still, this method presents a major drawback that is the neutralization of the zeolite acid sites by cobalt ions. Cobalt ions, introduced during impregnation, can occupy cation positions in the zeolite framework decreasing the number of acid sites available for hydrocarbon isomerization and cracking, while larger cobalt oxide particles can be detected on the outer surface of zeolite. Additionally, isolated Co cations in the zeolite framework are very difficult to reduce to metallic cobalt. Cobalt species on the zeolite outer surface have low dispersion and generate insufficient number of active sites for FT reaction. This decreases the amount of active phase for FT synthesis.

The improvement of zeolite diffusion properties through creating a hierarchical porous network has been the subject of extensive research [27-30]. The application of this type of materials was proven to be beneficial for the activity and selectivity of several catalytic reactions including long-chain paraffin isomerization and cracking combined with FT synthesis [26, 29-33]. Several synthesis methodologies, classified as top-down and bottom-up have be applied to the synthesis of hierarchical zeolites. A mesoporous network can be created directly by partially destroying the zeolite crystal through desilication [27, 34] or dealumination [35, 36]. Alternatively, hierarchical zeolites can be produced directly during the zeolite synthesis through the use of external templates that

are sacrificed after zeolite synthesis, e.g. carbon structures [28, 37] resins [38] or polymers [39]. It is important to emphasize that cobalt is usually added to the zeolites in the second step after hierarchization of the zeolite.

The goal of this work is to obtain in a one-pot synthesis composite hierarchical zeolites with cobalt metal particles uniformly distributed in the zeolite mesoporous structure. This has been achieved by using cobalt impregnated carbon nanotubes (Co/CNT) as sacrificial templates during the synthesis of ZSM-5 zeolite. Two different carbon nanotubes (CNT) with outer diameters of 10-20 nm and 20-40 nm were used to induce mesoporosity in ZSM-5. The catalysts were characterized by low-temperature N_2 adsorption, transmission electron microscopy (TEM), temperature-programmed reduction (TPR) and FTIR spectroscopy with adsorbed pyridine (Py). The hierarchical cobalt-zeolite samples were tested in FT synthesis and their catalytic performance in particular relative to synthesis of iso-paraffins was compared with the Co/ZSM-5 catalysts prepared by conventional impregnation.

4.2 Experimental Section

Impregnation of carbon nanotubes with cobalt

Prior to the impregnation, the multiwalled carbon nanotubes (CNTs) were treated with nitric acid to remove all metal contamination. Two different CNT samples (Iolitec nanomaterial, 95%) with different diameters, that is, 10-20 nm and 20-40 nm, were used. Typically, CNTs (3 g) were pretreated in concentrated HNO_3 (68%, 210 mL) for 14 h under reflux conditions. After, the samples were filtered, washed with distilled water until pH 7, and dried at 100 °C overnight.

Cobalt and platinum were introduced to CNTs by wet impregnation method using respectively $Co(NO_3)_2*6H_2O$ (Sigma-Aldrich, 98%) and $Pt(NH_3)_4(NO_3)_2$ (Sigma-

Aldrich) as precursors. Typically, $Co(NO_3)_2$ and $Pt(NH_3)_4(NO_3)_2$ solution (50 mL) was used per gram of CNTs and the precursor amount was estimated to obtain a final composition of 20 wt.% Co and 0.1 wt.% Pt. The mixture was submitted to ultrasonic treatment for 30 min and dried at 80 °C. The samples were calcined at 400 °C for 4 h under a nitrogen atmosphere.

After the calcination, the samples were treated with H_2O_2 to restore the hydrophilic properties of the CNTs. Typically, 30 mL of 1:1 H_2O_2 (Sigma-Aldrich, 35%) and distilled water were added to impregnated CNTs (2.56 g), which was sonicated for 30 min and dried at 80 °C.

Synthesis of hierarchical cobalt - ZSM-5

The ZSM-5 zeolite was synthesized by using the following initial composition of the gel: $2.7NaCl:1Al_2O_3:12.5TPAOH:55.8SiO_2:7500H_2O$. Sodium chloride (0.380 g, Janssen Chimica, P.A.), tetrapropylammonium hydroxide (3.0 g, Sigma-Aldrich, 1M in H_2O), sodium aluminate (0.040 g, Sigma-Aldrich) and distilled water were mixed until a clear solution was obtained. Then, Co/CNT (0.3 g) and tetraethyl orthosilicate (TEOS, 2.8 g, Sigma-Aldrich, 99%) were added to the solution. After, the synthesis gel was aged for 1 h at room temperature under stirring. The synthesis gel was set inside a Teflon-lined autoclave (40 mL) and the zeolite crystallization performed under static condition at 170 °C for 24 h. After cooling down, the solid was recovered by filtration and washed until neutral pH. The final solid was calcined at 600 °C for 4 h under air. Thermogravimetric analysis showed complete decomposition and oxidation of cobalt-containing carbon nanotubes at temperatures below 400 °C. This suggests that cobalt zeolite composite catalysts calcined at 600 °C in air did not contain any residual carbon species.

For comparison, zeolite syntheses without addition of CNTs or in the presence of CNTs, which did not contain cobalt ions, were performed. The prepared zeolites were impregnated with cobalt and platinum precursors in the final catalysts.

To obtain the zeolite acid form, two successive exchanges using 2 M NH_4NO_3 aqueous solution at 80 °C for 1 h (1 g of zeolite per 50 mL of solution) were performed. The ammonium form was converted into the protonic form by calcination at 450 °C for 4 h under air.

The synthesized samples were denoted as: $CoCNT_{(x)}$/ZSM-5 for the samples synthesized with cobalt and platinum co-impregnated CNTs (x represents the CNT diameter used in the synthesis, that is, 10-20 or 20-40 nm); $Co_{(x)}$/ ZSM-5 for the samples synthesized with CNTs and subsequently impregnated with Co and Pt (x represents the CNT diameter used in the synthesis, that is, 10-20 nm or 20-40 nm). Co/ZSM-5 stands for the zeolite synthetized without addition of CNTs and impregnated with the Co and Pt precursors.

Catalyst characterization

The samples were characterized by X-ray diffraction (XRD) by using a D8 Advance diffractometer equipped with an energy dispersive type detector and a monochromatic CuK_α radiation source. The samples were analyzed using a step of 0.02° with an acquisition time of 0.5 s. The average size of cobalt oxide (Co_3O_4) crystallites was determined by the Scherrer equation.

The sample chemical composition was determined by X-ray fluorescence (XRF) on a spectrometer M4 TORNADO (Bruker). This instrument is equipped with 2 anodes: rhodium X-ray tube 50 kV/600 mA (30 W) and a tungsten X-Ray tube 50 kV/700 mA (35 W). For sample characterization, the rhodium X-rays with a poly-capillary lens

enabling excitation of an area of 200 μm were used. The detector used was a Silicon-Drift-Detector Si(Li) with <145 eV resolution at 100000 cps (MnK_α) and cooled with a Peltier cooling (253°K). The measurement was done under vacuum (20 mbar). Quantitative analysis was performed using fundamental parameter (FP; standardless).

The textural properties of the samples were determined by N_2 physisorption on a Micromeritics ASAP 2000 apparatus. Prior to analysis, the samples were degassed under vacuum (10 μmHg) at 350 °C for 4 h. The total pore volume (TPV) was calculated from the amount of vapor adsorbed at a relative pressure $P/P_0 = 0.97$. The samples surface area was estimated by the BET method, while the micropore volume and external surface were calculated using the deBoer t-plot method.

The catalyst reducibility was studied using temperature-programmed reduction (TPR) system with an Autochem II (Micrometrics) apparatus. The samples were reduced under a flow of 5% H_2 in argon (50 mL min^{-1}) and heated up to 800 °C at a rate of 5 °C/min.

Comparative characterization of the acidic OH groups (Brönsted acid sites) and Lewis acid sites in solid acids, e.g. zeolites, was carried out using transmittance FTIR measurements in the 6000-900 cm^{-1} spectral range utilizing pyridine adsorption for monitoring the strength and relative quantities of both Lewis and Brönsted acid sites. FTIR transmittance measurements were performed at ~30 °C using self-supported disks of studied materials activated at 450 °C for 5 h in vacuum (with the temperature ramp of 1 °C/min). FTIR spectra have been collected using a Thermo iS10 spectrometer at a 4 cm^{-1} resolution (0.96 cm^{-1} data spacing). The spectra were analyzed and presented (including integration, differentiation and determination of peak positions) using specialized Thermo software, Omnic. Acidic properties of the samples were evaluated using temperature

programmed desorption of pyridine (Py) monitored spectroscopically. An excess of Py was admitted into the transmittance cell at 150 °C, in a stepwise manner until no changes were observed in the spectra. The saturated sample was then evacuated for 10 min at 150 °C to remove physically adsorbed Py and the FTIR spectrum collected. In the transmittance TPD experiments, Py was removed under vacuum in a stepwise fashion at 150-450 °C, and the FTIR spectra were obtained at each temperature step, every 50 °C. The intensity of the Py-L and Py-H^+ peaks at ~ 1455 and 1545 cm^{-1} was measured as a function of temperature, and the resulting plots used to compare the effective acidity of the samples.

The TEM observations of the samples were obtained by using a Tecnai instrument equipped with a LaB6 crystal operated at 200 kV. Before the analysis, the samples were dispersed by ultrasound in ethanol for 5 min, and a drop of the suspension was deposited onto a carbon membrane on a 300 mesh copper grid. The STEM-HAADF tomographic analysis was carried out on a Jeol 2100F (field emission gun) microscope operating at 200 kV by using a spot size of 1.1 Å with a current density of 0.5 pA $Å^{-1}$.

Catalytic tests

The catalytic performance of the samples was tested in FT synthesis. The experiments were performed in a milli-fixed bed reactor. All the details of the catalytic test relevant to mass and heat transfers are given in our earlier publication [53]. No significant (>0.5 bar) pressure drop and temperature gradient are observed under the reaction conditions. Prior to testing, the samples were reduced in situ in pure H_2 gas flow (3 mL min^{-1}) at 400 °C for 4 h with a heating rate of 3 °C/min. Then, the reactor was cooled down to room temperature, the flow switched to syngas (H_2/CO = 2) and the

pressure adjusted to 20 bar. Nitrogen (5% of the CO flow) was used as internal standard. The flow was adjusted to obtain a GHSV of 20-70 $L/g_{Co}.h$. After achieving the desired pressure, the temperature was progressively increased to the reaction temperature, i.e. 250 °C, at a rate of 3 °C/min. The reaction was conducted at 250 °C in order to create in addition to FT synthesis favorable conditions for secondary reactions such as olefin cracking and isomerization. The gas hourly space velocity (GHSV) was expressed in $cm^3 g_{cat}^{-1} h^{-1}$. The units correspond to the volume of syngas, which passed through 1 g of catalyst per hour. The gaseous reaction products, i.e. up to the C_5 hydrocarbons were analyzed online using gas-chromatography (GC×FID/TCD, Varian, CP-3800). The liquid products were condensed under pressure and analyzed ex situ using a Shimadzu 2010-Plus-AF gas-chromatograph.

4.3 Results and Discussion

Catalyst structure

The XRD patterns of the synthesized samples are displayed in Figure 4-1. All samples present characteristic peaks of MFI zeolite. The presence of CNTs during hydrothermal treatment does not affect to any noticeable degree the intensity of the XRD peaks. The introduction of cobalt by impregnation or with CNTs during the zeolite synthesis led to an overall reduction of the intensity of the zeolite characteristic peaks. This was attributed to the effect of "dilution" and lower concentration of MFI phase in these samples. The Co_3O_4 phase was detected using a characteristic peak at 2 θ equal to 36.8°in all samples containing cobalt. The particle size of Co_3O_4 calculated using the Scherrer equation (Table 4-1) was in all cases between 27 and 44 nm, indicating that a large fraction of cobalt is located either in the mesopores or on the zeolite external surface. Interestingly, smaller diameter CNTs (10-20 nm) during zeolite crystallization led to the

formation of smaller Co_3O_4 particles, i.e. around 30 nm, when compared with the synthesis without CNTs or using larger diameter CNTs (20-40 nm).

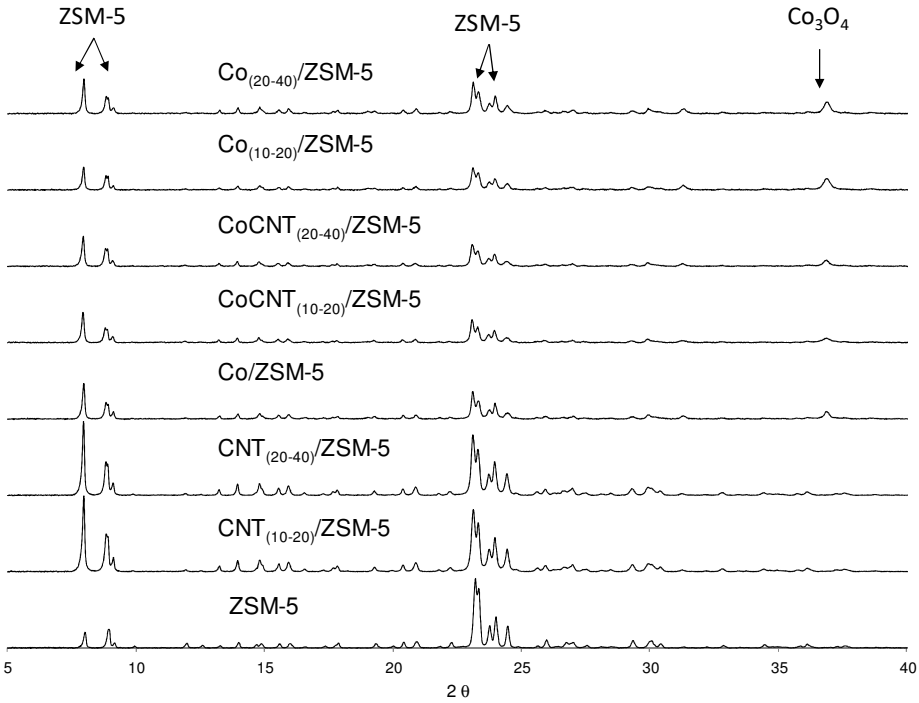

Figure 4-1 XRD patterns of cobalt ZSM-5 nanocomposites.

Table 4-1 Catalyst textural characterization.

Sample	N_2 adsorption				Co content (wt %)	Co_3O_4 Particle size* (nm)
	S_{BET} (m^2g^{-1})	V_{tot} (cm^3g^{-1})	V_{mic} (cm^3g^{-1})	V_{meso} (m2g-1)		
ZSM-5	425	0.19	0.13	0.06	-	-
$CNT_{(10-20)}$/ZSM-5	434	0.21	0.12	0.09	-	-
$CNT_{(20-40)}$/ZSM-5	418	0.21	0.10	0.11	-	-
Co/ZSM-5	372	0.17	0.11	0.06	15.6	44
$Co_{(10-20)}$/ZSM-5	360	0.18	0.10	0.08	13.2	27
$Co_{(20-40)}$/ZSM-5	276	0.13	0.08	0.05	12.7	40
$CoCNT_{(10-20)}$/ZSM-5	435	0.32	0.09	0.23	7.8	29
$CoCNT_{(20-40)}$/ZSM-5	395	0.25	0.09	0.16	9.4	42

The catalyst textural properties are listed in Table 4-1. The nitrogen adsorption desorption isotherms are displayed in Figure S4 (Supporting information, SI). The

introduction of CNTs without cobalt in the zeolite synthesis gel did not affect to any greater extent the zeolite overall surface area. However, the catalyst porosity undergoes significant changes. The mesoporous volume of the zeolites prepared using the 10-20 nm and 20-40 nm diameter CNTs increased by 50% and 80%, respectively. This variation is possibly caused by creating mesoporosity via removal of the CNTs incorporated inside the zeolite crystals during crystallization [28].

After cobalt impregnation, a significant decrease in the sample surface area and pore volume was observed. This decrease was attributed to the presence of Co_3O_4 which can result in a partial plugging of the zeolite pores and "dilution" effect. In all cases, the impregnation with cobalt nitrate also caused a decrease in the zeolite microporous volume. This suggests that at least a part of cobalt is located inside the zeolite framework. The mesoporous volume was however slightly higher in the samples synthetized in the presence of CNTs (without cobalt). This seems to confirm partial incorporation of CNTs into zeolites during their synthesis and subsequent generation of mesoporosity during the CNT combustion.

The samples synthesized with Co/CNT as templates displayed surface area and microporous volume similar to the pure zeolite (Table 4-1), while the mesoporous volume was significantly increased. In comparison to the ZSM-5 samples synthesized with pristine CNTs, the $CoCNT_{(10-20)}$/ZSM-5 and $CoCNT_{(20-40)}$/ZSM-5 mesoporous volume was, respectively, 185% and 220% higher than that of $Co_{(10-20)}$/ZSM-5 and $Co_{(20-40)}$/ZSM-5.

The impact of the CNTs on the zeolite morphology was investigated by TEM (Figure 4-2). The zeolite crystallization in the presence of CNTs led to the formation of large pores in the zeolite crystals (Figure 4-2A). These pores were formed after calcination when the CNTs were removed from the zeolite. The zeolite phase clearly

displayed imprinting coming from CNTs, which were partially encapsulated inside the zeolite crystals during germination [26]. The presence of these regularly shaped pores was not observed on zeolites crystallized in the presence of cobalt impregnated CNT (Figure 4-2B). In the presence of Co/CNT, the formed zeolite crystals took a less regular shape, in agreement with the higher mesopore volumes observed for calcined $CoCNT_{(10-20)}$/ZSM-5 and $CoCNT_{(20-40)}$/ZSM-5 (Table 4-1). Schematically the zeolite synthesis process in the presence of Co/CNT is shown in Figure 4-3. Figure 4-2C and Figure 4-2D show the formation of a uniform layered material. Importantly, these layered structures are only observed when cobalt was present in CNT added to the zeolite synthesis mixture. Indeed, the zeolite morphology replicates that of carbon nanotubes containing cobalt nanoparticles.

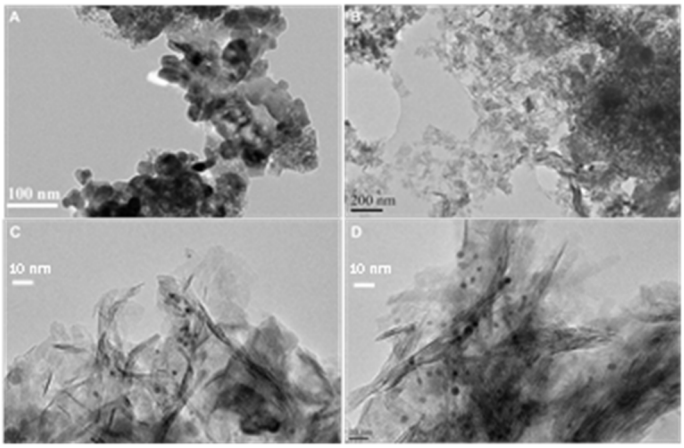

Figure 4-2 TEM images of $Co_{(10-20)}$/ZSM-5 (A), $CoCNT_{(10-20)}$/ZSM-5(B), $CoCNT_{(10-20)}$/ZSM-5 high magnification(C) and $CoCNT_{(20-40)}$/ZSM-5 high magnification.

In addition, Figure 4-2C and Figure 4-2D display a large number of small Co_3O_4 particles with a diameter between 1 and 5 nm as well as larger particles, i.e. 30-50 nm. This suggests that the zeolite contains two types of cobalt particles: smaller cobalt particles of 1-5 nm are located in the zeolite meso- and micropores, while larger cobalt particles of 30-50 nm are situated in the zeolite mesopores and on the outer surface. Note

that only large Co_3O_4 crystallites can be detected in the zeolites by XRD, while it is impossible to detect by XRD cobalt oxide particles smaller than 5 nm.

To confirm uniform distribution of cobalt nanoparticles in the zeolite mesopores, we conducted additional experiments using the STEM-HAADF electron tomography. The typical slices (xy) and (xz) extracted from the 3D volume calculated by tomography of the sample $CoCNT_{(20-40)}$/ZSM-5 prepared using $Co/CNT_{(20-40)}$ as sacrificial template (Figure 4-4) show the presence of cobalt nanoparticles inside the mesoporous structure of zeolite.

Thus, the electron microscopy results are clearly indicative of the important role of cobalt located on CNTs for directing zeolite synthesis. Cobalt species probably act as zeolite nucleation sites for designing mesoporous zeolites with the CNT-type morphology (Figure 4-3).

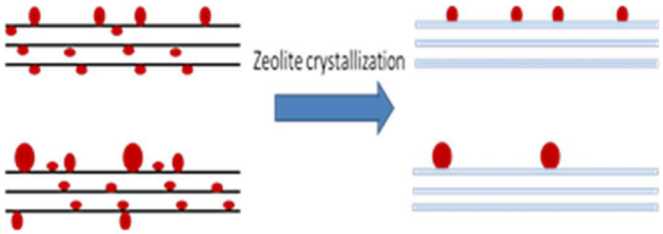

Figure 4-3 Synthesis of ZSM-5 zeolite using Co/CNT as sacrificial templates. Resulting zeolites replicate carbon nanotube morphology.

The TPR profiles of the catalysts are shown in Figure 4-5. The reduction profiles of the impregnated samples were consistent with the two-step Co_3O_4 reduction to metallic Co. Co_3O_4 is first reduced to CoO which is then reduced to metallic Co, thus leading to the formation of two H_2 consumption peaks [13, 40]. In the samples prepared by impregnation, i.e. Co/ZSM-5, $Co_{(10-20)}$/ZSM-5 and $Co_{(20-40)}$/ZSM-5, the characteristic Co_3O_4 reduction peaks overlap leading to a broad peak with a “low temperature” shoulder corresponding to the reduction of Co_3O_4 to CoO.

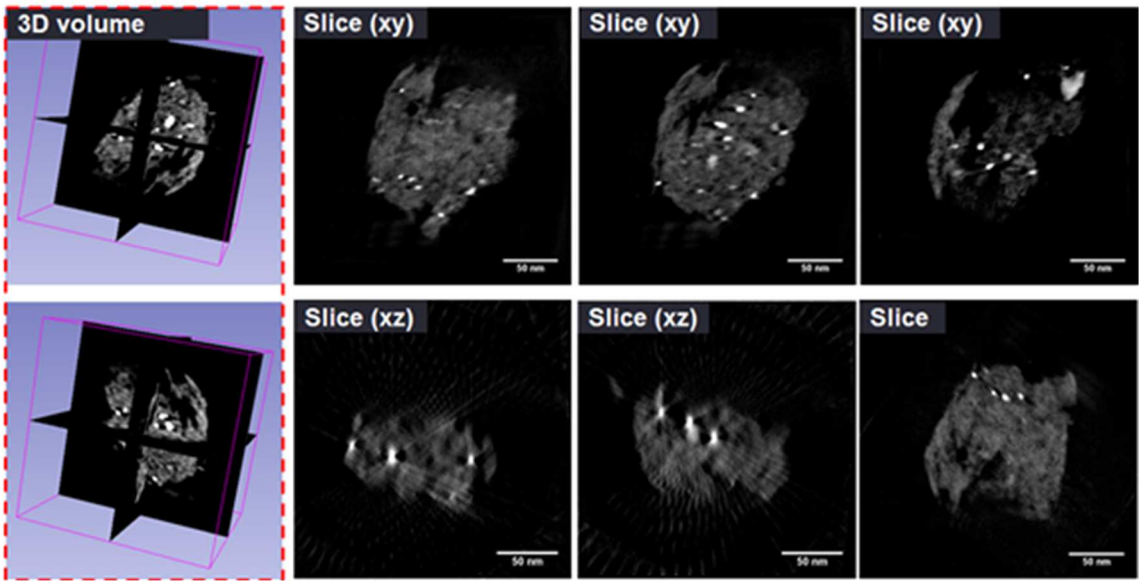

Figure 4-4 Results of STEM-HAADF electron tomography analysis of $CoCNT_{(20-40)}$ZSM-5 catalyst (3D volume and typical slices showing clearly the presence of cobalt nanoparticles inside the zeolite structure).

No peaks at the temperatures higher than 400 °C were observed indicating the absence of isolated exchanged cobalt ions or barely reducible cobalt silicates. Interestingly, the hydrogen consumption profiles were different in the samples synthesized through the germination of zeolite in the presence of Co impregnated CNT. The broad TPR peak which occurred at temperatures below 400 °C, can be attributed to the reduction of Co_3O_4 crystallites to CoO and then to metallic Co [41, 42]. The second hydrogen consumption peak, observed at 700-730 °C, suggests the presence of a more refractory cobalt phase.

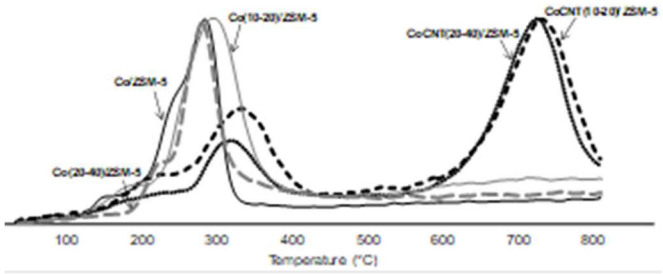

Figure 4-5 Temperature programmed reduction (TPR) profiles of the catalysts.

The formation of amorphous cobalt silicates or aluminates is a possible explanation. Additionally, incorporation of cobalt in the framework structure of the MFI zeolite cannot be completely discarded. Indeed, several authors have reported incorporation of transition metals, including cobalt, into zeolite framework when this metal was present during hydrothermal synthesis [43-46]. The cobalt reducibility and acidity data evaluated from pyridine adsorption and FTIR spectroscopy data are given in Table 4-2.

Table 4-2 Catalyst acidity and cobalt reducibility.

Sample	SiO_2/ $Al2O_3$[a]	Extent of cobalt reduction[b] (%)	Total acidity[c]		Fraction of strong acidity[d]	
			Brönsted ($\mu molg^{-1}$)	Lewis ($\mu molg^{-1}$)	Bönsted	Lewis
Co/ZSM-5	24	82	160	530	0.688	0.708
$Co_{(10-20)}$/ZSM-5	25	69	150	520	0.733	0.769
$Co_{(20-40)}$/ZSM-5	22	58	195	560	0.769	0.768
$CoCNT_{(10-20)}$/ ZSM-5	20	18	250	180	0.800	0.667
$CoCNT_{(20-40)}$ /ZSM-5	21	7	295	130	0.847	0.846

[a]bulk. Determined by XRF
[b]calculated from low temperature (<400°C) TPR peaks assuming reduction of Co_3O_4 into metallic cobalt
[c]determined by pyridine adsorption at 150°C
[d]determined by pyridine adsorption at 350°C

The introduction of CNTs or Co/CNT during the hydrothermal synthesis of the zeolite caused no significant variations in the SiO_2/Al_2O_3 ratio. Significant changes in acid properties were observed between the impregnated samples and the ones when the Co was present during hydrothermal treatment. All the samples synthesized using cobalt nitrate impregnation of the zeolite displayed higher concentration of Lewis acid sites. Unsaturated sites in cobalt oxide particles are known to be responsible for the creation of Lewis acidity [47]. Therefore, higher concentration of Lewis acid sites in the impregnated

samples could be related to the higher loading of cobalt oxide in these catalysts as shown by TPR (Figure 4-5). Much lower concentration of Co_3O_4 (18% and 7% respectively) was detected by TPR in $CoCNT_{(10-20)}$/ZSM-5 and $CoCNT_{(20-40)}$/ZSM-5. These samples showed lower concentration of Lewis acid sites. Note also that the samples synthesized through impregnation showed lower concentration of Brönsted acid sites in comparison with the catalysts synthesized in the presence of Co/CNT. The synthesis of the zeolite directly in the presence of Co/CNT enables higher total Brönsted acid site concentration. The variation of IR intensity of bands attributed to Py adsorption on Brönsted and Lewis acid sites is shown in Figure S2 (SI). The zeolites synthetized using Co/CNT show a higher effective strength of Brönsted acid sites, compared to the samples prepared by impregnation, while the impregnated samples have a much higher concentration of stronger Lewis acid sites (Table 4-2).

Catalytic performance in FT synthesis

The results of the FT catalytic evaluation of the materials are shown in Table 4-3, Figure 4-6 and Figure S3, SI. FT reaction rate varies between 131 and 371 $mmol_{CO}/h.g_{Co}$. The catalytic performance of cobalt zeolite catalysts was tested for at least 30 h. No noticeable evolution of catalytic performance was observed under these conditions. The samples were organized with respect to their activity in the following order: $Co_{(10-20)}$/ZSM-5 >$CoCNT_{(10-20)}$/ZSM-5>$Co_{(20-40)}$/ZSM-5>Co/ZSM-5>$CoCNT_{(20-40)}$/ZSM-5.
The catalytic performance of cobalt catalysts depends on the density of cobalt metallic active sites. Cobalt reducibility is therefore an important parameter.

Table 4-3 Activity and selectivity of the catalysts for the Fischer-Tropsch synthesis reaction (P=2 MPa, GHSV=20-70 L/h g_{Co}, T=250 °C, H_2/CO=2).

Catalyst	FT reaction rate ($mmol_{CO}/h.g_{Co}$)*	Conversion (%)	Selectivity					
			CH_4	C_2-C_4	C_2-C_4 (olefin)	C_2-C_4 (paraffin)	C_2-C_4 (P/O)	C_5^+
Co/ZSM-5	244	39	32.8	19.0	2.7	16.3	6.0	48.1
$Co_{(10-20)}$/ZSM -5	371	28	28.9	18.4	2.0	16.4	8.2	52.7
$Co_{(20-40)}$/ZSM-5	204	29	37.1	29.8	1.5	28.3	18.9	33.1
$CoCNT_{(10-20)}$/ZSM-5	352 (1961)#	42	15.9	13.8	2.8	11.0	3.9	73.1
$CoCNT_{(20-40)}$/ZSM-5	131 (1893)#	28	12.6	13.2	3.0	10.2	3.4	74.2

*time at 24 h.
In brackets: activity on the reducible cobalt basis.

Whereas the TPR profiles of the samples prepared by impregnation suggest the presence of cobalt species reducible at temperatures lower than 450 °C, the TPR profiles (Figure 4-5) of the $CoCNT_{(10-20)}$/ZSM-5 and $CoCNT_{(20-40)}$/ZSM-5 samples synthetized using Co/CNT templates show that only a small portion of cobalt is reducible at 400 °C. Consequently, the samples prepared by addition of Co/CNT during the zeolite synthesis contain a higher fraction of cobalt silicate or aluminates, which are not active for the reaction. Interestingly, when comparing the activity of the catalysts on the basis of reducible cobalt (Table 4-3), both $CoCNT_{(10-20)}$/ZSM-5 and $CoCNT_{(20-40)}$/ZSM-5 displayed a 5 to 10 times higher FT rate compared to the impregnated samples.

The higher activity per reducible cobalt observed on the samples obtained by zeolite germination on Co/CNT can be linked to their enhanced mesoporous structure. Cobalt $CoCNT_{(10-20)}$/ZSM-5 and $CoCNT_{(20-40)}$/ZSM-5 display much higher mesoporous

volume. During the catalyst preparation, cobalt metal nanoparticles introduced using the Co/CNT sacrificial templates are distributed more uniformly within the zeolite mesopores than in the catalysts prepared by impregnation. In addition, catalyst mesoporosity enhanced in CoCNT/ZSM-5 compared to other cobalt zeolite catalysts facilitates diffusion of the reagents and intermediates and removal of the reaction products. The cobalt metal nanoparticles size is also known to be an important factor for the FT synthesis performance [48]. The average size of cobalt oxide crystallites calculated from XRD in all samples was between 27 and 40 nm. In contrast to the samples prepared by impregnation, the TEM images of $CoCNT_{(10-20)}$/ZSM-5 and $CoCNT_{(20-40)}$/ZSM-5 (Figure 4-2 and Figure 4-4) clearly show the presence of Co_3O_4 particles with the size between 1 and 5 nm. Some of these nanoparticles are probably located in the zeolite micropores.

Table 4-3 also shows hydrocarbon selectivities observed in FT synthesis on cobalt–zeolite catalysts for CO conversions in the range of 28 and 42%. Previous reports [3, 13, 16] suggest very small impact of variation of conversion between 30 and 40% on the reaction selectivity. The methane selectivity varies between 13 and 37%. The samples synthesized by impregnation, i.e. Co/ZSM-5, $Co_{(10-20)}$/ZSM-5 and $Co_{(20-40)}$/ZSM-5, display much higher selectivity towards methane formation when compared to $CoCNT_{(10-20)}$/ZSM-5 and $CoCNT_{(20-40)}$/ZSM-5. Notably, methane selectivity was between 1.8 and 2.9 times lower when Co/CNT was present during zeolite synthesis. Similarly, the C_2-C_4 hydrocarbon selectivity was also higher in the samples obtained by cobalt impregnation, in particular on $Co_{(20-40)}$/ZSM-5. Metal particle sizes and their location in the zeolite can explain the selectivity towards short carbon-chain products and methane observed on the impregnated samples. Indeed, during the impregnation, cobalt can diffuse inside the zeolite framework generating small particles, in addition to the larger metal particles located on the zeolite external surface. The diffusion limitations and smaller metal

particles inside the zeolite framework can result in higher methane and lower carbon-chain products selectivities [7]. Lower methane selectivity observed on the CoCNT/ZSM-5 samples could be also due to partial dissolution of extremely small cobalt nanoparticles during zeolite germination around these cobalt species. The occurrence of higher diffusion limitations in the impregnated samples is also consistent with the higher paraffin to olefin ratio (Table 4-3) observed for the impregnated samples. Higher paraffin yields are linked to the higher rate of olefin secondary hydrogenation, which are favored when diffusion limitations and olefin residence time in the zeolite pores are more significant.

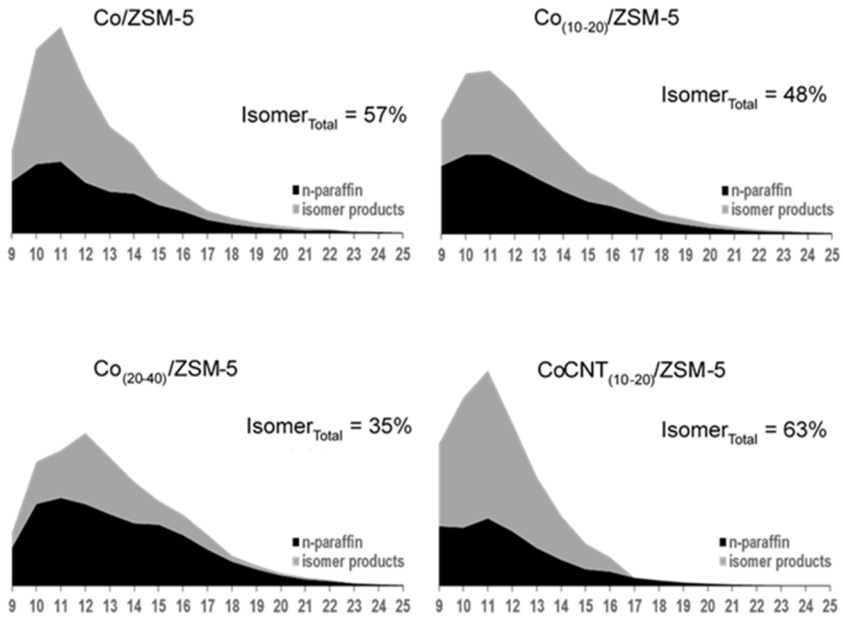

Figure 4-6 Molar distribution of liquid products by carbon number. Isomer$_{Total}$ represents the total amount of isomerized products in the gas fraction. α represents the chain growth coefficient for the ASF distribution.

The liquid product distribution is shown in Figure 4-6, with the respective n-paraffin and isomer product selectivity. Independently of the synthesis procedure, none of the zeolite based catalysts yielded products with more than 25 carbon atoms. Thus, it is possible to assert that the zeolite support is responsible for the reduction of the carbon chain of the FT products. Note that cobalt catalyst on non-acidic supports at similar

reaction conditions show formation of long-chain hydrocarbons with up to 50 carbon atoms [13]. This phenomenon is reflected by the chain growth probability (α) in the Anderson-Schulz-Flory distribution. Figure S3, SI clearly shows modification of the Anderson-Schulz-Flory plot for $CoCNT_{(10-20)}$/ZSM-5 which was synthetized using Co/CNT as sacrificial templates compared to other catalysts. Under similar reaction conditions and on a non-acidic support, e.g. SiO_2, α is commonly around 0.85 for cobalt-based catalysts [13], whereas for the samples in this study the chain growth probability was between 0.58 and 0.68.

The catalytic data suggest strong influence of the zeolite on both isomerization and cracking. On the one hand, the reaction products over cobalt zeolite composites contained significant amounts of isomers because of olefin isomerization on the zeolite Brönsted acid sites (Figure 4-5). On other hand, the carbon chain length over the cobalt zeolite catalysts was much shorter than on silica-supported counterparts. The reduction of the carbon chain growth when using zeolite supports for the FT synthesis is generally attributed to the occurrence of cracking reactions over Brönsted acid sites. The long-chain hydrocarbons resulting from the FT synthesis undergo cracking and isomerization on the zeolite acid sites leading to the formation of the shorter branched hydrocarbons. Indeed, the presence of isomerized hydrocarbons in the wax was observed for all catalysts. The proportion between isomerized products and linear paraffins was largely influenced by the catalyst synthesis procedures. Among the impregnated samples, the selectivity towards isomerization products was higher on Co/ZSM-5 followed by $Co_{(10-20)}$/ZSM-5 and $Co_{(20-40)}$/ZSM-5, respectively with isomer fractions of 57%, 48%, and 35%. Interestingly, $CoCNT_{(10-20)}$/ZSM-5 displayed the highest selectivity towards isomerization products, i.e. fraction of branched isomers of 63%. It is important to mention that hydrocarbons with a higher isomerization degree are more likely to lead to

the formation of tertiary carbocations, which however, can undergo β-scission [49]. Moreover, because of longer residence time in the zeolite micropores, the long chain hydrocarbons are more likely to undergo cracking [50]. Therefore, lower isomerization selectivity observed on the impregnated samples might be linked to a higher cracking rate of the long chain hydrocarbons. The higher selectivity to the C_2-C_4 hydrocarbons, and consequent lower C_5^+ hydrocarbon yield, observed for the impregnated samples could be due to the cracking of larger molecules.

The occurrence of primary and secondary cracking reactions in zeolite materials is often attributed to diffusion limitations [51]. Indeed, a longer residence time of the molecules in the vicinity of acid sites increases the probability of hydrocarbons to undergo cracking while shorter residence time of long chain hydrocarbons in proximity of zeolite acid sites would favor isomerization. The porosity of the impregnated sample is mostly constituted by micropores, while $CoCNT_{(10-20)}$/ZSM-5 and $CoCNT_{(20-40)}$/ZSM-5 have significant mesoporous volume created by the CNT sacrificial templates. The diffusion of higher hydrocarbons is therefore enhanced in the CoCNT/ZSM-5 catalysts, which reduces their residence time inside the zeolite pores and probability of cracking. This suggestion is consistent with higher selectivity to longer carbon chain hydrocarbons observed on $CoCNT_{(10-20)}$/ZSM-5 and $CoCNT_{(20-40)}$/ZSM-5 (Table 4-3). Additionally, the higher cracking reaction rate on the impregnated samples would explain the lower isomerization selectivity on the impregnated catalysts, since the cracking rate of branched hydrocarbons is several orders of magnitude higher [52] than for linear conterparts. On $CoCNT_{(10-20)}$/ZSM-5 and $CoCNT_{(20-40)}$/ZSM-5, the molecules produced by FT synthesis can diffuse more easily, owing to the higher mesoporous volume of the samples. Therefore, the cracking reactions rates lessened due to the faster diffusion and removal

of the isomerized products. This improves isomerization selectivity and selectivity toward long-chain hydrocarbons.

The synthesis of zeolite in the presence of cobalt impregnated CNTs avoids the zeolite pore plugging during cobalt impregnation while generating a complementary mesoporous structure in the zeolite support. Consequently, the diffusion is improved enabling a reduction in the methane and C_2-C_4 hydrocarbon selectivities. Additionally, the liquid products are mainly composed of hydrocarbons up to C_{20} with a higher degree of isomerization. Therefore, the catalysts on the basis of mesoporous zeolites synthesized using carbon nanotubes with cobalt nanoparticles as sacrificial templates are more suitable for the direct production of fuels from syngas than conventional cobalt zeolite supported catalysts prepared by impregnation.

4.4 Conclusion

The use of cobalt impregnated CNTs as sacrificial template enables direct synthesis of cobalt/ZSM-5 mesoporous composite catalysts. The synthesized catalyst had significantly higher mesoporous volume when the synthesis was performed in the presence of Co/CNT than pristine CNTs. The morphology was also strongly affected by the zeolite synthesis method. The samples prepared during zeolite synthesis using the Co/CNT sacrificial templates showed clearly expressed layered structure. This indicates that the cobalt had an impact on the zeolite germination process. At the same time, the final samples had similar Si/Al ratio. The catalysts prepared by impregnated exhibited higher concentration of Lewis acid sites, whereas the catalysts prepared using Co/CNT showed higher amount of Brönsted acid sites. A significant amount of cobalt silicates was observed when cobalt was present during the zeolite synthesis.

The catalytic performance in FT synthesis was significantly affected by the catalyst synthesis procedure. The FT reaction rate normalized by reducible cobalt was 5-10 times higher over the catalysts prepared using Co/CNT as sacrificial template. The higher mesoporous volume of the samples synthesized using Co/CNT during zeolite germination allows a faster diffusion of products and reagents, leading to longer chain products and a reduction of the cracking reactions while improving the selectivity to branched hydrocarbons.

The originality and major advantage of the developed method are relevant to simultaneous creation of zeolite mesoporous structure and introduction of cobalt nanoparticles within zeolite crystallites. Different to the techniques of post-synthesis introduction of cobalt, the method developed in this paper leads to a uniform distribution of cobalt nanoparticles within the zeolite mesoporous structure, enhanced diffusion and catalytic performance in FT reaction.

References

[1] A.Y. Khodakov, W. Chu, P. Fongarland, *Chem. Rev*. **2007**, 107, 1692–1744.

[2] B.H. Davis, M.L. Occelli, *Stud. Surf. Sci. Catal*. **2006**, 163, 1–420.

[3] Q. Zhang, K. Cheng, J. Kang, W. Deng, Y. Wang, *ChemSusChem*, **2014**, 7, 1251–1264.

[4] H. Schulz, *Catal. Today* **2014**, 228, 113–122.

[5] G. Henrici-Olivé, S. Olivé, *Angew. Chemie Int. Ed*. **1976**, 15, 136–141.

[6] C. Bouchy, G. Hastoy, E. Guillon, J.A. Martens, *Oil Gas Sci. Technol. - Rev. IFP* **2009**, 64, 91–112.

[7] V. Subramanian, K. Cheng, C. Lancelot, S. Heyte, S. Paul, S. Moldovan, O. Ersen, M. Marinova, V. V. Ordomsky, and A. Y. Khodakov, *ACS Catal.* **2016**, 6, 1785−1792.

[8] V. V. Ordomsky, A. Y. Khodakov, B. Legras and C. Lancelot, *Catal. Sci. Technol*., **2014**, 4, 2896-2899

[9] F. Pinto, R.N. André, C. Carolino, M. Miranda, *Fuel Process. Technol*. **2014**, 126, 19–29.

[10] T.-S. Zhao, J. Chang, Y. Yoneyama, N. Tsubaki, *Ind. Eng. Chem. Res*. **2005**, 44, 769–775.

[11] F.G. Botes, W. Böhringer, *Appl. Catal. A*. **2004**, 267, 217–225.

[12] N. Tsubaki, Y. Yoneyama, K. Michiki, K. Fujimoto, *Catal. Commun*. **2003**, 4, 108–111..

[13] V. Subramanian, V.L. Zholobenko, K. Cheng, C. Lancelot, S. Heyte, J. Thuriot, S. Paul, V. V. Ordomsky, A.Y. Khodakov, *ChemCatChem* **2016**, 8, 380–389.

[14] Z.W. Liu, X. Li, K. Asami, K. Fujimoto, *Catal. Commun*. **2005**, 6, 503–506.

[15] S. Bessell, *Appl. Catal. A*. **1995**, 126, 235–244.

[16] A. Carvalho, M. Marinova, N. Batalha, N. R. Marcilio, A. Y. Khodakov, and V. V. Ordomsky, *Catal. Sci. Technol.,* **2017**, 7, 5019-5027.

[17] D.J. Koh, J.S. Chung, Y.G. Kim, *Ind. Eng. Chem. Res*. **1995**, 34, 1969–1975.

[18] K. Jothimurugesan, S.K. Gangwal, *Ind. Eng. Chem. Res*. **1998**, 37, 1181–1188.

[19] G. Yang, C. Xing, W. Hirohama, Y. Jin, C. Zeng, Y. Suehiro, T. Wang, Y. Yoneyama, N. Tsubaki, *Catal. Today* **2013**, 215, 29–35..

[20] X. Li, J. He, M. Meng, Y. Yoneyama, N. Tsubaki, *J. Catal.* **2009**, 265, 26–34

[21] A. Martínez, J. Rollán, M.A. Arribas, H.S. Cerqueira, A.F. Costa, E.F. S.-Aguiar, *J. Catal.* **2007**, 249, 162–173.

[22] A. Martínez, S. Valencia, R. Murciano, H.S. Cerqueira, A.F. Costa, E.F. Eduardo, *Appl. Catal. A* **2008**, 346, 117–125

[23] Z.W. Liu, X. Li, K. Asami, K. Fujimoto, *Fuel Process. Technol.* **2007**, 88, 165–170.

[24] S. Bessell, *Appl. Catal. A* **1993**, 96, 253–268.

[25] K. Cheng, L. Zhang, J. Kang, X. Peng, Q. Zhang, Y. Wang, *Chem. - A Eur. J.* **2015**, 21, 1928–1937.

[26] S. Sartipi, M. Alberts, M.J. Meijerink, T.C. Keller, J. Pérez-Ramírez, J. Gascon, F. Kapteijn, *ChemSusChem* **2013**, 6, 1646–1650.

[27] M. Kustova, K. Egeblad, C.H. Christensen, A.L. Kustov, C.H. Christensen, *Stud. Surf. Sci. Catal.* **2007**, 170, 267–275.

[28] D.P. Serrano, J.M. Escola, P. Pizarro, *Chem. Soc. Rev.* **2013**, 42, 4004–4035.

[29] Y. Wang, Y. Jiang, J. Huang, J. Liang, H. Wang, Z. Li, J. Wu, M. Li, Y. Zhao, J. Niu, *Fuel* **2016**, 174, 17–24

[30] S. Sartipi, K. Parashar, M.J. Valero-Romero, V.P. Santos, B. Van Der Linden, M. Makkee, F. Kapteijn, J. Gascon, *J. Catal.* **2013**, 305, 179–190.

[31] J. Plana-Pallejà, S. Abelló, C. Berrueco, D. Montané, *Appl. Catal. A* **2016**, 515, 126–135.

[32] Q. Lin, G. Yang, Q. Chen, R. Fan, Y. Yoneyama, H. Wan, N. Tsubaki, *ChemCatChem* **2015**, 7, 682–689.

[33] G. Huang, P. Ji, H. Xu, J.-G. Jiang, L. Chen, P. Wu, *Microporous Mesoporous Mater.* **2017**, 248, 30–39.

[34] D. Verboekend, J. Perez-Ramirez, *Catal. Sci. Technol.* **2011**, 1, 879–890.

[35] S. Yang, C. Yu, L. Yu, S. Miao, M. Zou, C. Jin, D. Zhang, L. Xu, S. Huang, *Angew. Chemie Int. Ed.* **2017**, 56, 12553–12556

[36] P. Sazama, Z. Sobalik, J. Dedecek, I. Jakubec, V. Parvulescu, Z. Bastl, J. Rathousky, H. Jirglova, *Angew. Chemie Int. Ed.* **2013**, 52, 2038–2041

[37] Y. Fang, H. Hu, G. Chen, *Microporous Mesoporous Mater* **2008**, 113, 481–489.

[38] L. Tosheva, V. Valtchev, J. Sterte, *Micropor. Mesoporous Mater.* **2000**, 35, 621–629.

[39] F.-S. Xiao, L. Wang, C. Yin, K. Lin, Y. Di, J. Li, R. Xu, D.S. Su, R. Schlögl, T. Yokoi, T. Tatsumi, *Angew. Chemie Int. Ed.* **2006**, 45, 3090–3093.

[40] C. Huang, Z. Ma, P. Xie, Y. Yue, W. Hua, Z. Gao, *J. Mol. Catal. A 2015,* 400, 90–94.

[41] E. Van Steen, G.S. Sewell, R.A. Makhothe, C. Micklethwaite, H. Manstein, M. De Lange, C.T.O. Connor, *J.Catal.* **1996**, 229, 220–229.

[42] S.J. Jong, S. Cheng, *Appl. Catal. A* **1995**, 126, 51–66.

[43] Y. Yao, F. Cao, J. Gu, Y. Wu, Y. Zhou, J. Wang, *J. Porous Mater.* **2013**, 20, 891–896.

[44] S.N. Azizi, S. Ehsani Tilami, *J. Solid State Chem.* **2013**, 198, 138–142.

[45] Q. Wang, J. Wang, Y. Zhou, X. Lin, *J. Porous Mater.* **2013**, 20, 1519–1523.

[46] A. Rokicińska, M. Drozdek, B. Dudek, B. Gil, P. Michorczyk, D. Brouri, S. Dzwigaj, P. Kuśtrowski, *Appl. Catal. B* **2017**,.212, 59–67.

[47] G.A.. Mekhemer, H.M.. Abd-Allah, S.A.. Mansour, *Colloids Surfaces A Physicochem. Eng. Asp.* **1999**, 160, 251–259.

[48] Oyvind Borg, P.D.C. Dietzel, A.I. Spjelkavik, E.Z. Tveten, J.C. Walmsley, S. Diplas, S. Eri, A. Holmen, E. Rytter, *J. Catal.* **2008**, 259, 161–164.

[49] J.A. Martens, M. Tielen, P.A. Jacobs, Catal. Today 1987, 1, 435–453.

[50] A. Corma, P.J. Miguel, A. V. Orchillés, *Appl. Catal. A* **1994**, 117, 29–40.

[51] S. van Donk, A.H. Janssen, J.H. Bitter, K.P. de Jong, *Catal. Rev.* **2003**, 45, 297–319.

[52] J. Weitkamp, S. Ernst, *Catal. Today* **1994**, 19, 107–149.

[53] S. Chambrey, P. Fongarland, H. Karaca, S. Piché, A. Griboval-Constant, D. Schweich, F. Luck, S. Savin, A.Y. Khodakov, *Catal. Today* **2011**, 171, 201-206

Supporting Information

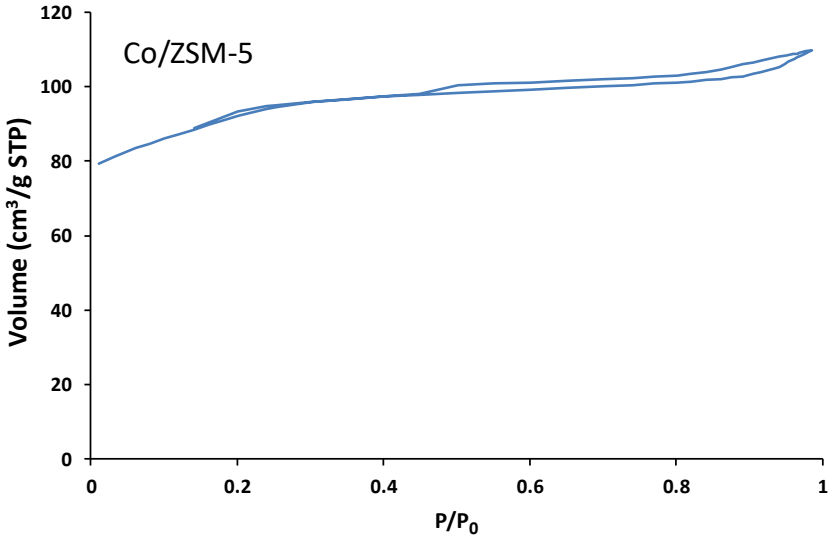

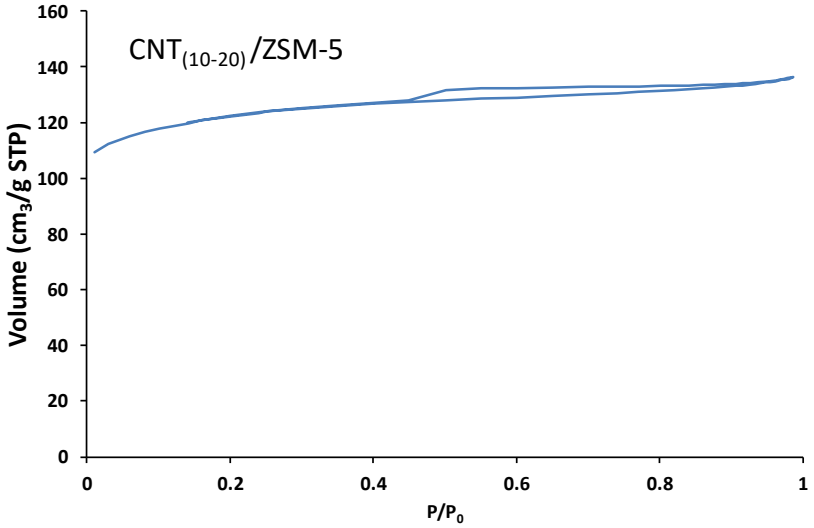

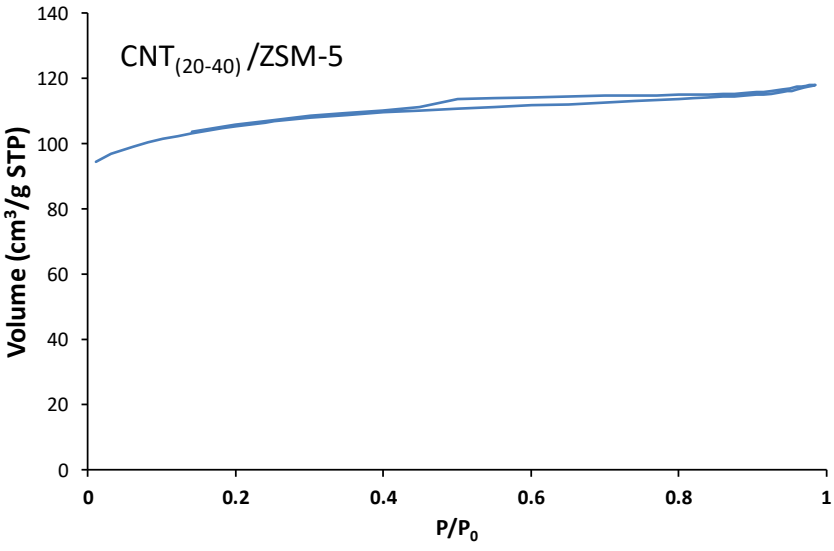

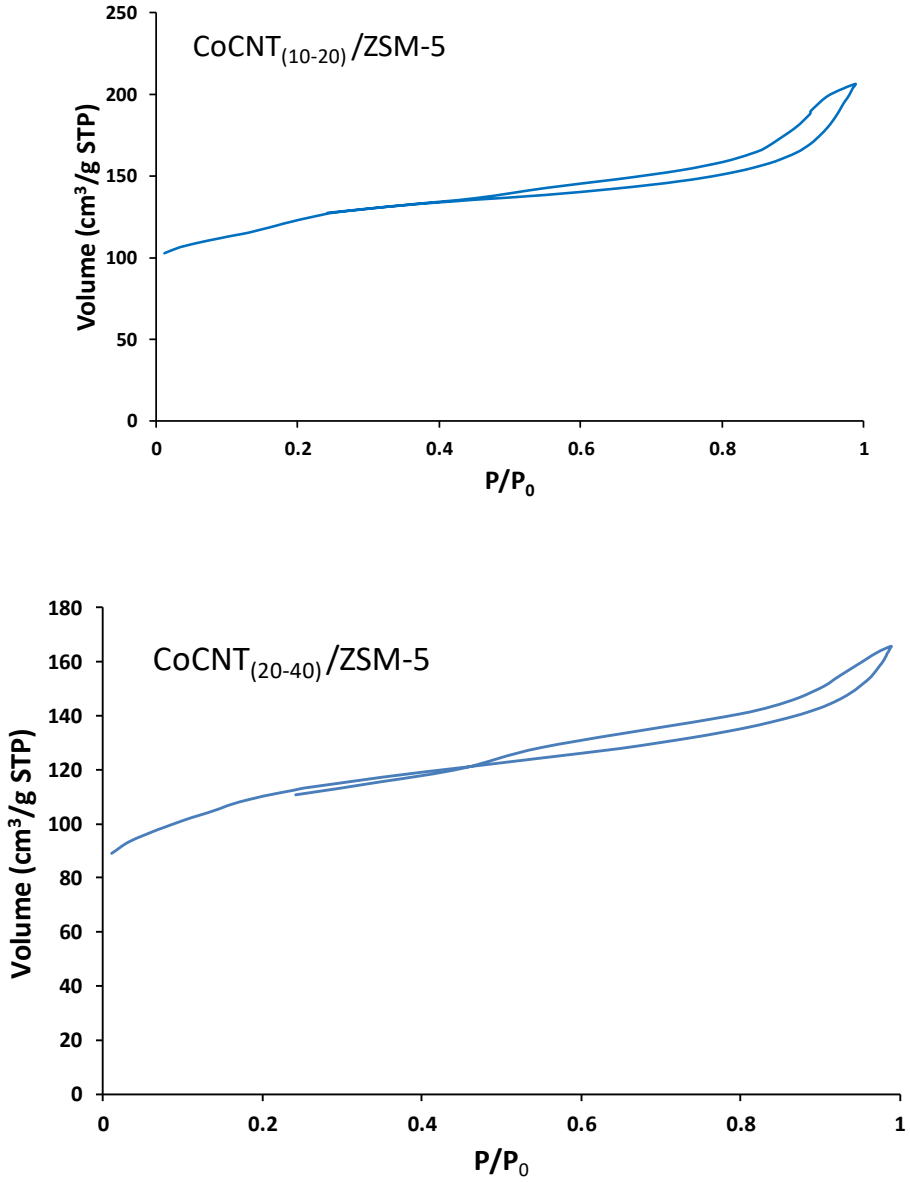

Figure S4. Nitrogen adsorption-desorption isotherms on cobalt zeolite composite catalysts.

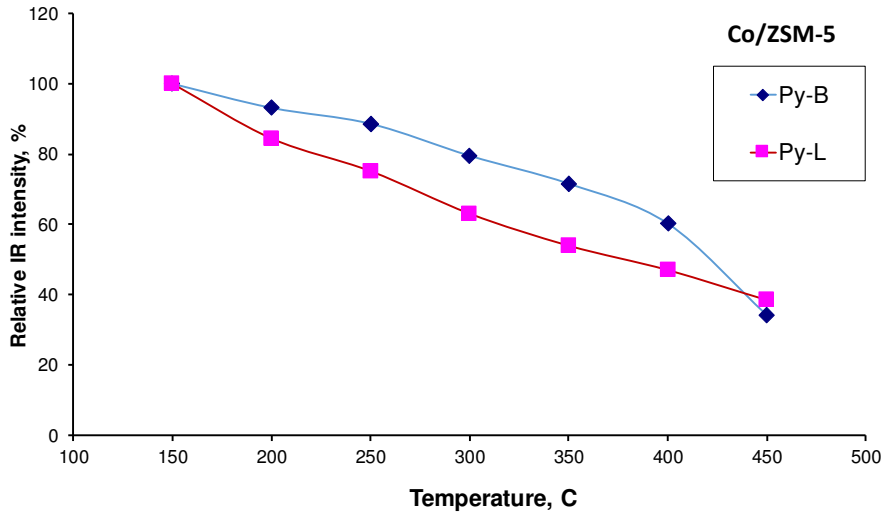

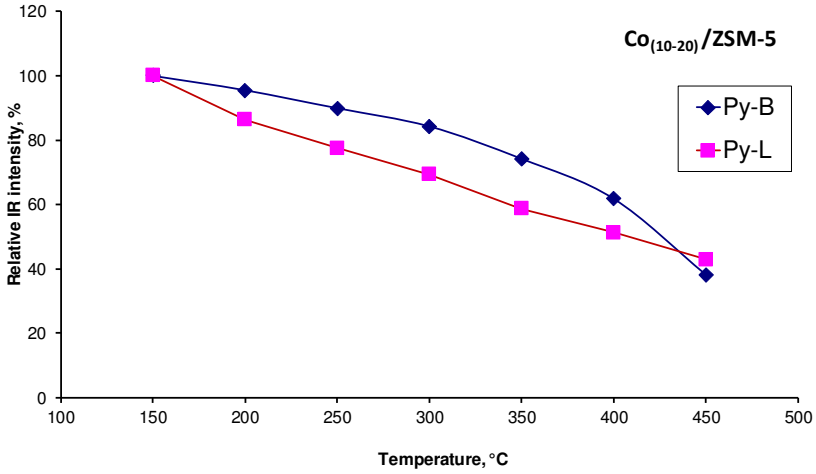

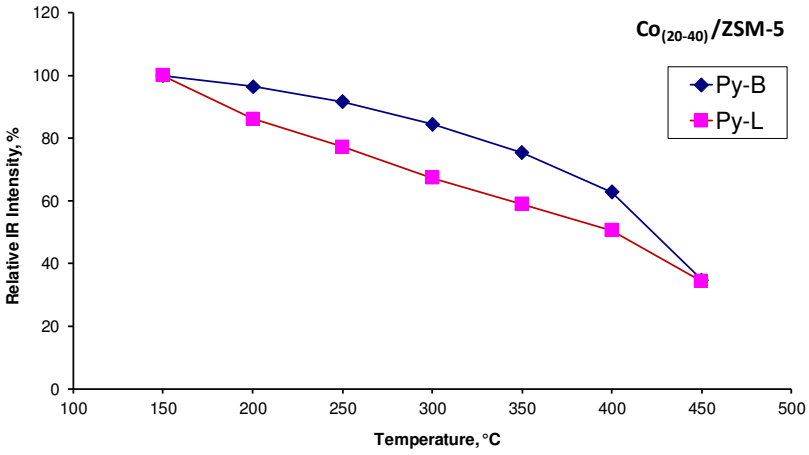

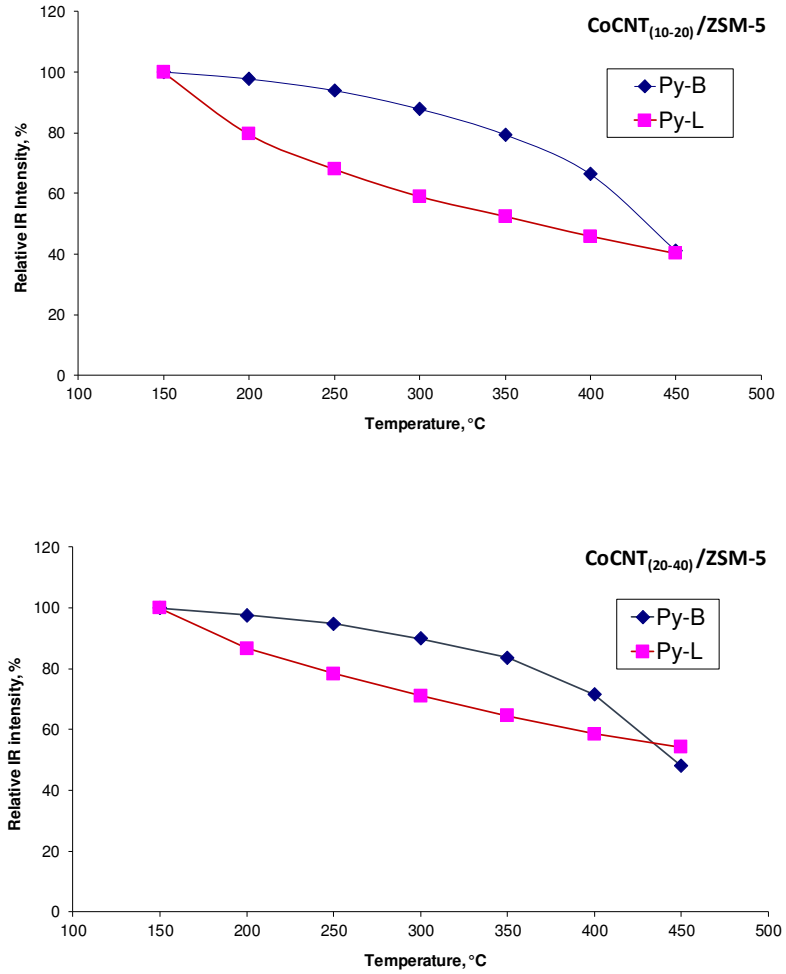

Figure S5. Variation of intensities of IR bands attributed to Pyridine adsorbed on Brönsted and Lewis acid sites as functions of desorption temperature on different cobalt-zeolite catalysts. The zeolites synthetized using CNT impregnated with cobalt have slightly stronger Brönsted acid sites compared to the samples prepared by impregnation.

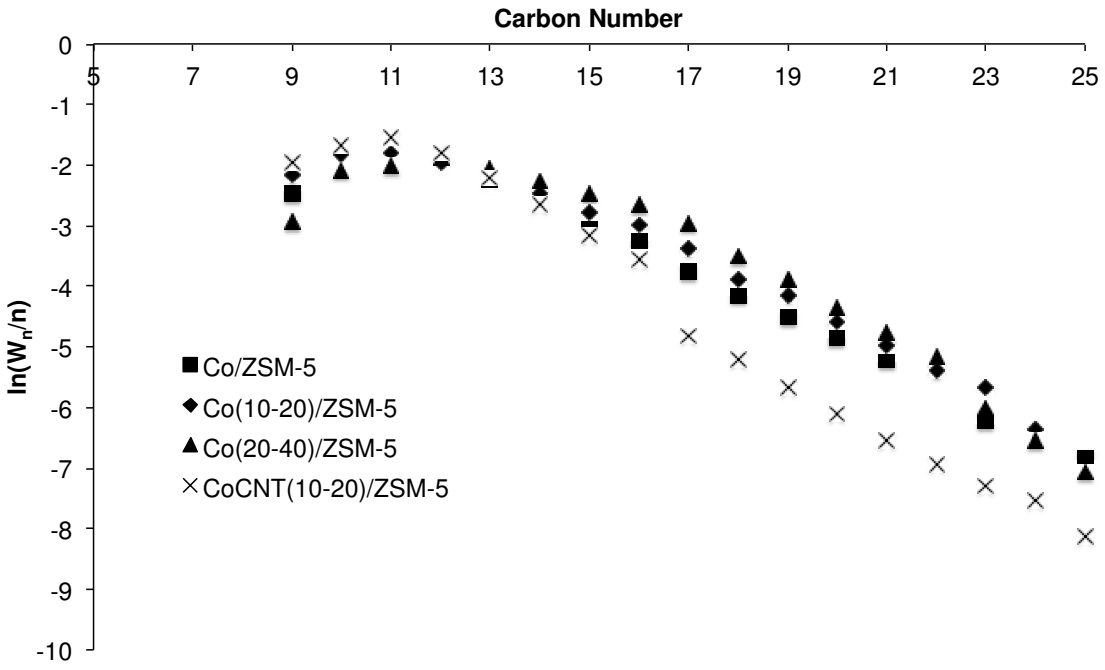

Figure S6. ASF distribution plot for the wax products obtained from the FT synthesis reaction.

Chapter 5: Multifaceted Role of Metal Carbon Nanotube Templates in the Synthesis of Hierarchical Zeolite Composite Catalysts

Manuscript submitted for publication

Abstract: Metal zeolite nanocomposites are extensively used in heterogeneous catalysis. Small zeolite pore size and non-uniform distribution of the metal component within the zeolite structure heavily reduce the efficiency of these catalysts. In this work, we propose a new strategy for the design of hierarchical zeolites with specific shape, enhanced mesoporosity and uniform distribution of highly dispersed metals such as cobalt, nickel, and magnesium in the zeolite crystals. The strategy involves using metal carbon nanotubes as structure directing agents. Multiple roles of the metal carbon nanotubes in the zeolite synthesis are uncovered. First, they serve as a replica to create zeolite with specific fibrous shape. Second, they fulfill the role of a mesoporogen and increase 3-5 times the zeolite secondary porosity. Finally, they operate a vehicle to uniformly introduce the metal functions inside the mesoporous zeolites. Importantly, the presence of metals in carbon nanotubes is essential for the enhancement of mesoporosity. The catalysts prepared using metal carbon nanotube templates have shown enhanced catalytic performance in Fischer-Tropsch synthesis, hydrogenation of aromatics and anisole acylation.

Keywords: hierarchical zeolite; hard template; replicas; catalyst; promotion; metal dispersion; acidity

5.1 Introduction

Zeolites are microporous crystalline solids with a regular pore system, which have found numerous applications in industrial processes such as oil refining, organic synthesis, adsorption and separation. The zeolite crystal structure determines the size and geometry of the micropores. They are very specific for a given type of the zeolite [1] and often are comparable with the size of reacting molecules. Smaller and uniform pores lead to stronger interaction between the zeolite and reacting molecules and thus, introduce geometric, electronic confinement and shape selectivity phenomena for a catalytic reaction involving bulky molecules [2]. Zeolites can be tailored to specific catalytic applications by controlling Brönsted and Lewis acidity as well as by introducing new catalytic functions, including metal cations, clusters, metal oxides, organic complexes and enzymes.

Zeolites in their hydrogen form are considered as acid catalysts, while metal-containing zeolites are considered as bifunctional catalysts that exhibit complex behavior. The concentrations and intrinsic activity of the metal and acid sites, and in particular, their localization within the zeolite structure are of utmost importance for the catalyst activity, selectivity and stability [3-5]. Ion exchange, impregnation, or introduction of a metal precursor to the zeolite synthesis gel have been often used for synthesis of metal-zeolite composites. In the metal-zeolite composites, metal can be present either in the form of isolated cations in the cationic sites, or in the form of tetrahedrally coordinated cations isomorphously substituting silicon or aluminum atoms in the zeolite framework, or finally, as small metal or oxide nanoparticles localized within the zeolite micro- or mesopores. The distribution of metal component with the zeolite is of paramount importance for the resulting catalytic performance. The distance between metal

nanoparticles and acid sites, "site intimacy" [6], diffusional limitations for the intermediates during their transport from one site to another [7-10] strongly affect the performance of many catalytic reactions

Very small pore size of zeolites (~1 nm) imposes diffusional limitations for many catalytic reactions, in particular for those, involving bulky molecules. In order to overcome these, numerous efforts have made to synthesize nano-sized zeolite crystals [11], extra-large pore zeolites [12], or mesoporous zeolites [13, 14], the latter are often referred as hierarchical zeolites. The hierarchical zeolites contain, in addition to the well-defined micropore system, mesopores with the diameters in the range of 2-50 nm [15, 16]. Different to zeolite micropores, the size, shape and orientation of these mesopores are not directly related to the zeolite crystalline structure. The methods used for the preparation of hierarchical zeolites could be summarized into two main groups. (i) Bottom-up methods, where sacrificial templates of desired size and dimensions are incorporated into zeolite crystals during the crystallization step. These templates are then eliminated by combustion or extraction. (ii) Top-down methods, including post-synthesis chemical treatment of zeolite crystals leading to the extraction of aluminum and silicon atoms and partial dissolution of the zeolite framework. Note that it is usually much more difficult to maintain zeolites with good crystallinity and to generate uniform mesopores using top-down methods such as steam treatment, acid and alkaline leaching [17] compared to the bottom-up strategies.

Both hard [18, 19] and soft templates [20, 21] have been utilized to synthetize hierarchical zeolites using the bottom up approach. The hard templates usually include carbon nanoparticles, nanotubes and polymer beads, while various cationic surfactants, organosilane, cationic polymer, and ionic liquids [22, 23] are considered as soft secondary

templates. Both hard and soft templates could be removed by calcination. Among the hard templates, carbon nanotubes (CNT) have attracted particular attention in the literature. CNT are very versatile materials [24, 25] as their properties are strongly affected by the presence of hydrophobic or hydrophilic functional groups, metals, oxide and other dopants. As a result, the properties of hierarchical zeolites prepared using CNT as secondary templates are strongly affected by the features of CNT and zeolite synthesis conditions. To the best of our knowledge, no studies have been performed to evaluate the effect of different metals present in CNT on the zeolite crystallization and mesoporosity.

In this chapter, metal containing CNT (Me-CNT) were applied as secondary templates for synthesis of hierarchical ZSM-5 zeolites. We uncovered at least three roles of Me-CNT in the zeolite synthesis. First, they strongly affect the shape of the synthesized zeolites, which seem to be replicas of CNT and show distinct fibrous texture. Second, the Me-CNT plays a role of mesoporogen and strongly enhance the zeolite mesoporous volume. Finally, zeolite synthesis in the presence of Me-CNT offers the opportunity to simultaneously introduce new catalytic functions leading to bifunctional metal-zeolite catalysts. The introduced metals are then uniformly distributed within the zeolite crystals. The presence of metal species in CNT is essential to obtain the observed phenomena. Note that only very limited impact on zeolite porous structure was observed by using metal-free CNT as secondary hard templates. The metal zeolite composites prepared using metal-CNT templates exhibited improved catalytic performance in Fischer-Tropsch synthesis, hydrogenation of aromatics and anisole acylation with hexanoic acid.

5.2 Experimental

CNT and their impregnation with metal precursors

Two multi-wall CNT samples (Iolitec nanomaterial, 95%) with different diameters, i.e. 10-20 nm and 20-40 nm, were used. The CNT were pretreated with nitric acid to remove all metal contaminations. This treatment also converted CNT into their hydrophilic forms. Typically, 3 g of CNT were pretreated in 210 mL of concentrated HNO_3 (68%) for 14 h under reflux. Next, the samples were filtered, washed with distilled water until pH = 7 and dried at 100 ºC overnight.

Metals were added to CNT via the wet impregnation method using $Co(NO_3)_2$ $6H_2O$ (Sigma-Aldrich) and $Pt(NH_3)_4(NO_3)_2$ (Sigma-Aldrich), $Mg(NO_3)_2$ $6H_2O$ (Sigma-Aldrich) and $Ni(NO_3)_2$ $6H_2O$ (Sigma-Aldrich) as precursors. Co-impregnation with platinum was solely used for the preparation of cobalt catalysts. Typically, the precursor amount for impregnation was calculated to obtain 20 wt.% of the metal in the final catalyst. The mixture was subjected to ultrasonic treatment for 30 min and dried at 80 °C. The samples were calcined at 400 °C for 4 h under nitrogen atmosphere.

After calcination in nitrogen, the hydrophilic properties of CNT were partially lost. In order to restore the CNT hydrophilicity, the samples were treated with H_2O_2. Typically, 30 mL of 1:1 H_2O_2 (Sigma-Aldrich, 35%) and distilled water mixture were added to 2.56 g of impregnated CNT, sonicated for 30 min and dried at 80 °C. The metal supported CNT catalysts are denoted as Metal/$CNT_{(x)}$ (where Metal=Co, Ni or Mg) and x is the CNT diameter in nm.

Synthesis of hierarchical metal-ZSM-5 zeolites

The ZSM-5 zeolite was synthesized by using a synthesis gel with the initial composition of $2.7NaCl:1Al_2O_3:12.5TPAOH:55.8SiO_2:7500H_2O$. The synthesis of the zeolite was carried out by mixing sodium chloride (0.380 g, Janssen Chimica, P.A.), tetrapropylammonium hydroxide (3.0 g, Sigma-Aldrich, 1 M in H_2O), sodium aluminate (0.040 g, Sigma-Aldrich) and distilled water until a clear solution was obtained. Metal/CNT (0.24 g) and tetraethyl-orthosilicate (TEOS, 2.8 g, Sigma-Aldrich, 99%) were added to the previous solution. Then, the synthesis gel was aged for 1 h at room temperature under stirring. The synthesis gel was put inside a Teflon-lined autoclave (40 mL). The zeolite crystallization was performed under static condition at 170 °C for 24 h. After cooling down, the solid was recovered by filtration and washed until pH=7 was achieved. The final solid was calcined at 600 °C for 4 h in air. Further details relevant to the introduction of cobalt with CNT into ZSM-5 zeolite are available elsewhere [26].

For comparison, the zeolite syntheses using pure CNT were performed under the same conditions using a similar gel composition. The resulting zeolites were then impregnated using incipient wetness method with cobalt, nickel and magnesium nitrates as precursors.

In order to obtain the zeolite acid form, two successive exchanges using 2 M NH_4NO_3 aqueous solution at 80 °C for 1 h (1 g of zeolite per 50 mL of solution) were performed. The ammonium forms were converted into the protonic forms by calcination at 450 °C for 4 h in air. The synthesized samples were denoted as: $MetalCNT_{(x)}$/ZSM-5 (where Metal= Co, Ni or Mg) for the samples synthesized using metal impregnated CNT (x represents the CNT diameter used in the synthesis, i.e. 10-20 or 20-40 nm) and $CTN_{(x)}$/ZSM-5 for the samples synthesized with pure CNT as secondary templates. Metal/ZSM-5 stands for the zeolite synthetized without any secondary template and

conventionally impregnated after its synthesis with a metal nitrate followed by the nitrate decomposition via calcination in air at 500 °C.

Catalyst characterization

The textural properties of the samples were determined by N_2 physisorption on a Micromeritics ASAP 2000 apparatus. Prior to the analysis, the samples were degassed under vacuum (10 µmHg) at 350 °C for 4 h. The total pore volume (TPV) was calculated from the amount of vapor adsorbed at a relative pressure $P/P_0 = 0.97$. The sample surface area was estimated by the BET method, while the micropore volume was calculated using the deBoer t-plot method.

The samples were characterized by X-ray diffraction (XRD) with a D8 advance diffractometer equipped with an energy dispersive type detector and a monochromatic CuK_α radiation source. The samples were analyzed using a step of 0.02° with an acquisition time of 0.5 s.

The sample chemical composition was determined by X-ray fluorescence (XRF) using a M4 TORNADO (Bruker) spectrometer. This instrument was equipped with 2 anodes a rhodium X-ray tube 50 kV/600 mA (30 W) and a tungsten X-Ray tube 50 kV/700 mA (35 W). For sample characterization, the rhodium X-ray tube with a poly-capillary lens enabling excitation of an area of 200 µm was utilised. A Silicon-Drift Si(Li) detector with Peltier cooling (253°K) and a resolution <145 eV at 100000 cps (Mn Kα) was used. The measurements were conducted under vacuum (20 mbar). Quantitative analysis was carried out using fundamental parameter (FP) (standardless).

The catalyst reducibility was studied using an Autochem II (Micrometrics) temperature-programmed reduction (TPR) system. The samples were reduced under a flow of 5 % H_2 in argon (50 mL/min) and heated up to 800 °C at a rate of 5 °C/min. The

catalyst Brönsted and Lewis acidities were monitored by infrared spectroscopy (IR) with pyridine adsorption. The IR spectra were recorded using a Thermo iS10 spectrometer (DTGC detector, 64 scans at 4 cm^{-1} resolution). The samples were pretreated under vacuum (10^{-}5 Torr) at 450 °C for 5 h. After pre-treatment, pyridine was adsorbed on the sample and the sample was then heated under vacuum (10^{-5} Torr) at 150 °C. The spectra before and after the Py adsorption were collected at ambient temperature. The amounts of Brönsted and Lewis acid sites were calculated using the intensity of bands at ~1545 cm^{-1} and ~1455 cm^{-1}, respectively. The absorption coefficients ε(B)=1.08 for Brönsted acid sites (peak at ~1545 cm^{-1}) and ε(L)=1.71 cm mol^{-1} for Lewis acid sites (peaks at ~1455-1445 cm^{-1}) were used for quantification of the zeolite acid sites.

The TEM observations of the samples were obtained by using a Jeol 2100F instrument operated at 200 kV. Before the analysis, the samples were dispersed by ultrasound in ethanol for 5 min, and a drop of the suspension was deposited onto a carbon membrane on a 300 mesh copper grid. The STEM-HAADF tomographic analysis was carried out on a Jeol 2100F (field emission gun) microscope operating at 200 kV by using a spot size of 1.1 Å with a current density of 0.5 pA $Å^{-1}$. Selected Area Electron Diffraction (SAED) patterns were recorded using a US1000XP CCD camera with an exposure time of 2 s on circular areas of 200 nm diameter.

Catalytic tests

Hydrogenation of aromatics: Toluene or triisopropylbenzene hydrogenations were carried out in a fixed-bed reactor. The catalyst (50 mg) was loaded in the stainless-steel reactor and then activated in a H_2 gas flow (10 cm^3/min, atmospheric pressure) at 400 C for 4 h with a heating rate of 2 °C/min. The reactor was cooled below to 50 °C, a hydrogen flow with a pressure of 20 bar was introduced into the reactor. The temperature

was raised at 1 °C/min to the required reaction temperature (250 °C). The liquid reagents (toluene or triisopropylbenzene) were injected by pump (PHD ULTRA 4400, Harvard Apparatus) with a flow rate (0.8 mL/h). The products were collected in a cold tap and analyzed by a gas chromatograph (Bruker GC-450) equipped with thermal conductivity (TCD) and flame ionization (FID) detectors.

Fischer Tropsch synthesis: the experiments were performed in a fixed-bed reactor. Prior to testing, the samples were reduced in situ in pure H_2 flow (3 cm^3/min) at 400 °C for 4 h with a heating rate of 3°C/min. After the reactor was cooled down to room temperature, the flow was switched to syngas (H_2/CO = 2) and the pressure adjusted to 20 bar. Nitrogen (5% relative to CO) was used as the internal standard. After achieving the desired pressure, the temperature was increased to the reaction temperature, i.e. 250 °C, at a rate of 3 °C/min. The gas space velocities were adjusted to obtain CO conversion of 30-40% for all catalysts. The gaseous reaction products, i.e. up to C_5, were analyzed on-line using a GC equipped with a FID and a TCD detectors (Varian, CP-3800). The remaining products (wax) were condensed under pressure and analyzed ex situ on a Shimadzu GC with FID (2010-Plus-AF).

Anisole acylation: the activity of all catalysts was evaluated in the acylation reaction between anisole and hexanoic acid according to the following protocol. The catalyst (20 mg) was added to a mixture of anisole (2 g) and hexanoic acid (0.3 g) in a reflux reactor system. Upon sealing, the tube was heated at 180 °C for 2 h. The products were analyzed by gas chromatography.

5.3 Results and Discussion

The nitrogen adsorption–desorption isotherms for the catalysts prepared by impregnation and synthesized using the Me/CNT templates are shown in Figure 5-1.

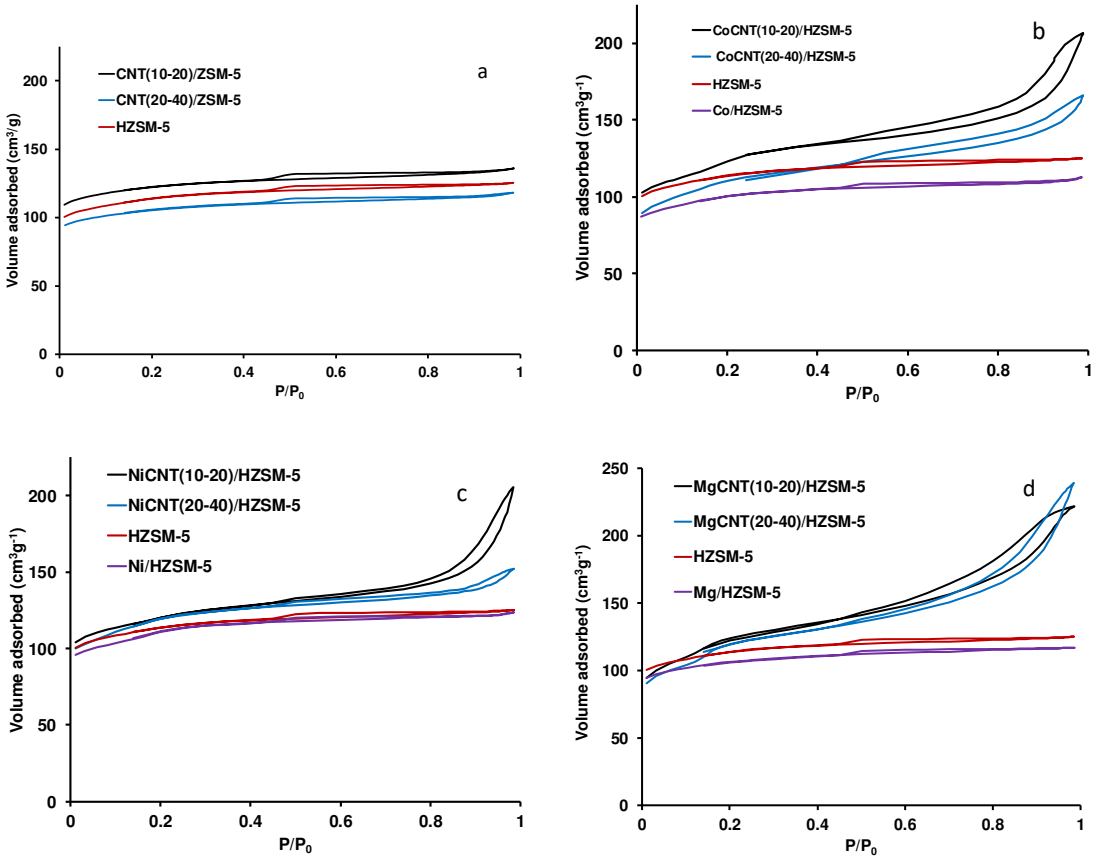

Figure 5-1 Low temperature nitrogen adsorption-desorption isotherms on the HZSM-5 zeolite synthetized with and without addition of CNT (a) cobalt (b), nickel (c) and magnesium (d) ZSM-5 catalysts.

The ZSM-5 sample displays a type-I isotherm exhibiting a sharp uptake at low relative pressure followed by a plateau with a hardly visible hysteresis at P/P_0>0.5. This type of isotherm is usually observed for microporous materials with textural mesoporosity generated by aggregation of small zeolite crystallites. Similar isotherms shapes were observed for the $CNT_{(10-20)}$/ZSM-5 and $CNT_{(20-40)}$/ZSM-5 samples synthetized using pure CNT as secondary hard templates (Figure 5-1a). Table 5-1 shows that the addition of pure $CNT_{(10-20)}$ during the ZSM-5 zeolite synthesis results in a slight increase in the BET surface area and pore volume. The use of $CNT_{(20-40)}$ during the ZSM-5 zeolite synthesis did not change substantially the porous characteristics of the zeolite.

Table 5-1. Catalyst characterization data

Sample	S_{BET} (m^2g^{-1})	V_{tot} (cm^3g^{-1})	V_{mic} (cm^3g^{-1})	V_{meso} (m^2g^{-1})	Metal content (wt%)	Lewis ($\mu molg^{-1}$)	Brönsted ($\mu molg^{-1}$)
ZSM-5	425	0.19	0.13	0.06	-	36	314
$CNT_{(10-20)}$/ZSM-5	460	0.21	0.15	0.06	-	-	-
$CNT_{(20-40)}$/ZSM-5	397	0.18	0.13	0.05	-	-	-
Co/ZSM-5	372	0.17	0.11	0.07	15.6	530	160
$CoCNT_{(10-20)}$/ZSM-5	435	0.32	0.09	0.23	7.8	180	250
$CoCNT_{(20-40)}$/ZSM-5	395	0.25	0.09	0.16	9.4	130	295
Mg/ZSM-5	399	0.18	0.12	0.06	1.5	284	92
$MgCNT_{(10-20)}$/ZSM-5	433	0.34	0.07	0.27	2.3	48	204
$MgCNT_{(20-40)}$/ZSM-5	410	0.35	0.05	0.30	2.1	39	141
Ni/ZSM-5	406	0.19	0.11	0.08	5.0	172	179
$NiCNT_{(10-20)}$/ZSM-5	444	0.29	0.12	0.17	4.5	47	267
$NiCNT_{(20-40)}$/ZSM-5	434	0.23	0.10	0.13	4.6	18	220

The introduction of metals (Co, Mg, Ni) to the zeolite synthesis gel, without using CNT as a secondary template, has only a minor effect on the zeolite porosity and specific surface area resulting in a decrease in the zeolite pore volume and specific surface area (Table 5-1). The difference between the surface area and pore volume of the parent zeolite and its counterparts containing metals may be assigned to both, the effect of zeolite "dilution" by metals and partial pore blocking by the metal species. Only the microporous zeolite volume is affected by impregnation with metals in Co/ZSM-5, Ni/ZSM-5 and Mg/ZSM-5 as compared to the parent ZSM-5 zeolite, while almost no changes are observed in the mesoporous volume. This fact indicates that the metal cations are preferentially located in the zeolite micropores, whereas the major part of the metal species, e.g. metal oxides, in the case of ZSM-5 is located on the zeolite external surface.

Remarkably, rather different isotherms and textural properties were observed for the ZSM-5 zeolites synthetized in the presence of Me/CNT templates. The zeolites prepared in the presence of Co/CNT, Ni/CNT and Mg/CNT templates exhibit a combination of type I and IV isotherms with a significant N_2 uptake at low relative pressure and a hysteresis loop at high relative pressure ($P/P_0 > 0.5$, Figure 5-1b-d). Adsorption of nitrogen in the range of $P/P_0 = 0.5$ - 1.0 and relevant hysteresis can be explained by mesoporosity developed by the presence of cobalt, nickel or magnesium oxides supported on CNT. Note that almost no increase in the zeolite mesoporosoity was observed when pure $CNT_{(10\text{-}20)}$ or $CNT_{(20\text{-}40)}$ were used as mesoporous hard templates (Table 5-1). Importantly, the presence of metal species on CNT is essential for the synthesis of ZSM-5 zeolite with enhanced mesoporous volume. A slight increase in the BET surface area was also observed for $CoCNT_{(10\text{-}20)}$/ZSM-5, $NiCNT_{(10\text{-}20)}$/ZSM-5 and $MgCNT_{(10\text{-}20)}$/ZSM-5, while the BET surface area slightly decreases when using the $Me/CNT_{(20\text{-}40)}$ templates. Thus, the most significant effect of using CNT containing cobalt, nickel and magnesium is the substantial increase in the mesoporous volume. The zeolite mesoporous volume increases 2.5-4 times, when using $CoCNT_{(10\text{-}20)}$ and $Co/CNT_{(20\text{-}40)}$, 4.5-5 times, when using $MgCNT_{(10\text{-}20)}$ and $MgCNT_{(20\text{-}40)}$ and 2.2-3 times for $NiCNT_{(10\text{-}20)}$ and $NiCNT_{(20\text{-}40)}$ (Table 5-1). Note that the zeolite micropore volume (between 0.09-0.13 cm^3/g) is only slightly affected by CNT supported metals used as secondary templates.

Figure 5-2 displays XRD patterns of all samples included in the present study. The characteitic XRD peaks of the MFI structure are observed in all samples, regardless of the employed synthesis procedure. No halo peaks, which can be attributed to the amorphous phase, have been observed. Note that the presence of metals in the catalysts leads to somewhat lower intensity of the zeolite XRD patterns, which is due to the dilution of the MFI phase with the metal oxides. In the Co/ZSM-5, $CoCNT_{(10-20)}$/ZSM-5 or $CoCNT_{(20-40)}$/ZSM-5 samples a peak at 36.9 ° which is characteritic to the Co_3O_4 can be observed. The particle size of Co_3O_4 calculated using the Scherrer equation (Table 5-1) was 27-44 nm. Such large size suggests that the main fraction of cobalt oxide is located either in large mesopores or on the zeolite external surface. The Ni/ZSM-5 catalyst prepared using impregnation with nickel nitrate showed a very low intense XRD peaks at 43.2° attributed to the face-centered cubic phase NiO (JCPDS card no. #47-1049). The $Ni/CNT_{(10-20)}$/ZSM-5 or $Ni/CNT_{(20-40)}$/ZSM- catalysts prepared using $Ni/CNT_{(10-20)}$ and $Ni/CNT_{(20-40)}$ as hard templates did not show any peaks characteristic of the nickel oxide phases. No XRD peaks assigned to the Mg-containing phases were detected in either Mg/ZSM-5 prepared via aqueous impregnation or in $MgCNT_{(10-20)}$/ZSM-5 and $MgCNT_{(20-40)}$/ZSM-5 catalysts prepared using hydrothermal synthesis with the Mg/CNT hard template. The absence of XRD peaks attributed to the metal oxide phases can be explained by smaller metal oxide particle size in the Mg- and Ni-containing samples, which are below the XRD detection limits.

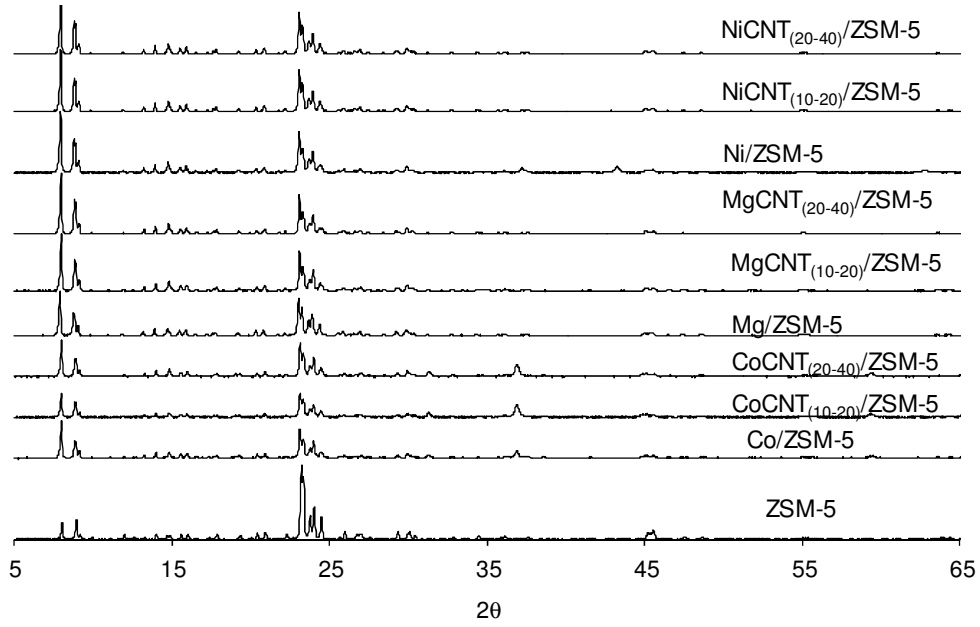

Figure 5-2 XRD patterns of the metal ZSM-5 catalysts.

Figure 5-3 shows the TEM images of the Co, Ni and Mg containing ZSM-5 catalysts prepared using metal-CNT templates. They are very different from those usually observed for the conventional ZSM-5 zeolite. The zeolite crystallites obtained in the presence of metal CNT templates exhibit a rather irregular fibrous shape leading to the development of zeolite mesoporosity. TEM images suggest zeolite crystallization over CNT. This shape arises from CNT partially encapsulated inside the zeolite crystals during the zeolite synthesis. The synthesized zeolite seems to replicas of Me/CNT. They reproduce almost exactly the shape of the secondary templates. Importantly, the presence of metal containing CNT seems indispensable for obtaining these fibrous zeolite crystallites. The TEM images for all prepared metal-zeolite catalysts also display small metal oxide nanoparticles with the diameter between 1 and 5 nm.

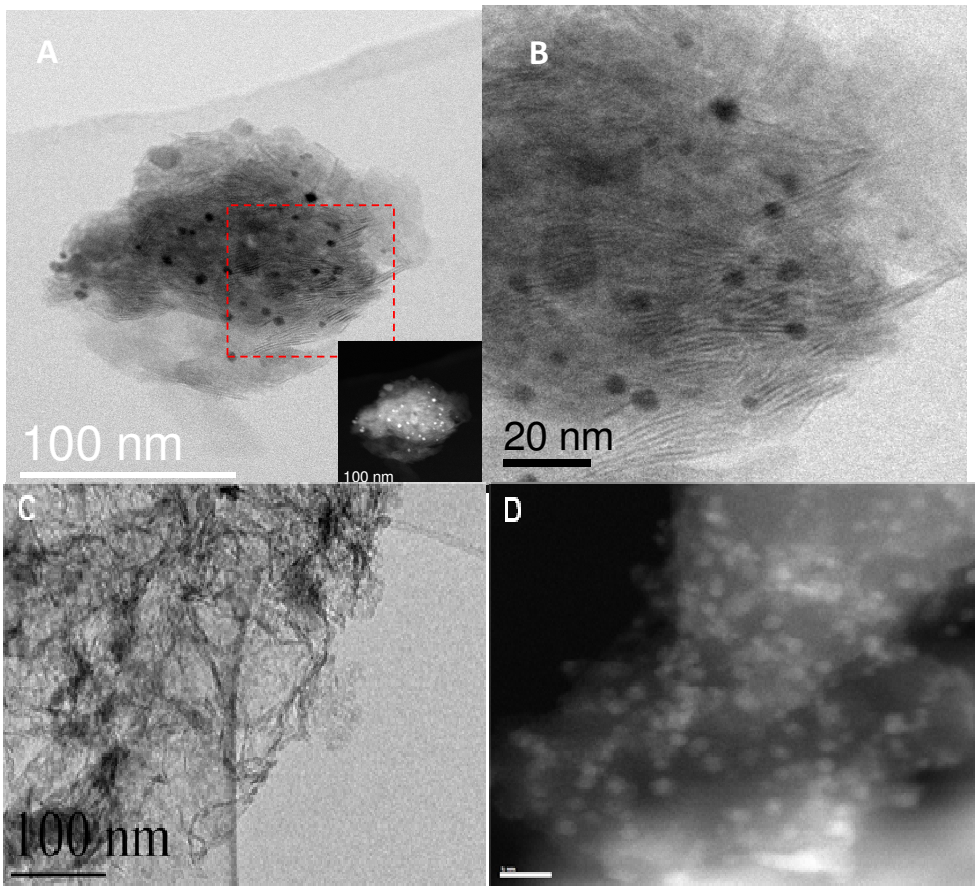

Figure 5-3 TEM images of $CoCNT_{(10-20)}$/ZSM-5 high magnification(A), $CoCNT_{(20-40)}$/ZSM-5 high magnification (B), $MgCNT_{(10-20)}$/ZSM-5 (C) and $NiCNT_{(20-40)}$/ZSM-5 (D).

The presence of zeolite phase in these fibrous structures was further confirmed by selected area electron diffraction (SAED). Figure 5-4 displays well defined diffraction patterns and clearly indicates zeolite crystalline phase in the areas containing a larger quantify of fibrous zeolite replicas of the Me/CNT templates.

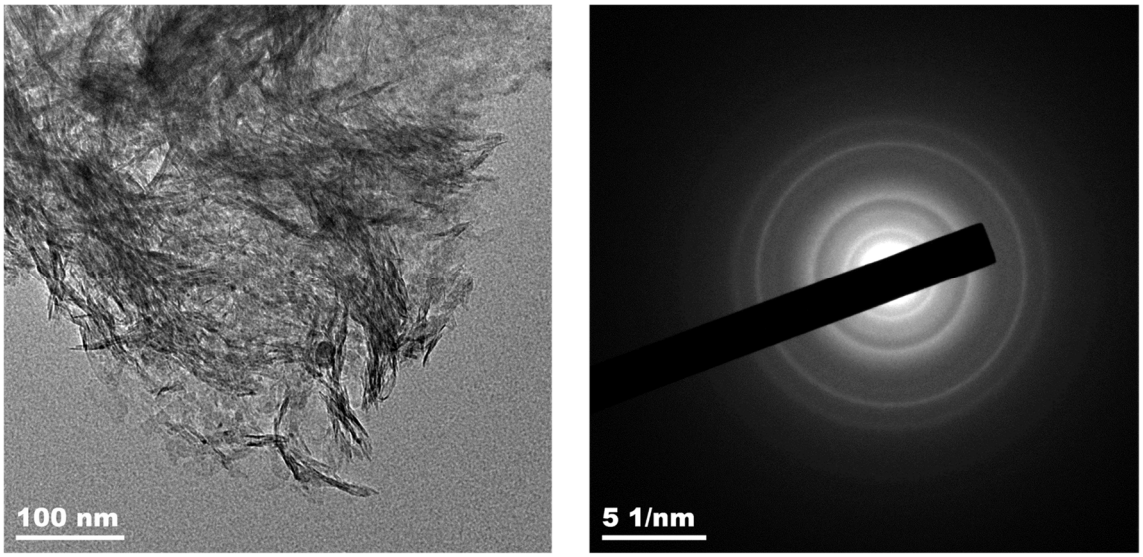

Figure 5-4 TEM image and SAED patterns of NiCNT(20-40)/ZSM-5 zeolite.

STEM-HAADF electron tomography of the $CoCNT_{(20-40)}$/ZSM-5 sample has confirmed localization of metal oxide nanoparticles within the zeolite (Figure 5-5). Co nanoparticles have been observed as bright spots with diameter in the range 2-5 nm. STEM-HAADF images show that nanoparticles are located inside the pores of $CoCNT_{(20-40)}$/ZSM-zeolite. Thus, electron microscopy, electron diffraction and tomography in combination with other characterization techniques revealed the important role of small metal oxide clusters in CNT for the formation of mesopores in zeolite crystals. Note that no noticeable enhancement of the zeolite mesoporosity was observed by using metal-free CNT as secondary templates (Table 5-1).

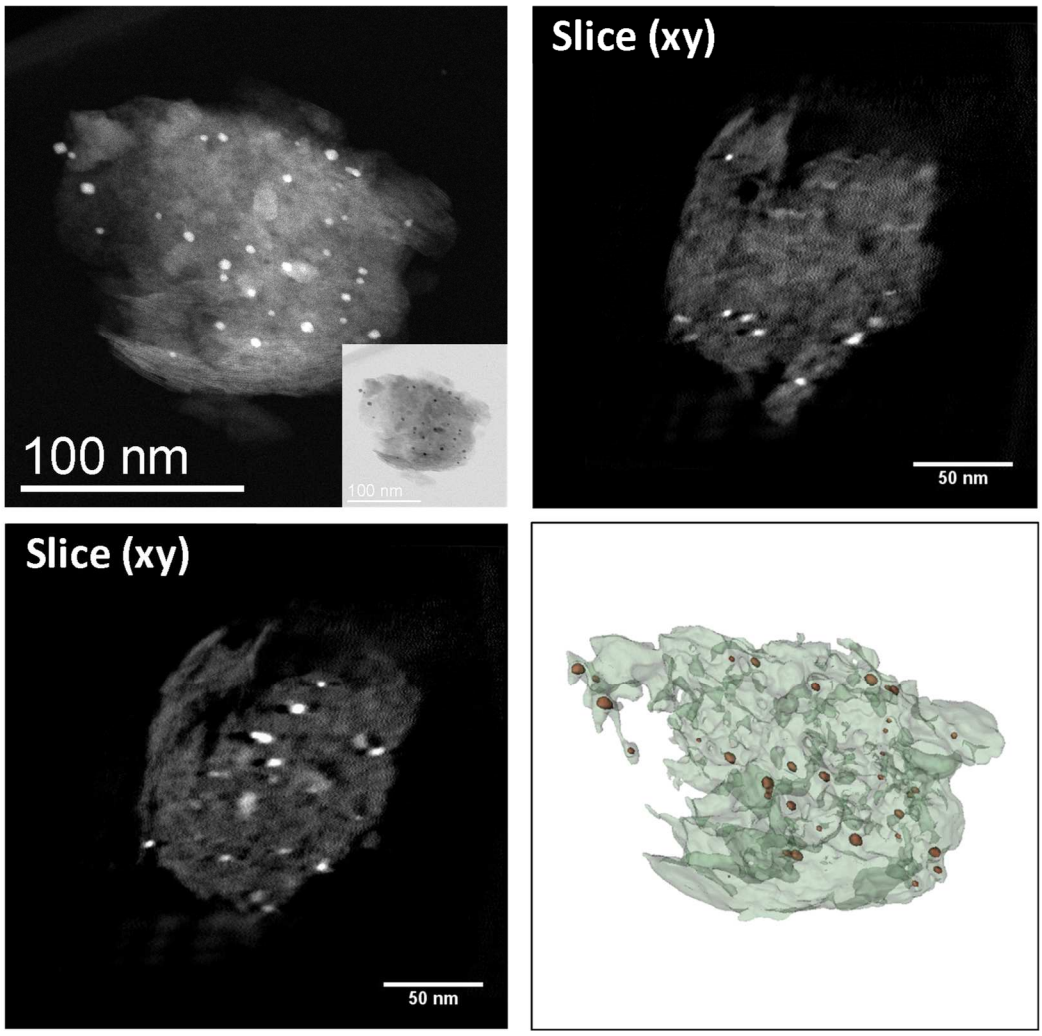

Figure 5-5 STEM-HAADF electron tomography analysis of $CoCNT_{(20-40)}$/ZSM-5 catalyst clearly showing the presence of cobalt nanoparticles inside the zeolite structure.

The ZSM-5 zeolite nucleation seems to occur on the metal oxide sites located on CNT and results in the hierarchical zeolites with enhanced mesoporosity. The resulting zeolite replicates the fibrous shape of CNT. The mesopores are created when CNT are removed from the zeolite by calcination. A scheme illustrating the formation of hierarchical zeolite during the synthesis utilizing Me/CNT as secondary hard templates is shown in Figure 5-6. It is important to emphasize that the stability of metal oxide nanoparticles supported on CNT in the basic medium used for zeolite synthesis is essential for obtaining hierarchical zeolites with enhanced mesoporosity. Our experiments with templates on the basis of iron and copper oxides supported on CNT did

not result in the zeolites with enhanced mesoporosity. This seems to be a consequence of the dissolution of iron and copper oxides in basic medium during zeolite synthesis.

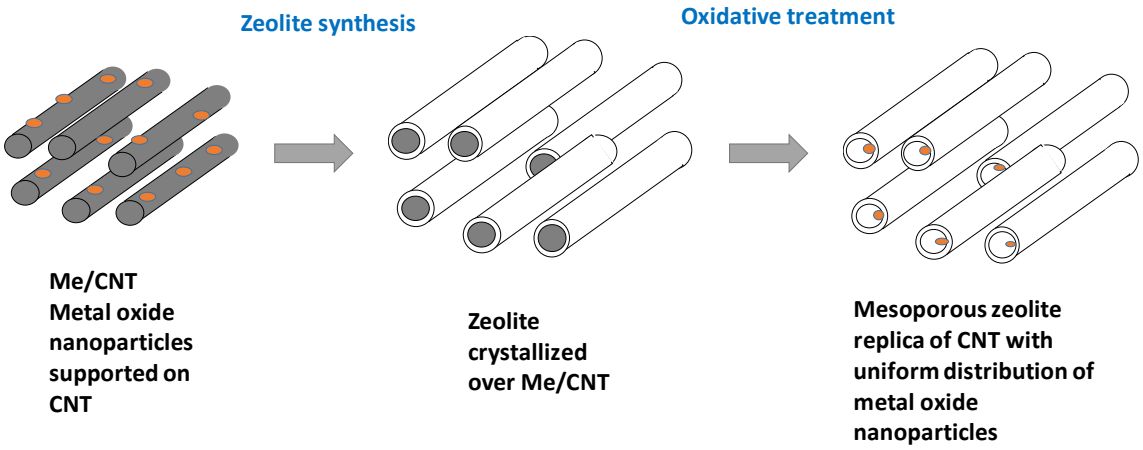

Figure 5-6 Synthesis of hierarchical zeolites using metal oxide supported on CNT as secondary hard templates.

Cobalt and nickel temperature programed reduction (TPR) profiles are presented in Figure 5-7. The reduction patterns of the cobalt zeolite catalysts are consistent with the presence of several types of cobalt species and two-step Co_3O_4 reduction to metallic cobalt. Previous reports [27-29] suggest that Co_3O_4 is first reduced to CoO at a lower temperature, whereas CoO is reduced to metallic Co at higher temperatures (Figure 5-7a). The Co/ZSM-5 sample with cobalt added by impregnation exhibits a TPR peak at 280°C with shoulders at 150-220 °C. The shoulders at 150-220 °C in the TPR profile of Co/ZSM-5 can be therefore attributed to the reduction of the Co_3O_4 nanoparticles to CoO, while the major TPR peak at 280°C corresponds to the reduction of CoO to metallic cobalt. Previously we showed that the ZSM-5 catalysts prepared by impregnation contained a large fraction of cobalt oxide nanoparticles on the zeolite outer surface. Because of a larger solvating shell, diffusion of multi-charged ions such as cobalt or nickel, inside the ZSM-5 micropores can be rather slow [30]. In all catalysts prepared by impregnation, a considerable amount of bivalent metal ions are present on the zeolite

external surface. The $CoCNT_{(10-20)}$/ZSM-5 and $CoCNT_{(20-40)}$/ZSM-5 samples exhibited two groups of TPR peaks at 150-420 °C and at 600 – 800 °C. Similar to the Co/ZSM-5 zeolite, the low temperature peaks are attributed to the reduction of small Co_3O_4 nanoparticles to metallic cobalt via intermediate formation of CoO. The shift of these peaks to higher temperature can be explained by smaller Co_3O_4 particle sizes [31] and their localization inside the zeolite meso- and micropores. In agreement with previous studies [32, 33], the peaks at higher temperature are assigned to cobalt silicates or aluminates. These mixed compounds form because of the interaction and chemical reactions between the small metal oxide nanoparticles located on CNT and zeolite synthetized under the hydrothermal conditions. The TPR data are consistent with the suggestions that cobalt species supported on CNT act as nucleation sites in the synthesis of the hierarchical ZSM-5 zeolite.

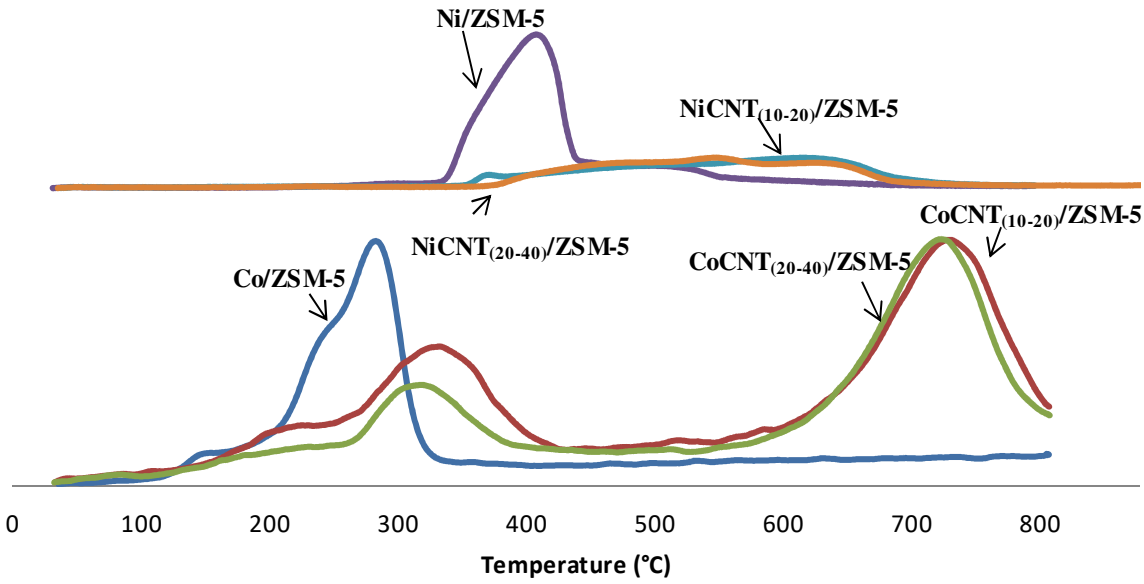

Figure 5-7 Temperature programmed reduction (TPR) profiles of the Co (a) and Ni (b) catalysts.

The reduction profiles of the nickel catalysts prepared by impregnation with nickel nitrate and synthetized using Ni/CNT as secondary templates are shown in Figure 5-7b. They exhibit broad hydrogen consumption peaks in the temperature range from 350 to 750°C. A single hydrogen consumption peak at about 400°C [34, 35] is usually observed in the TPR profile of bulk NiO. It corresponds to the reduction of NiO to metallic nickel. Thus, the low temperature peaks located between 400 and 500°C in the TPR profiles of nickel-zeolite catalysts may correspond to the reduction of small NiO particles. Note that the Ni/ZSM-5 zeolite prepared by impregnation usually contains a significant concentration of NiO on the zeolite outer surface. These NiO nanoparticles are detected in Ni/ZSM-5 by XRD (Figure 5-2). Similar to cobalt zeolite nanocomposites, the shift of the TPR peaks to a higher temperature can be due to the smaller NiO particle size and some diffusional limitations during their reduction arising from the localization of these small NiO nanoparticles in the porous material [36]. The area of the low temperature TPR peaks between 400° and 500 °C significantly decreases for the catalysts prepared using Ni/CNT as secondary templates. This corresponds to the decrease in the concentration of the NiO particles on the zeolite outer surface. The TPR profiles of the $NiCNT_{(10\text{-}20)}$/ZSM-5 and $NiCNT_{(20\text{-}40)}$CNT/ZSM-5 catalysts exhibit low intensity peaks at 500-700 °C. High temperature TPR peaks can be attributed to the reduction of highly dispersed nickel species [37] or to the presence of nickel silicate (phyllosilicate) species [38, 39]. In agreement with other characterization methods, the TPR results clearly show that introduction of nickel and cobalt species with CNT during the zeolite hydrothermal synthesis results to higher metal dispersion. In cobalt catalysts, metal nanoparticle localization within zeolite meso- and micropores also leads to the formation of mixed compounds between metal oxide, silica or alumina.

The acidity of the metal-zeolite catalysts has been characterized by FTIR using adsorption of pyridine (Py) as a probe for Brönsted (BAS) and Lewis acid sites (LAS). The FTIR spectra recorded after Py adsorption on the reduced catalysts are displayed in Figure 5-8. The pure ZSM-5 zeolite exhibits characteristic bands at ~1545 and 1455-45 cm^{-1} assigned to the pyridinum ion (PyH^+) formed on BAS and to Py adsorbed on LAS (which may also include metal ions such as Co^{2+}, Ni^{2+} or Mg^{2+}), respectively. Py adsorbed on both the LAS and BAS also displays a band at 1490 cm^{-1}. The concentrations of BAS and LAS calculated using the molar absorption coefficients for the bands at ~1545 and 1455-45 cm^{-1} are shown in Table 5-1. Impregnation of the ZSM-5 zeolite with Co^{2+}, $Ni^{2+,}$ and Mg^{2+} cations leads to a significant decrease in the concentration of BAS. The effect is more pronounced for the Mg^{2+} impregnated ZSM-5. A much lower concentration of BAS in the impregnated catalysts can be explained by the ion exchange of the zeolite bridging OH group protons with the Mg^{2+}, Ni^{2+} and Co^{2+} ions. Small metal oxide clusters can also block some zeolite microporesthus making some of BAS inaccessible for Py adsorption. Interestingly, at the same metal content in the zeolites, the decrease in the concentration of BAS is less significant, when the cations are introduced with the Me/CNT hard templates. This suggests that a significant fraction of the metal species added with Me/CNT are probably not localized in the cationic zeolite sites but present as small oxide clusters in the zeolite micro- and mesopores. This explain a less significant decrease in the number of BAS in the zeolites synthetized using the Me/CNT hard templates with the same metal contents.

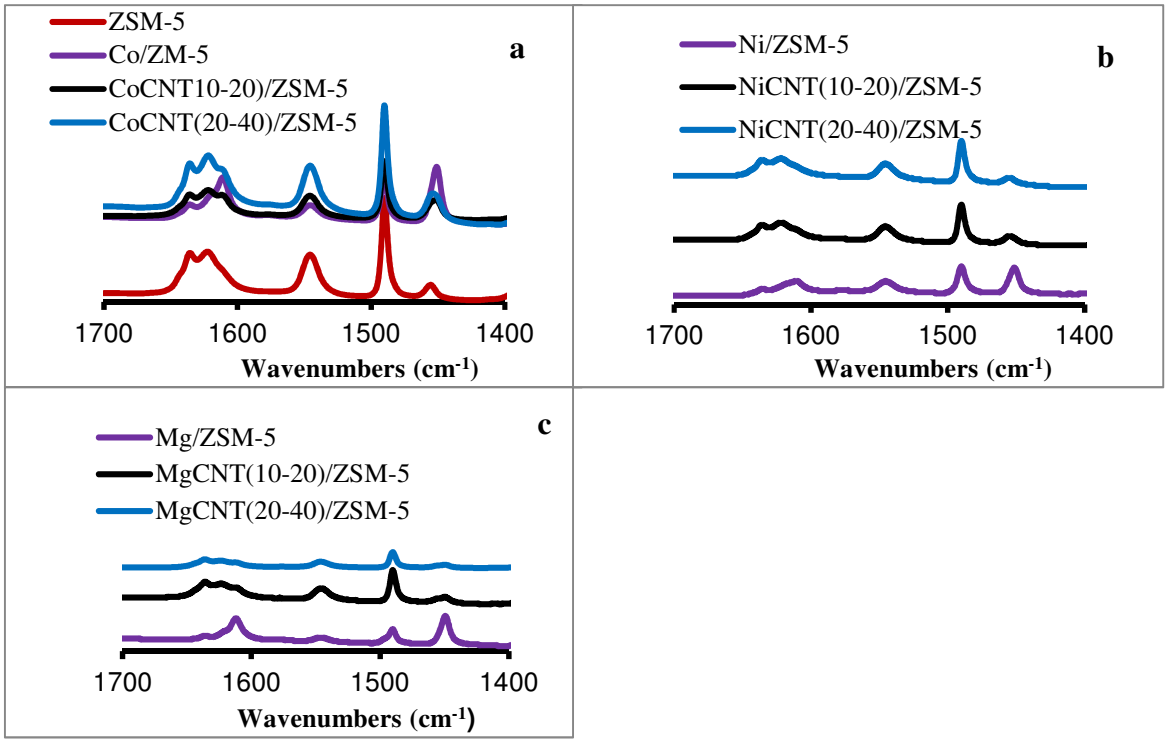

Figure 5-8 FTIR spectra observed after adsorption of Py on cobalt (a), nickel (b) and magnesium (c) zeolite catalysts

The number of LAS is considerably higher in all metal containing ZSM-5 as compared to their metal-free ZSM-5 counterpart (Table 5-1). The addition of the metals results in the generation of news types of Lewis acid sites such as coordinatively unsaturated Co^{2+}, Ni^{2+} or Mg^{2+} cations. Some of these cations can occupy zeolite cationic sites. Interestingly, a much lower concentration of Lewis acid sites is generated in the metal zeolite catalysts prepared using zeolite crystallization in the presence of metal CNT secondary templates as compared to the sample prepared by zeolite impregnation with nitrates. This can be due to a lower concentration of Co^{2+}, Ni^{2+} and Mg^{2+} in the cationic sites of the hierarchical zeolites. This also indicates the formation of metal oxide clusters and is consistent with a smaller decrease in the number of BAS in the zeolites prepared using the Me/CNT hard templates.

Catalytic Performance in Fischer-Tropsch Synthesis, Hydrogenation and Acylation Reactions

The results of catalytic tests of cobalt zeolite catalysts in Fischer-Tropsch synthesis are presented in Table 5-2. Hydrocarbons and water were major reaction products of carbon monoxide hydrogenation. Extremely small amounts of CO_2 were observed. By varying GHSV between 20 and 70 L/hg_{Co}, the CO conversion of 30 – 40% was obtained for all catalysts. The reaction rate normalized by the amount of cobalt in the catalysts slightly increases for $CoCNT_{(10-20)}$/ZSM-5 and decreases in $CoCNT_{(20-40)}$/ZSM-5 compared to the Co/ZSM-5 sample prepared by conventional impregnation. Note however, that TPR (Figure 5-7a) is indicative of very different cobalt reducibility in different samples. The addition of the Co/CNT hard templates during the zeolite synthesis results in the formation of barely reducible cobalt silicate or cobalt aluminate species, which exhibit TPR peaks at 800-900°C. The peaks at 800-900°C are absent in the TPR profiles of Co/ZSM-5. This suggests a low concentration of cobalt silicates or aluminates in the Co/ZSM-5 catalyst prepared by impregnation. Interestingly, the activity per reducible cobalt increased 5 – 10 times over CoCNT/ZSM-5 prepared using CoCNT as secondary templates in comparison with Co/ZSM-5 prepared by impregnation. The methane selectivity varied between 13 – 37%. Previous report [40] suggests that the higher methane selectivity over zeolite based catalysts can be due to more significant diffusion limitations for carbon monoxide molecules compared to hydrogen. Slower diffusion of CO relative to hydrogen results in the CO deficiency the zeolite pores. The resulting higher H_2/CO ratio in the narrow zeolite pores leads to a higher contribution of methanation reaction and higher methane selectivity. Importantly, lower methane selectivity was observed over $CoCNT_{(10-20)}$/ZSM-5 and $CoCNT_{(20-40)}$/ZSM-5 with larger mesoporous volume. These catalysts may have less significant diffusion limitations

compared to mostly microporous Co/ZSM-5, where cobalt was added by impregnation. The catalysts prepared using the $CoCN5_{(10-20)}$ and $CoCNT_{(20-40)}$ hard templates also exhibit a higher selectivity to the C_5^+ products (around 74%) as compared to the conventional Co/ZSM-5 catalysts which exhibited C_{5+} selectivity of 48% (Table 5-2).

Table 5-2. Activity and selectivity of the catalysts for the Fischer-Tropsch synthesis reaction (P=2 MPa, GHSV=20-70 L/hgCo, T=250 °C, H_2/CO=2)

Catalyst	Activity ($mmol_{CO}/h.g_{Co}$)[a]	Conversion (%)	Selectivity (mol. C%)					
			CH_4	C_2-C_4	C_2-C_4 (olefin)	C_2-C_4 (paraffin)	C_2-C_4 (P/O)	C_5^+
Co/ZSM-5	244	39	32.8	19.0	2.7	16.3	6.0	48.1
$CoCNT_{(10-20)}$/ZSM-5	352 (1961)[b]	42	15.9	13.8	2.8	11.0	3.9	73.1
$CoCNT_{(20-40)}$/ZSM-5	131 (1893)[b]	28	12.6	13.2	3.0	10.2	3.4	74.2

[a]Time at 24 h. [b] In brackets: activity in reducible cobalt basis.

Nickel catalysts were tested in the toluene and 1,3,5-triisopropylbenzene hydrogenation (Table 5-2). These reactions were used to evaluate the activity and accessibility of nickel metal sites in the hierarchical zeolites. The mesoporosity developed in the nickel-zeolite catalysts synthetized in the presence of Ni/CNT secondary templates results in a significantly higher hydrogenation rate in both toluene and 1,3,5-triisopropylbenzene reactions. The reaction rate increases in the order: Ni/SZM-5< $NiCNT_{(10-20)}$/ZSM-5<$NiCNT_{(20-40)}$/ZSM-5. This is therefore indicative of a better nickel dispersion and enhanced accessibility of nickel metallic sites in the zeolites prepared using the Ni/CNT hard templates. Noteworthy, the zeolite prepared using $NiCNT_{(20-40)}$ with larger CNT diameter exhibited higher reaction rate in both toluene and 1,3,5-triisopropylbenzene hydrogenation reactions.

Table 5-3. Hydrogenation reaction (H_2=20 mL/min, Liquid flow=0.8 mL/h T=250 °C, P=20 bar).

Catalyst	Toluene Conversion (%)	1,3,5-Triisopropylbenzene Conversion (%)
Ni/ZSM-5	60	23.7
$NiCNT_{(10-20)}$/ZSM-5	83.3	50.8
$NiCNT_{(20-40)}$/ZSM-5	97.7	97

*Time at 6 h.

Zeolites usually contain significant concentration of acid sites. Acylation of anisole with hexanoic acid was selected as a model reaction to characterize the catalytic performance of the acid sites on the outer surface and in the mesopores of the hierarchical zeolites (Figure 5-9).

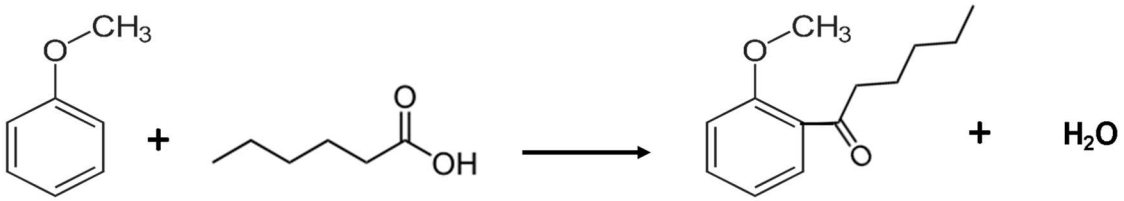

Figure 5-9 Acylation of anisole with hexanoic acid results in ortho-methoxy-hexyl-phenone.

On all catalysts evaluated in the present work, the reaction results in the formation of ortho-methoxy-hexyl-phenone with the selectivity higher than 90%, while the selectivity to the para-isomer was less than 10%. Only traces of the meta-isomer were detected. Note that the size of the ortho-isomer is much higher than the dimeter of micropores in the ZSM-5 zeolite. Higher selectivity to the larger size ortho- methoxy-hexyl-phenone is consistent with the critical role of the zeolite acid sites on the zeolite outer surface and mesopores in this reaction. The hexanoic acid conversion and reaction rate are displayed in Table 5-4. For all catalysts, the conversion increases, when Me/CNTs were added as hard templates during the zeolite synthesis. The conversion increases 2-4

times over $CoCNT_{(10-20)}$/ZSM-5 and $CoCNT_{(20-40)}$/ZSM-5; 1.3-1.6 times over $NiCNT_{(10-20)}$/ZSM-5 and $NiCNT_{(20-40)}$/ZSM-5 and 4.5 – 5.0 times over $MgCNT_{(10-20)}$/ZSM-5 and $MgCNT_{(20-40)}$/ZSM-5 in comparison with their counterparts prepared via impregnation. The effect is more pronounced when CNT had a relatively large (20-40 nm) diameter. The highest conversion was achieved over $NiCNT_{(20-40)}$/ZSM-5.

Table 5-4. Acylation reaction (2 g of anisol, 0.3 g hexanoic acid, 20 mg of the catalyst, T=180 °C).

Catalyst	Conversion (%)	Reaction rate (μmol/g min)
Co/ZSM-5	0.43	4.63
$CoCNT_{(10-20)}$/ZSM-5	1.00	10.78
$CoCNT_{(20-40)}$/ZSM-5	1.79	19.29
Ni/ZSM-5	1.53	16.49
$NiCNT_{(10-20)}$/ZSM-5	1.92	20.69
$NiCNT_{(20-40)}$/ZSM-5	2.46	26.51
Mg/ZSM-5	0.26	2.80
$MgCNT_{(10-20)}$/ZSM-5	1.18	12.72
$MgCNT_{(20-40)}$/ZSM-5	1.31	14.12

*time at 2 h.

Figure 5-10 shows the relation between the conversion of hexanoic acid and the number of Brönsted acid sites in the catalysts. Both the concentration of Brönsted acid sites and the presence of mesopores created in the ZSM-5 zeolite in the presence of metal supported CNT affect the catalytic performance in the anisole acylation. Interestingly, at similar concentration of BAS, the higher acylation rates were observed for the catalysts with higher mesoporosity. In particular, the CNT diameter is important for preparing the metal zeolite catalysts with higher reaction rates. The zeolites with larger mesopores obtained using Me/CNT with the diameter of 20-40 nm were the most active in this reaction. This suggests a better accessibility of both Brönsted and metal sites in the hierarchical ZSM-5 prepared using the Me/CNT templates. Hence, the strategy for

synthesis of hierarchical zeolites using metal supported CNT as secondary hard templates seems promising. It produces hierarchical zeolites replicating the shape of CNT with enhanced mesoporosity and containing highly dispersed, accessible and uniformly distributed metal and acid sites, which will be certainly beneficial for several important catalytic reactions.

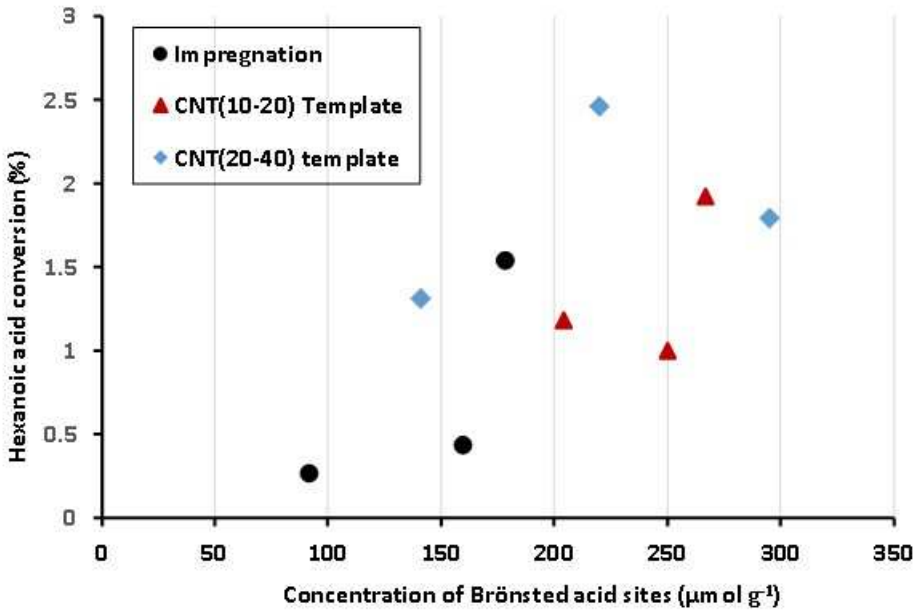

Figure 5-10 Hexanoic acid conversion in anisole acylation over the metal zeolite catalysts prepared by impregnation and using Me/CNT as secondary hard templates.

5.3 Conclusion

A new synthesis strategy for the preparation of hierarchical zeolites preparation has been developed. The zeolite crystallites were prepared under hydrothermal conditions in the presence of CNT supported metal nanoparticles used as secondary hard templates. The Me/CNT templates play three roles in the synthesis of hierarchical zeolite. These templates are at the same time (i) a zeolite synthesis replica, (ii) a mesoporogen and (a) a tool to introduce uniformly distributed metal species into zeolites.

The metal oxide species seem to be nucleation sites and crystallization modifier leading to the fibrous zeolite structures, which largely replicates the CNT. Using Me/CNT as templates leads a several-fold increase in the zeolite mesoporous volume. In the synthetized zeolites, the dispersed metal species are uniformly distributed within the crystallites and mostly present as small metal oxide nanoparticles. The concentration of Brönsted acid sites in the zeolites synthetized using Me/CNT as secondary templates is higher than in the zeolites with the same amount of metal species prepared via impregnation.

Because of a decrease in the diffusion limitations and uniform distribution of metal nanoparticles in the zeolite, the resulting materials have shown improved catalytic performance in three catalytic reactions: Fischer-Tropsch synthesis, hydrogenation of aromatics and anisole acylation.

References

[1] Corma, A. From Microporous to Mesoporous Molecular Sieve Materials and Their Use in Catalysis, *Chem. Rev.* **1997**, 97, 2373-2419.

[2] Egeblad, K.; Christensen, C.H.; Kustova, M.; Christensen, C. H. Templating Mesoporous Zeolites, *Chem. Mater.* **2008**, 20, 946–960.

[3] Ertl, G.; Knözinger, H.; Weitkamp, J. in Preparation of solid acids, Wiley-VCH, Germany 1999.

[4] Weisz, P.B. Polyfunctional heterogeneous catalysis, *Adv. Catal.* **1962**, 13, 137-190.

[5] Subramanian, V.; Zholobenko, V.L.; Cheng, K.; Lancelot, C.; Heyte, S.; Thuriot, J.; Paul, S.; Ordomsky, V.V.; Khodakov, A.Y. The Role of Steric Effects and Acidity in the Direct Synthesis of iso-Paraffins from Syngas on Cobalt Zeolite Catalysts, *ChemCatChem* **2016**, 8, 380-389.

[6] Ertl, G.; Knözinger, H.; Weitkamp, J. in Preparation of solid acids, Wiley-VCH, Germany, 1999.

[7] Zečević, J.; Vanbutsele, G.; de Jong, K.P.; Martens, J.A. Nanoscale intimacy in bifunctional catalysts for selective conversion of hydrocarbons, *Nature* **2015**, 528, 247.

[8] Samad, J. E.; Blanchard, J.; Sayag, C.; Louis, C.; Regalbuto, J.R. The controlled synthesis of metal-acid bifunctional catalysts: The effect of metal:acid ratio and metal-acid proximity in Pt silica-alumina catalysts for n-heptane isomerization, *J. Catal.* **2016,** 342, 203–212.

[9] Prins, R. Hydrogen Spillover. Facts and Fiction. *Chem. Rev*. **2012**, 112, 2714–2738.

[10] Im, J.; Shin, H.; Jang, H.; Kim, H.; Choi, M. *Nat. Commun*. **2014**, 5, Article number: 3370.

[11] Carvalho, A.; Marinova, M. ; Batalha, N. ; Marcilio, N.R. Khodakov, A.Y.; Ordomsky, V.V. Design of nanocomposites with cobalt encapsulated in the zeolite

micropores for selective synthesis of isoparaffins in Fischer–Tropsch reaction, *Catal. Sci. Technol.* **2017**, 7, 5019-5027.

[12] Peron, D. V. ; Zholobenko, V.L.; Rodrigues de la Rocha, M.; Oberson de Souza, M. ; Feris, L.A. ; Marcilio, N.R. ; Ordomsky, V.V. ; Khodakov, A.Y. Nickel–zeolite composite catalysts with metal nanoparticles selectively encapsulated in the zeolite micropores, *J Mater Sci,* **2019**, 54, 5399–5411.

[13] Tosheva, L.; Valtchev, V.P. Nanozeolites: Synthesis, Crystallization Mechanism, and Applications, *Chem. Mater.* **2005**, 17, 2494-2513.

[13] Jiang, J.; Yu, J.; Corma, A. Extra-Large-Pore Zeolites: Bridging the Gap between Micro and Mesoporous Structures, *Angew. Chem. Int. Ed.* **2010**, 49, 3120 – 3145.

[15] Tao, Y.; Kanoh, H.; Abrams, L.; Kaneko, K. Mesopore-Modified Zeolites: Preparation, Characterization, and Applications, *Chem. Rev.* **2006**, 106, 896-910.

[16] van Donk, S., Janssen, A.H.; Bitter, J.H.; de Jong, K.P. Generation, Characterization, and Impact of Mesopores in Zeolite Catalysts, *Catal. Rev. Sci. Eng*. **2003**, 45, 297-319.

[17] Chen, H.; Wang, Q.; Zhang, X.; Wang, L. Hydroconversion of jatropha oil to alternative fuel over hierarchical ZSM-5. *Ind. Eng. Chem. Res*. **2014**, 53, 19916-19924.

[18] Schmidt, I.; Boisen, A.; Gustavsson, E.; Ståhl, K.; Pehrson, S.; Dahl, S.; Carlsson, A.; Jacobsen, C. J. H. Carbon Nanotube Templated Growth of Mesoporous Zeolite Single Crystals, *Chem. Mater.* **2001**, 13, 4416-4418.

[19] Boisen, A.; Schmidt, I.; Carlsson, A.; Dahl, S.; Brorson, M.; Jacobsen, C.J.H. TEM stereo-imaging of mesoporous zeolite single crystals, *Chem. Commun*. **2003**, 958–959.

[20] Meng, X.; Nawaz, F.; Xiao, F.-C. Templating route for synthesizing mesoporous zeolites with improved catalytic properties, *Nano Today* **2009**, 4, 292-301.

[21] Zhou, M.; Wang, F.; Xiao, W.; Gao, L.; Xiao, G. The comparison of mesoporous HZSM-5 zeolite catalysts prepared by different mesoporous templates and their catalytic

performance in the methanol to aromatics reaction, *Reac Kinet Mech Cat* **2016**, 119, 699–713.

[22] Zhai, Y.; Zhu, Z.; Dong, S. Carbon-Based Nanostructures for Advanced Catalysis, *ChemCatChem* **2015**, 7, 2806-2815.

[23] Liu, W.-W.; Chai, S.-P.; Mohamed, A.R.; Hashim, U. Synthesis and characterization of graphene and carbon nanotubes: A review on the past and recent developments. *J. Ind. Eng. Chem.* **2014**, 20, 1171-1185.

[24] Flores, C.; Batalha, N.; Ordomsky, V.; Zholobenko, V.L.; Baaziz, W.; Marcilio, N.R.; Khodakov, A.Y. Direct Production of Iso-Paraffins from Syngas over Hierarchical Cobalt-ZSM-5 Nanocomposites Synthetized by using Carbon Nanotubes as Sacrificial Templates, *ChemCatChem*, **2018**, 10, 2291-2299.

[25] van't Blik, H.F.J.; Prins, R. Characterization of supported cobalt and cobalt-rhodium catalysts: III. Temperature-Programmed Reduction (TPR), Oxidation (TPO), and EXAFS of Co-Rh/SiO2. *J. Catal.* **1986**, 97, 210-218.

[26] Hong, J.; Marceau, E.; Khodakov, A.Y.; Griboval-Constant, A.; La Fontaine, C.; Villain, F.; Briois, V.; Chernavskii, P.A. Impact of sorbitol addition on the structure and performance of silica-supported cobalt catalysts for Fischer–Tropsch synthesis, *Catal. Today* **2011**, 175, 528-533.

[27] Khodakov, A.Y.; Griboval-Constant, A.; Bechara, R.; Villain, F. Pore-size control of cobalt dispersion and reducibility in mesoporous silicas, *J. Phys. Chem. B* **2001**, 105, 9805-9811.

[28] Stakheev, A.Y.; Khodakov, A.Y.; Kustov, L.M.; Kazansky, V.B.; Minachev, K.M. Localization of polyvalent cations in pentasil catalysts modified by metal oxides. *Zeolites* **1992**, 12, 866-869.

[29] Khodakov, A.Y.; Lynch, J.; Bazin, D.; Rebours, B.; Zanier, N.; Moisson, B.; Chaumette, P. Reducibility of cobalt species in silica-supported Fischer–Tropsch catalysts, *J. Catal.* **1997**, 168, 16-25.

[30] Puskas, I.; Meyers, B. L.; Hall, J. B. Activity decline and diffusional changes in a magnesium-promoted cobalt-silica catalyst, *Catal. Today* **1994**, 21, 243–251.

[31] S. Jong, J.; Cheng, S. Reduction behavior and catalytic properties of cobalt containing ZSM-5 zeolites, *Appl. Catal. A* **1995**, 126, 51–66.

[32] Tomiyama, S.; Takahashi, R.; Sato, S.; Sodesawa, T.; Yoshida, S. Preparation of Ni/SiO2 catalyst with high thermal stability for CO2-reforming of CH4. *Appl. Catal. A* **2003**, 241, 349-361.

[33] Soghrati, E., Kay, T.; Ong, C.; Kok Poh, C.; Kawi, S.; Borgna, A. Zeolite–supported nickel phyllosilicate catalyst for CO hydrogenolysis of cyclic ethers and polyols, *Appl. Catal. B* **2018**, 235, 130-142.

[34] Maia, A.J.; Louis, B.; Lam, Y.L.; Pereira, M.M. Ni-ZSM-5 catalysts: Detailed characterization of metal sites for proper catalyst design, *J. Catal.* **2010**, 269, 103–109.

[35] Romero, M.D.; de Lucas, A.; Calles, J.A.; Rodriguez, A. Bifunctional catalyst Ni/HZSM-5: effects of the nickel incorporation method, *Appl. Catal. A* **1996**, 146, 425-441.

[36] Chen, B.-H.; Chao, Z.-S.; He, H.; Huang, C.; Liu, Y.-J.; Yi, W.-J.; Wei, X.-L.; An, J.-F. Towards a full understanding of the nature of Ni(ii) species and hydroxyl groups over highly siliceous HZSM-5 zeolite supported nickel catalysts prepared by a deposition-precipitation method. *Dalton Trans.* **2016**, 45, 2720-2739.

[37] B.- Chen, B.-H.; Liu, W.; Li, A.; Liu, Y.-J.; Chao Z.-S. A simple and convenient approach for preparing core–shell-like silica@ nickel species nanoparticles: highly

efficient and stable catalyst for the dehydrogenation of 1, 2-cyclohexanediol to catechol, *Dalton Trans*. **2015**, 44, 1023-1038.

[38] Iglesia, E.; Reyes, S.C.; Madon, R. J. and Soled, S.L. *Adv. Catal.* **1993**, 39, 221-302.

Chapter 6: General Conclusion and Perspectives

This thesis was performed at "Unité de catalyse et de chimie du solide" (UCCS), University of Lille, France, and in the Department of Chemical Engineering, Federal University of Rio Grando Do Sul, Brazil in 2016-2019. The main objective of this Ph. D. thesis was to design bifunctional catalysts on the basis of metal nanoparticles and mesoporous zeolites with the target to enhance their catalytic performance in different reactions such as Fischer Tropsch synthesis, toluene and 1, 3, 5 triisoproplybenzene hydrogenation and acylation of anisole. The work followed three parallel and complementary paths. The first one (Chapter 3) is centered on the study of influence of impregnation and ion exchange sequence, in particular on the metal localization, acidity of cobalt supported on the large pore BEA zeolite. The second (Chapter 4) is focused on the production of iso-paraffins from syngas, more specifically by creating hierarchical ZSM-5 zeolite using cobalt CNT as sacrificial template. The third (Chapter 5) is aimed on mesoporosity creation of ZSM-5 using different metals like nickel and magnesium supported on CNT.

6.1 General Conclusion

In chapter III, four different catalysts prepared using different ion exchange sequence were synthesized: Co/HBEA, CoH/HBEA, Co/NaBEA, CoH/NaBEA. Cobalt impregnation on the H-from of BEA results in cobalt localization on the outer surface and in the zeolite micropores. The deposition of cobalt on the BEA zeolite external surface and in the micropores leads to cracking and higher methane selectivities in FT synthesis. The catalyst CoH/NaBEA with the Co species localized on the external surface and high concentration of Brönsted acid sites in the zeolite micropores, showed lower methane

selectivity, higher selectivity to long chain hydrocarbons and significant yield of isomerized hydrocarbons. This strategy seems to have several advantages for the design of bifunctional catalysts over large pore zeolites.

In chapter IV, the use of the bifunctional Co/ZSM-5 catalysts enhanced the iso-paraffin selectivity in FT synthesis. This improvement can be attributed by creation of the mesopores in the ZSM-5 zeolite using metal-CNT as templates. The mesoporosity increased 3-4 times by introducing Co/CNT during the zeolite synthesis. Besides that, when cobalt was impregnated in the CNT and then placed in the synthesis gel, the resulting zeolite had higher amount of Brönsted acid sites. This methodology leads to more uniform metal distribution on the support and greater proximity between active metal sites and acid sites from the zeolite. The catalysts prepared using Co/CNT as secondary templates presented an enhanced selectivity to isomerized branched hydrocarbons and lower methane selectivity.

In chapter V, the methodology used to create hierarchical zeolite with metal CNT was extended to other metals like Ni and Mg. The deposed metal particles have uniform distribution in the crystallites of hierarchical zeolites. Important roles of the metal carbon nanotubes in the zeolite synthesis are uncovered. First, Me/CNT serve as a replica to create zeolites with specific fibrous morphology. Second, they fulfill the role of a mesoporogen and markedly increase the zeolite secondary porosity. Finally, they act as a vehicle to uniformly introduce the metal functions inside the mesoporous zeolites. The presence of metals in carbon nanotubes is essential for the enhancement of mesoporosity.

This thesis clearly shows that the catalytic performance of metal zeolite composite catalysts is a function of zeolite mesoporososity, zeolite pore sizes, zeolite acidity and localization of metal nanoparticles on the zeolite outer surface or in the zeolite

micropores. Because of the decrease in the diffusion limitations and uniform distribution of metal nanoparticles in the zeolite, the resulting materials have shown improved catalytic performance in three catalytic reactions: Fischer-Tropsch synthesis, hydrogenation of aromatics and anisole acylation.

6.2 Perspectives

Thus, efficient control of localization of metal and acid sites within metal zeolite composite catalysts is a very useful tool to tune the catalytic performance for many catalytic reactions. The results of this thesis allow us to propose new strategies for the design of bifunctional catalysts. In particular, two new methodologies can be further developed such as

- Introducing one metal inside the CNT and another metal outside the CNT when using Me/CNT as templates for zeolite synthesis. This strategy should reduce formation of barely reducible metal silicates with the metal species which are located inside CNT;

- Microemulsion methodology which might control the size of metal nanoparticles deposed inside the micro and mesopores of zeolite and

- Catalyst deactivation is a major challenge for the design of bifunctional catalysts. Though the catalysts developed in these work were stable in lab scale experiments, further long duration tests are required to evaluate their stability under industrial conditions.